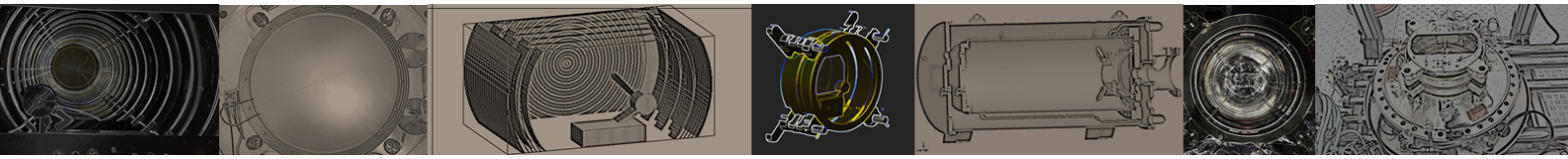

Mass and Life-time Measurement of the 1.7 ms ^{215}Po Isotope

A Crucial Test of the Novel Concept of the Cryogenic Ion Catcher for the Super-FRS at GSI-FAIR

Inauguraldissertation zur Erlangung des Doktorgrades der Naturwissenschaftlichen Fakultät der Justus-Liebug Universität Gießen

vorgelegt von: Ann-Kathrin Rink

vorgelegt am: 24.05.2017

Erstgutachter: Prof. Dr. Dr. h.c. Hans Geissel

Zweitgutachter: Prof. Dr. Christoph Scheidenberger

IONAS

FAIR

JUSTUS-LIEBIG-UNIVERSITÄT GIESSEN

GSI

Contents

1 Motivation

The origin and properties of short-lived nuclei in the universe are fundamental topics of nuclear and astrophysics today. Various scenarios describe the nucleosynthesis from big bang until today. In the early universe, milliseconds after the big bang, proton and neutron formation took place and later also light nuclei like deuterium, helium and lithium have been produced in primordial processes. [Rolfs and Rodney, 1988]

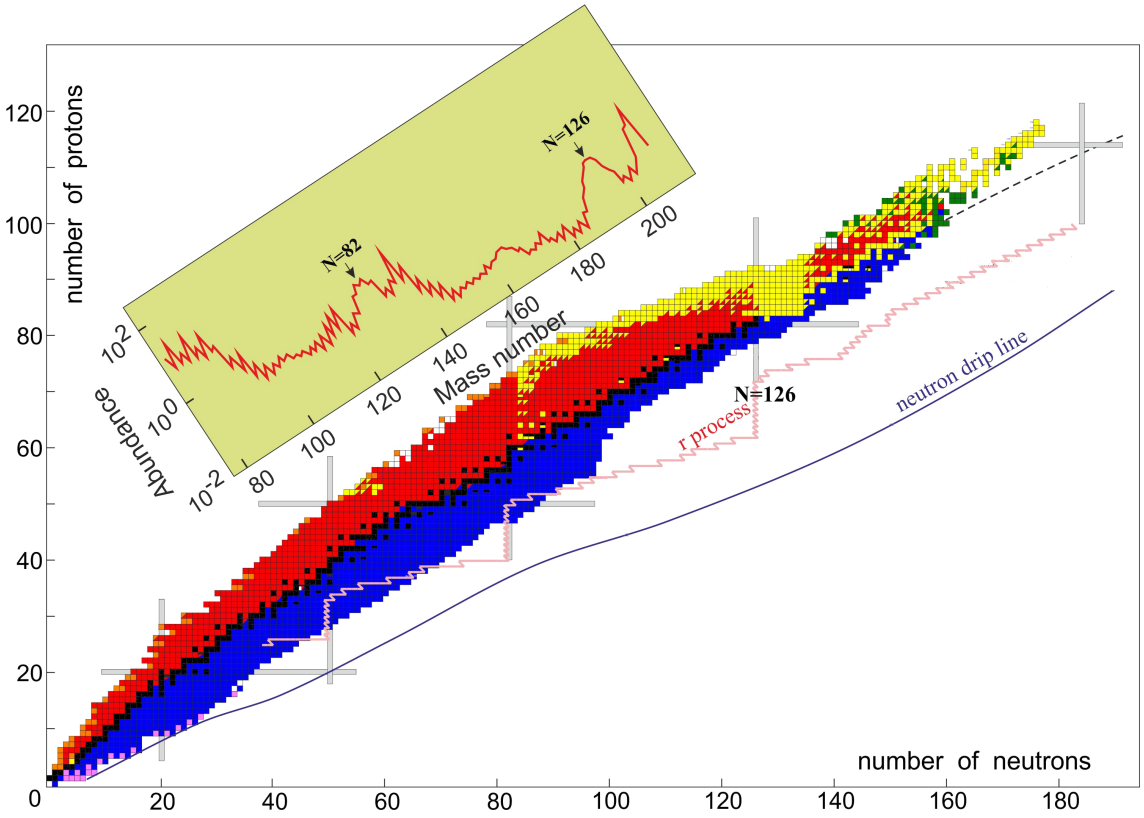

Figure 1.1: Chart of nuclides including a projection of the nuclear abundance of the elements in the universe. The chart has been modified from [FLNR, 2017].

Heavier nuclei are produced in fusion reactions in the stars. Depending on the mass of the star the burning process can reach elements up to iron in exothermic reactions. The maximum of the binding energy is reached at iron and thus the fusion reactions in stars terminate at this element. Since the stellar burning (fusion) cannot explain the nuclear abundances of heavy ions, see Figure 1.1, additional nucleosynthesis

scenarios need to be considered. In addition to fusion reactions, nuclear capture processes take place, such as proton and neutron capture. Elements beyond iron are produced via capture processes and subsequent β-decay. Neutron capture processes take place at different neutron densities. In stellar scenarios with neutron densities of $10^8\,\mathrm{cm}^{-3}$ mainly the slow neutron capture process (s-process) dominates. In this case, capture reactions are in the same time regime as the half-life of the subsequent β-decays. The s-process ends at ^{209}Bi isotope due to the short α-decay lifetime between the elements of Bi and Th.

For the production of the heavier elements like uranium and thorium another neutron capture scenario is responsible: the r-process. The r-process is a rapid neutron capture process that requires many orders of magnitude higher neutron densities than the s-process. Neutron densities between $10^{20}\,\mathrm{cm}^{-3} < \mathrm{n_n} < 10^{28}\,\mathrm{cm}^{-3}$ at temperatures of $10^9\,\mathrm{K}$ [Kratz et al., 1993] [Kreim et al., 2013] are necessary for fast capture reactions. Whereas the s-process runs along the valley of stability, the r-process path is located near the neutron drip-line in the region of nuclei with half-lives in μs to ms range.

The fact that neither the s- nor r-process can describe the production of the most neutron-deficient isotopes, proton capture reactions (p-process) must contribute to the nucleosynthesis.

Describing these nuclear reactions correctly, theoretical models need input from measurements of nuclear properties. Experimental nuclear masses, separation energies as well as half-lives are essential components in theoretical models. Meanwhile, the nuclear properties are well known for species at and near the valley of stability, whereas for short-lived exotic nuclei the information is rare. Exotic nuclei are characterised by short half-lives, low production cross sections, and quite different properties compared to stable nuclei. Therefore, new developments and faster measurements are the keys in this research. Leading heavy ion facilities are at Cern (Switzerland), GANIL(France), GSI (Germany), JINR (Russia), MSU-NSCL (USA) and Riken (Japan).

In future, the facility for Anti-proton and Ion Research (FAIR) at GSI will substantially contribute to nuclear and astrophysics along the driplines and nucleosynthesis paths in the universe. FAIR will concentrate mainly on the investigation of heavy r-process nuclei.

2 Heavy ion penetration in matter and electromagnetic fields

2.1 Slowing down of ions in matter

When an energetic ion beam penetrates through matter, the ions lose energy in elastic and inelastic collisions and are deflected [Rutherford, 1911, Bohr, 1913] from their incident direction. The ions experience atomic and nuclear interactions, whereby the atomic collisions are dominating in thin layers at all energy domains. The collisions are of statistical nature and thus cause energy and angular straggling, which represent the second moments of the distributions. In atomic collisions the identity of the projectile and target nuclei are conserved, i.e., only the electron systems are excited or even removed from the colliding atoms.

At moderate relative velocities of the ions, the probability of nuclear reactions is very low during their travel in matter. At relativistic energies the atomic range reaches the order of the free path length for nuclear interaction and cannot be neglected anymore [Geissel et al., 2002]. In the latter case the full particle identification has to be performed in experimental atomic collision measurements.

2.1.1 Heavy Ion energy loss, stopping powers, energy straggling and ranges

The mean energy loss $\langle \Delta \mathrm{E} \rangle$ of an projectile penetrating a layer of matter Δx at an energy E is given by:

$$\frac{\langle \Delta E \rangle}{\Delta x} = N \underbrace{\sum_i \langle \sigma_i \rangle T_i}_{\substack{stopping\ cross\ section \mathbf{S(E)}}} . \tag{2.1}$$

The kinetic energy is lost in discrete quantities T_i [Bohr, 1913] in a number of i collisions within the density of target atoms N with the collision probability σ_i. The stopping power is defined by:

$$\frac{dE}{dx} = -NS(E) \tag{2.2}$$

The stopping power has an elastic and an inelastic contribution which are added. The elastic collisions of the colliding atoms determine the angular distribution but have a minor contribution to the total energy loss at kinetic projectile energies exceeding 1 MeV/u for all ions. The inelastic stopping power function reaches a maximum at a few MeV/u due to charge-changing collisions and the mean ionisation. The maximum is often called as Bragg peak. At kinetic energies beyond the Bragg peak at several hundreds of MeV/u the Lindhard and Sørensen theory describes the stopping power very well [Scheidenberger et al., 1994] [Lindhard and Scœrensen, 1996]. For fully ionised projectiles the stopping power can be described by:

$$S = \frac{4\pi Z_1^2 e^4}{mv^2} \cdot Z_2 L, \tag{2.3}$$

with the projectile charge number $Z_1 e$ and velocity v, and the target charge number Z_2. The so-called stopping number L takes into account the different contributions which cause strong deviations from the first Born approximation [Lindhard and Scœrensen, 1996].

A common way to include the different contribution is:

$$S = \frac{4\pi (Z_1 e)^2 e^2 N}{mv^2} \left[L_{\text{Bethe}} + \Delta L_{shell} + \Delta L_{\text{LS}} - \frac{\delta}{2} \right] \tag{2.4}$$

where L_{Bethe} is the Bethe stopping number based on first Born approximation and relativistic treatment [Bethe, 1932]. ΔL_{shell} takes care of the fast target electrons with minor contributions to the slowing down at small velocities. ΔL_{LS} is based on the solution of the Dirac-equation and includes the Bloch correction [Lindhard and Scœrensen, 1996] and at ultra relativistic velocities also the finite size of nuclear charge distribution. δ describes the so-called density effect due to polarisation in solids at very high projectile velocities.

The energy-transfer quantities in the different collisions are very small, thus the continuous slowing down approximation is valid over a large energy domain. The range R of the particles in matter is given by the differential equation:

$$R = \int_0^{E_0} dE' \frac{1}{N\, S(E')} \tag{2.5}$$

In experiments with the FRS thick layers of matter are used to perform the spatial isotopic separation. The degraders, placed at the focal planes, often exceeds a thickness of half the atomic range of the reference ions. In this case the total energy loss ΔE has to be calculated by solving the integral equation of the range differences:

$$\Delta E = R(E_1) - R(E_2), \tag{2.6}$$

where E_1 and E_2 are the incident and exit energies, respectively.

The width of the energy distribution is called energy straggling and represents often the second moment of the distribution. Analogous to the stopping power formula, we can write:

$$\Omega_{\mathrm{E}}^2 = N\Delta x \underbrace{\sum_i T_i^2 \sigma_i}_{\substack{straggling\\ parameter\\ W=\sum_i T_i^2\sigma_i}} . \tag{2.7}$$

Note that the energy straggling is determined by the square of the individual energy transfers T_i.

The energy straggling in thick layers of matter can be well described by [Geissel et al., 2002]:

$$\Omega_{\mathrm{E}}^2 = \left(\frac{dE(E_2)}{dx}\right)^2 \int_{E_1}^{E_2} \frac{\frac{d\Omega^2(E')}{d\Delta x}}{\left[\frac{dE(E')}{dx}\right]^3} dE', \tag{2.8}$$

where E_1 and E_2 are the projectile energies in front of and behind the straggling target, respectively.

The measured differential energy straggling $\frac{d\Omega^2(E')}{d\Delta x}$ deviates from the simple Bohr or Bethe formulas by more than a factor of two at relativistic energies [Scheidenberger and Geissel, 1998, Geissel et al., 2002]. However, the Lindhard-Sørensen theory [Lindhard and Scœrensen, 1996] is in very good agreement with precise energy-straggling data for fully ionised projectiles. The projectiles are fully ionised when they emerge from layers of matter, if their relative velocity is larger than the corresponding velocities of the K-shell electrons. At lower velocities an additional energy straggling component, the charge-changing energy straggling becomes significant and can also increase the width of the energy distribution by a factor of more than 2 [Weick et al., 2000].

The knowledge of the range distributions of heavy ions stopped in the gas-filled ion catcher is also very important for the experiments in this thesis.

Since for heavy projectiles at relativistic energies the total and the projected range distributions do not differ significantly, the range straggling can be calculated by a simple formula, which is also based on the continuous slowing down approximation and can be derived from transport equations:

$$\Omega_{\mathrm{range}}^2 = \int_{E_{\mathrm{min}}}^{E_1} \frac{\frac{d\Omega^2(E')}{d\Delta x}}{\left[\frac{dE(E')}{dx}\right]^3} dE', \tag{2.9}$$

where E_1, $\mathrm{E}_{\mathrm{min}}$ are the incident projectile energy and a tiny energy ($\mathrm{E}_{\mathrm{min}} > 0$) near complete stopping.

2.2 Ion mobility and diffusion

The motion of charged particles in electro-magnetic fields is described by the Lorentz force $\vec{F}_L$ [Lorentz, 1937] and the equation of motion

$$m\ddot{\vec{r}} + \gamma\dot{\vec{r}} = \vec{F}_L \tag{2.10}$$

$$\text{with} \qquad \gamma = \frac{q}{\mu_e m} \tag{2.11}$$

$$\text{and} \qquad \mu_e = \frac{T}{T_0}\frac{p_0}{p}\mu_0 \tag{2.12}$$

is the electrical mobility. In case of the stopping cell an external magnetic field is not applied:

$$m\ddot{\vec{r}} + \gamma\dot{\vec{r}} = q\vec{E} \tag{2.13}$$

2.2.1 Space-charge effects

Space-charge effects appear if the charge density is high enough that the ion motion is influenced by coulomb interactions with neighbouring ions. Produced by incoming ion beams, electron-ion pairs are separated by the electrical field. The transport of ions through gas is slow, compared to electrons which are transported fast to the electrodes.

Regarding at these interactions [Huyse et al., 2002, Batygin, 2011] the equation of motion is

$$m\frac{dv_i}{dt} = -q\nabla_i\Phi_p\left(r_i, t\right) + qE_{ext}\left(r_i, t\right) \tag{2.14}$$

with the induced field $\nabla\Phi$ and Poisson equation

$$\nabla\Phi_p\left(r, t\right) = -\frac{\rho\left(r, t\right)}{\epsilon_0} \tag{2.15}$$

and the charge density $\rho\left(r, t\right)$.

Diffusion

Particles in a gas volume without external forces show Brownian motion [Uhlenbeck and Anrnstein, 1930]. The probability of a particle colliding with others inside the stopping medium is always larger than > 0. In solid materials diffusion happens as well but with slightly different processes, due to additional contributions of the bound atoms.

We assume the only disturbance from outside is the electrical force F which is in the average zero. Hence, the forces on particles are in random directions. The equation

of motion under this condition is:

$$m\ddot{\vec{r}} + \gamma\dot{\vec{r}} = F(t) \qquad \text{with} \qquad \langle F(t)\rangle = 0. \tag{2.16}$$

2.3 Ion motion in electromagnetic fields

The trajectory of ions flying through electro-magnetic fields is bent. It results from the Lorentz force [Lorentz, 1937]

$$\vec{F_L} = q\vec{E} + q\left(\vec{v} \times \vec{B}\right) \tag{2.17}$$

with electric field $\vec{E}$, the magnetic field $\vec{B}$ and the ions velocity $\vec{v}$. For **magnetic** fields ($\vec{E} = 0$) the vector product describes the ions trajectory forced to form a circle, where the curvature radius is given by

$$r_M = \frac{m}{q} \cdot \frac{\vec{v_\perp}}{\vec{B}}. \tag{2.18}$$

For **electric** fields ($\vec{B} = 0$) the deformation of the rectilinear motion can be assumed to be circular for small angles. It follows $F_L = F_Z$ like in the magnetic field only case. Thus the extracted radius is given by

$$r_E = \frac{m}{q} \cdot \frac{\vec{v^2}}{\vec{E}}. \tag{2.19}$$

2.3.1 Ion motion in radio-frequency quadrupoles

The radio-frequency quadrupoles (RFQ) are electrical driven rods, tubes or simply electrodes with an oscillating quadrupole potential applied. They can be either used as a massfilter, trap or as an ion guide. To guide the ions, they need to be confined between the electrodes, which is described by the Mathieu equations. They are equations of motion that give stable motion inside oscillating fields like in RFQs. The second order equations of motion result in the visualised potentials as they can be seen in figure 2.1 top. The resulting force on charged particles inside an RFQ is describe by the Lorentz force (without $\vec{B}$)

$$\vec{F} = -e\vec{E} = \quad -e\nabla\phi_{x,y} \tag{2.20}$$

$$= \quad \left(-e\tfrac{\phi_0}{r_0^2}x, e\tfrac{\phi_0}{r_0^2}y, 0\right). \tag{2.21}$$

where ϕ is the quadrupole potential $\phi_{x,y,z} = A(\lambda x^2 + \sigma y^2 + \gamma z^2) + C$. To fulfil the Laplace equation $\nabla^2\phi_{x,y,z} = 0$ for an RFQ mass filter / ion guide $\lambda = -\sigma$ and $\gamma = 0$ solve the equation.

With a time varying potential applied to the RFQ's the potential $\phi_0(t)$ looks like

$$\phi_0 = U - Vcos(\Omega t) \qquad \text{with} \qquad \Omega = 2\pi f \tag{2.22}$$

And it follows for the equation of motion

$$\frac{d^2u}{d\xi^2} + (a_u - 2b_u cos2\xi)\, u = 0 \tag{2.23}$$

using the substitution $\xi = \Omega t/2$, u is representing x or y. a and b are called Mathieu parameters, figure 2.1 dependency of a stable ion motion on these parameters is given.

$$\begin{pmatrix} m\frac{d^2x}{dt^2} = \frac{-e\phi_0}{r_0^2}x \\ m\frac{d^2y}{dt^2} = \frac{e\phi_0}{r_0^2}y \\ 0 \end{pmatrix} \Rightarrow \begin{pmatrix} \frac{d^2x}{d\xi^2} = \frac{-4e}{mr_0^2\Omega^2}(U - Vcos2\xi)x \\ \frac{d^2y}{d\xi^2} = \frac{4e}{mr_0^2\Omega^2}(U - Vcos2\xi)y \\ 0 \end{pmatrix} \tag{2.24}$$

For more details see [Haettner, 2011] and [Dawson, 1976]. To use RFQs as an ion guide an additional drag field needs to be applied to transport the ions in z-direction along the RFQ rods.

2.3.2 Ion motion on a radio-frequency carpet

To extract ions from a gas filled stopping cell two major methods are in use.

1. Extraction via gas flow. This method is mainly used for short gas catchers e.g. the IGISOL technique [Dendooven, 1997]; The biggest issue is the time the ions need for extraction since this time is depending on the gas flow of the system. It rises proportional to the cell length.
2. Extraction via DC and radio-frequency (RF) field; The ions transport is now dominated by the electrical fields instead of the gas flow and thus extraction times can be fast even for long gas cells.

The ion motion of the latter method can be manipulated by applying a pseudo-potential

$$V_{\mathrm{p}}(r) = \frac{q}{4m\Omega^2} E_{\mathrm{RF}}^2(r) \tag{2.25}$$

on a carpet with RF electrode structure. There the potential depends on the mass-to-charge ratio of the manipulating ion, the radio-frequncy $\Omega = 2\pi f_{RF}$ and an approach of the electrical field with a quadrupole field

$$E_{\mathrm{RF}} = E_0 cos(\Omega t) \tag{2.26}$$

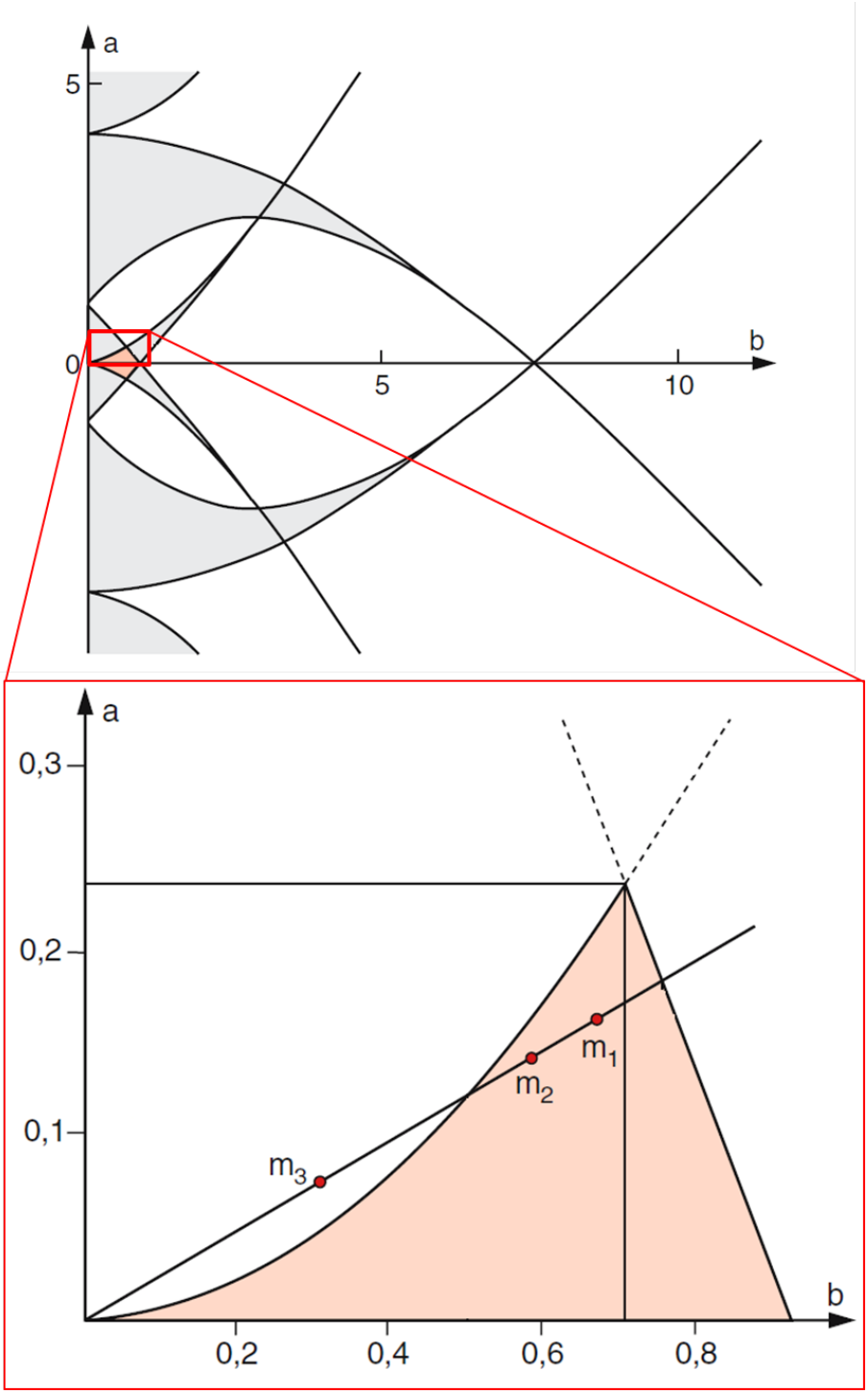

Figure 2.1: TOP PANEL: Stability diagram of radio-frequency quadrupoles showing the stable areas for ion motion with the Mathieu parameters a and b [Demtröder, 2010].
BOTTOM PANEL: Zoom into the first region of stability. For $a = 0$ the RFQ works as an ion guide, all masses (m_1, m_2, m_3) are transported. For $a > 0$ the RFQ works mass selective and it depends on the slope of the line.

$$\text{with} \qquad E_0 = \frac{r}{r_0} \cdot E_{\max} \qquad \text{for} \qquad 0 < r < r_0 \tag{2.27}$$

$$\text{and} \qquad E_0 = 0 \qquad \text{for} \qquad r > r_0 \wedge r < 0. \tag{2.28}$$

For operation under gas pressure the relaxation time τ has to implemented as a correction [Tolmachev et al., 1997]. The relaxation time is described as the time the ions need to loose their energy gained by the electrical field by collisions with the gas atoms.

$$\tau = \kappa \frac{m}{q} \tag{2.29}$$

Knowing the relaxation time τ and the RF frequency Ω the damping coefficient γ is given by

$$\gamma = \frac{\Omega^2 \tau^2}{1 + \Omega^2 \tau^2} \tag{2.30}$$

to determine the effective electrical field E_{eff} in front of the RF structure (the RF carpet). Therefore the pseudopotential E_p of the effective field E_{eff} is

$$E_{\text{eff}} = \gamma \cdot E_{\text{p}}. \tag{2.31}$$

With

$$E_{\text{p}} = -\nabla V_{\text{p}} \tag{2.32}$$

the effective field at the RF carpet can be described as

$$E_{\text{eff}} = \frac{q V_{\text{RF}}^2}{2 m \Omega^2 r_0^3} \cdot \left(\frac{r}{r_0} \right) \cdot \frac{\Omega^2 \tau^2}{1 + \Omega^2 \tau^2} \tag{2.33}$$

Two cases are distinguished. The vacuum case where $\tau \gg 1$ and the high pressure case for $\tau \ll 1$. It follows

$$E_{\text{Eff}} = \tau^2 \frac{q V_{\text{RF}}^2}{2 m r_0^3} \frac{r}{r_0} \tag{2.34}$$

With equation (2.29) and $\kappa = \kappa_0 \frac{p_0}{p} \frac{T}{T_0}$ the effective electrical field at the RF carpet is defined as

$$E_{\text{Eff}} = \frac{m V_{\text{RF}}}{2 q r_0^3} \cdot \left(\kappa_0 \frac{p_0}{p} \frac{T}{T_0} \right)^2 \frac{r}{r_0} \tag{2.35}$$

3 Tools to investigate exotic nuclei

Exotic nuclei are of basic interest to understand the strong interaction and the nucleosynthesis in the universe. These short-lived nuclei are still produced in stars, whereas they cannot be found in nature on Earth. Exotic nuclei on Earth can nowadays be produced via different reactions in accelerator based laboratories. Different production, separation and investigation methods have been development in the previous decades.

3.1 Exotic nuclear beam facilities

The investigation of exotic nuclei is a great challenge because their production cross sections are very small down to the pb range and their lifetimes are in the ms range and shorter. Therefore, special efforts are required to access efficiently rare isotopes in the laboratory. Two main types of exotic-nuclear beam facilities have been successfully applied: the Isotope Separation On-Line (ISOL) and the in-flight methods.

3.1.1 Isotope separation on-line method

ISOL facilities (Isotope Separation On-Line) are producing exotic nuclei by bombarding a thick target with intense high-energetic proton beams via target fragmentation. These targets vary from solid to liquid to gaseous. Depending on the nuclei of interest the targets have a thickness of several mg/cm^2 for light and heavy fusion evaporation reactions up to thick targets with hundreds of g/cm^2 thickness for neutron induced spallation, fragmentation and fission [Blumenfeld et al., 2013]. The produced exotic nuclei are stopped immediately inside the thick target and extracted via diffusion through the target material to the ion source. In case of thin targets a gas catcher collects the produced elements and isobars (see IGISOL – ion guide isotope separation on-line). For investigation at experiments the nuclei need to be ionised, therefor different procedures are in use. The most common ones are e.g. surface ionisation, resonant laser ionisation and electron cyclotron resonance (ECR). One fundamental problem of the ISOL method is the element selectivity of the extraction process after production. The diffusion process only works for non-refractory isotopes [Ravn et al., 1975] [Bjørnstad et al., 1986], whereas refractory elements are used as target material since they are very resistive to heat and wear.

(a)

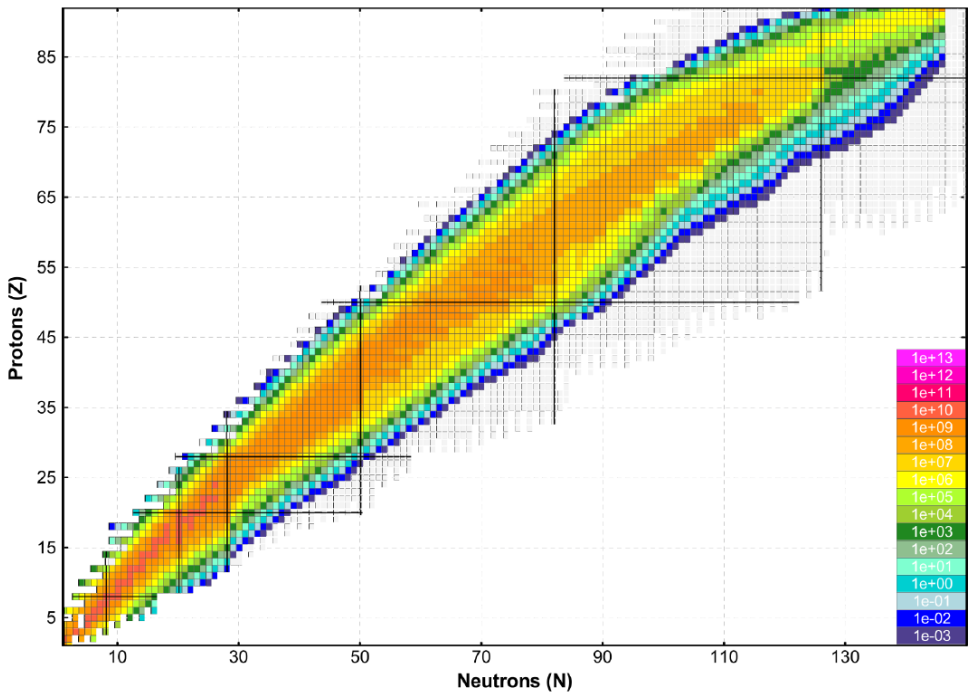

(b)

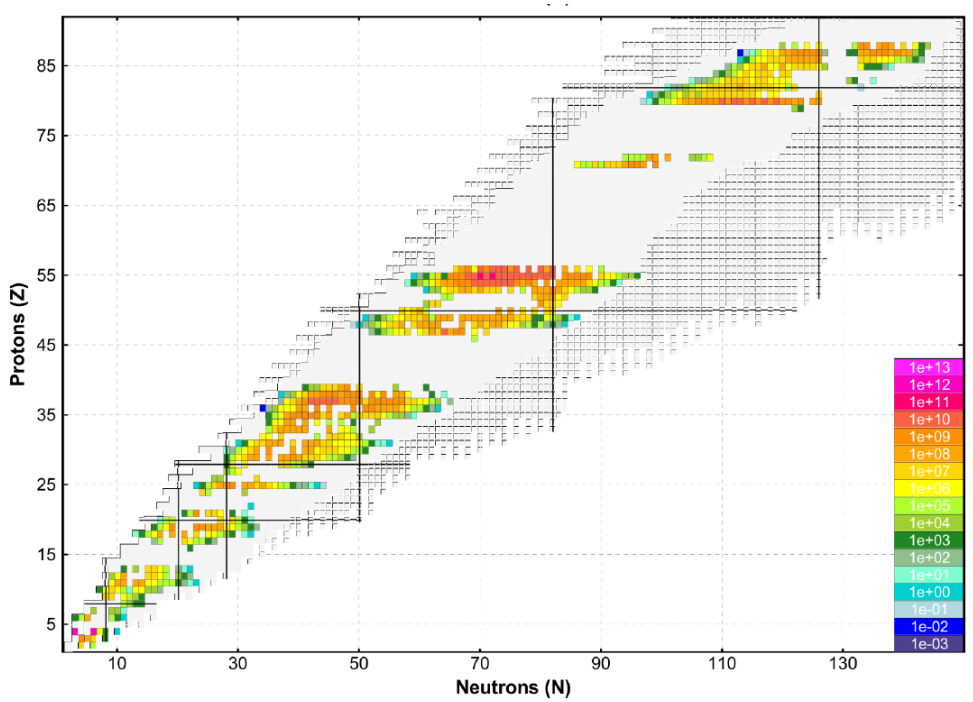

Figure 3.1: Comparison of the access to exotic nuclides for the In-Flight (panel a) and ISOL (panel b) production methods. In the chart of nuclides calculated production cross sections for fragmentation are indicated. The gaps in panel b) demonstrate that ISOL has limitations, specially for the refractive elements and nuclei with very short half-lives [ISOLDE, ,Reiter, 2015].

Connected to the element selectivity is the study of ions with short life-times, they need to have a half-life of several milliseconds or to be produced with high rates to compensate decay losses during the extraction process.
[Geissel et al., 1995]

IGISOL – ion guide isotope separation on-line

The IGISOL facilities [Dendooven, 1997] [Äysto, 2001] and references therein are based on the ISOL method, but use thinner targets and catches the produced nuclei with an ion guide. Because of their recoil energy the produced ions enter the gas filled cell and are extracted (still ionised) with the gas flow into an isotope separator. The IGISOL technique is compared to the standard ISOL technique faster with production and separation times in the sub-ms range, but is not suited for heavy ions.

3.1.2 In-flight method

In-flight production of exotic nuclei takes place at heavy ion accelerator facilities for instance at GSI (Germany) and RIKEN (Japan). The ion beams are accelerated up to $1,4\,\mathrm{GeV/u}$ and used as projectiles for thin target bombardment. In the moment the beam hits the target two main reactions take place the same time:

- Projectile fission – The Projectile is exited by the target atom, for de-excitation it fissions into two daughter nuclides.
- Projectile fragmentation – The projectile is fragmented by abrasion of several nucleons

These reactions can produce elements all across the nuclear chart from projectile downwards. A limitation of the in-flight method is the production cross section of the nuclei (for comparison of ISOL and In-Flight see figure 3.1). At the Fragment Separator (FRS) at GSI the ions impinge on a thin target with relativistic energies up to $1.5\,\mathrm{GeV/u}$ for light ion beams and $1\,\mathrm{GeV/u}$ for heavy ones. To have each ion species naked a Neodymium stripper foil follows the production target to ionise the out coming ion beam to the maximum.

3.1.3 Hybrid-method

The hybrid-method combines the advantages of both production methods that are described above. It uses the in-flight technique for ion production and separation and slows the ions down to energies almost at rest comparable to those at ISOL facilities. It enables high precision experiments at low energies for in-flight facilities.

3.2 High accuracy measurements

Measurements of exotic nuclei far off stability require fast and efficient methods due to their short lives and mostly low rates. For nuclear theory calculations and mass models experimental data is a great benefit, it is the more precise the input the more precise the output of predictions and models. Therefore high precision experiments and techniques have been developed.

3.2.1 Ion trap techniques

Ion traps always base on the same principles. The ions (almost at rest) are trapped inside a field. These fields can be electric or magnetic fields or even a superposition of both. They are trapped due to radial forces or inside harmonic potentials of electric or magnetic fields depending on their mass-to-charge ratio. Trapped in the potential the ions can either be cooled with buffer gas collisions, bunched or further investigated.

Radio-frequency quadrupole cooler buncher (RFQCB) are RFQs that bunch a continuous ion beam. It is collecting ions inside the RF field applying a potential wall which is switched low to release the ions into the downstream beam line. Before ions enter the RFQCB they are slowed down to $\sim 100\,\mathrm{eV}$ There are two main modes of operation

1. Bunches with low energy spread ($\sim 1\,\mathrm{eV}$) but long extraction ($\sim \mu\mathrm{s}$)
2. Bunches with well defined size (extraction $\sim 10 - 100\,\mathrm{ns}$) but larger energy spread

Mode 1 is required for performing collinear Laser spectroscopy and penning trap measurements. Mode 2 is required for Multiple-Reflection Time-of-Flight Mass Spectrometry.

Penning traps are high precision measurement tools and based on H.G. Dehmelt [Dehmelt, 1967] and W. Paul [Paul and Steinwedel, 1953]. super positioned weak electrostatic potential and a strong homogeneous magnetic field ($\vec{E} \perp \vec{B}$) confine charged particles in all spatial directions. The particle's motion in such a trap is described via superposition of three independent ion motions. The axial motion

$$\nu_z = \frac{1}{2\pi}\sqrt{\frac{qV_0}{md^2}} \tag{3.1}$$

depends on the mass-to-charge ratio m/q and trap potential V_0 and dimension d^2. And two radial motions

$$\nu_\pm = \frac{1}{4\pi}\left(\nu_c \pm \sqrt{\nu_c^2 - 2\nu_z^2}\right) \tag{3.2}$$

with the cyclotron frequency

$$\nu_c = \frac{1}{2\pi} \cdot \frac{q}{m} \cdot B \tag{3.3}$$

For nuclear structure physics experimental accuracies down to $10^{-7} - 10^{-8}$ are required. To ensure these high accuracies for absolute mass measurements the calibration ion needs to be as well known as the demanded precision.

3.2.2 Time-of-flight techniques

Mass and lifetime determination can be done via the nuclide time-of-flight over a certain distance as well.

Storage rings

In storage rings two established methods of mass measurements are performed. At GSI these measurements are performed at the experimental storage ring (ESR) [Geissel et al., 1992]. The revolution frequency of the ions circulating in the ring is mass dependent. This frequency is determined either with the Schottky-mass-spectrometry (SMS) demonstrated in figure 3.2*left* or the Isochronous Mass Spectrometry (IMS) demonstrated in figure 3.2*right* do perform high accuracy mass measurements in two different ways. [Franzke, 1987] [Franzke et al., 2008] The mass resolving power is give by

$$\frac{\Delta f}{f} = -\frac{1}{\gamma}\frac{\Delta m/q}{m/q} + \frac{\Delta v}{v}\left(1 - \frac{\gamma^2}{\gamma_t^2}\right). \tag{3.4}$$

For SMS the ion beam is cooled via electron and stochastic cooling, that it reduces the velocity contribution of the mass dependent frequency described in equation (3.4), that $\Delta v/v \to 0$. It detects the revolution frequency via none-destructive Schottky noise pick-ups. Due to fixed times needed for cooling processes SMS is limited by the life times of the nuclei of a few seconds.

In IMS the ions are none cooled and the spread in velocity of ions of the same species is compensated by different path length in the ring. The ions perform isochronous turns and the velocity is chosen such that $\gamma^2/\gamma_t^2 \to 1$. The revolving ions are detected by a TOF detector that is placed at that very position the ions have exact the same revolution time, the so-called time focus. Without the ion cooling process the access to exotic nuclei is widened out to ions with life times of tens of μs and thus is much faster.

Multiple-reflection time-of-flight mass spectrometers and separators

Multiple-reflection time-of-flight mass spectrometers / separators (MR-TOF MS) are electrostatic only devices [Plaß et al., 2013b]. They perform measurements by measuring the time the ions need from a specific starting point to the detector

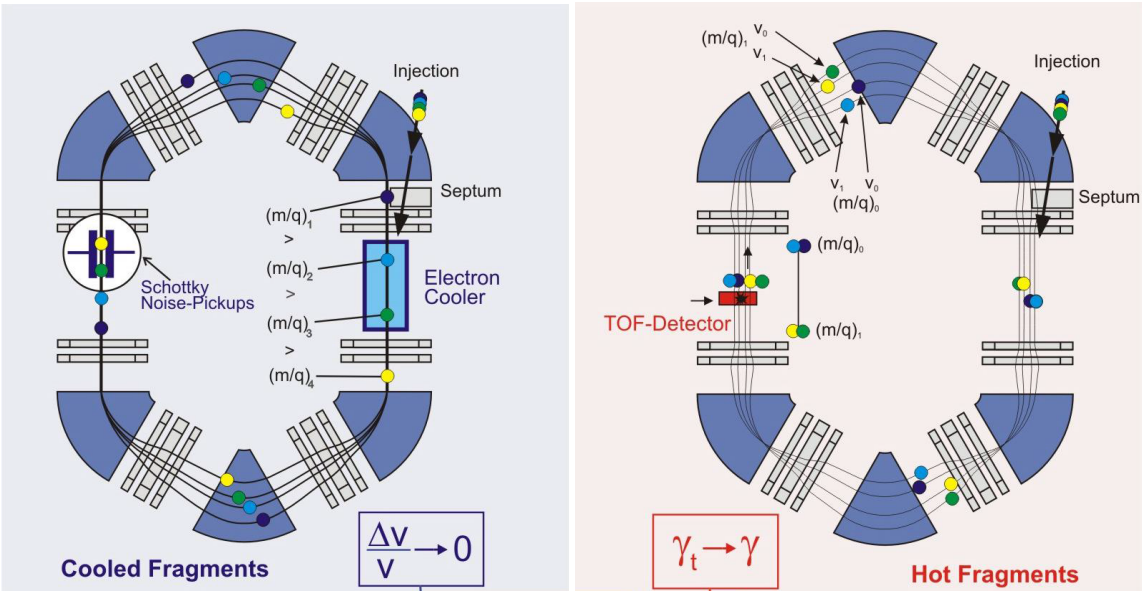

Figure 3.2: Mass spectrometry with the Experimental Storage Ring (ESR); Left panel: Schottky-Mass-Spectrometry – for long lived exotic nuclei ejected into ESR the phase space is reduce via electron cooling $\Delta v/v \approx 10^{-7}$. The measured revolution frequencies provide accurate mass-over-charge ratios independant on the velocity spread of the incident fragments; Right panel: Isochronous-Mass-Spectrometry – for short-lived nuclei electron cooling takes too long therefore the velocity spread is eliminated by properly tuned isochronicity [Diwisch, 2015].

(ending point). Ion species with same kinetic energy but different m/q differ in their flight time for a fixed path length and can be separated spatially. Each m/q does have a different time of flight for same kinetic energy and thus light ions are faster than heavy ions travelling the same path. To extend the spacial separation multiple reflection TOF-MS can increase the ion's flight path inside the so-called TOF analyser by performing multiple reflections inside the analyser. This is a break through the limited resolving power of linear or single reflector TOF MS and enables mass resolving powers $> 10^5$ and mass accuracies of $< 10^{-6}$. Multiple turns can be realised in different ways. Though the ions can perform the reflections in open or closed paths which mean they either travel in the analyser or use recycle the path for their given number of turns. (see figure 3.3) In addition there is the choice in letting the ions perform *turns* or *reflections* as sketched in figure 3.3. a, b, c show analyser for ion reflections realised with electrostatic mirrors [Tretner, 1959] [Wollnik and Przewloka, 1990] , d & e let the ions revolve in sector fields [Poschenrieder, 1972]

3.3 Time-of-flight mass spectrometry

The basic principle of time-of-flight mass spectrometry (TOF MS) is the separation of different mass-to-charge ratios (m/q) due to different velocities for the same

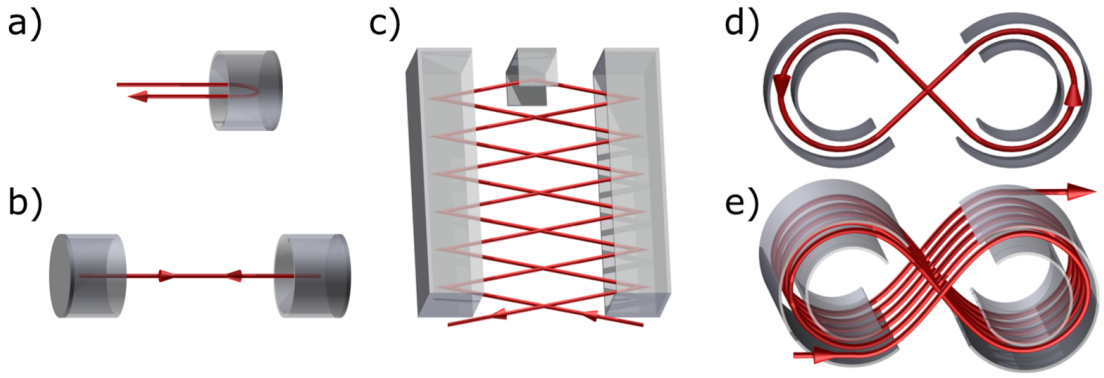

Figure 3.3: Different methods for TOF mass spectrometry. The goal is to prolong the flight path inside the different TOF analysers for high accuracy mass measurements; Panel *a*) single reflection device; Panel *b*) closed path analyser to achieve multi-reflections; *c*) open path analyser with multi-reflections; *d*) multi-turn analyser with closed orbits; *e*) open path analyser for multi turns. In courtesy of [Ebert, 2016]

kinetic energy:

$$E_{\text{kin}} = \frac{1}{2}mv^2 = qeU. \tag{3.5}$$

With the accelerating electrical potential U.

Principle of TOF analysers

With the first derivative of the path length – $v = s/t$ – and the ion's kinetic energy E_{kin} the time an ion spends inside the analyser can be described. The path length is given by the field free drift length inside the analyser l_{drift} and the velocity v resulting from equation (3.5)

$$t = \frac{l_{\text{drift}}}{\sqrt{\frac{2E_{\text{kin}}}{m}}}. \tag{3.6}$$

Since the acceleration to velocity v is depending on the charge-to-mass ratio and not on the ion's mass only the time-of-flight must be

$$t = \frac{l_{\text{drift}}}{\sqrt{\frac{2qeU}{m}}}. \tag{3.7}$$

In reality the TOF signal is not infinitely narrow but broadened gaussian like. This results from the thermal energy distribution of the ions in the preparation trap, that is not necessarily pointing in direction of the analyser at all times. The time the ions need to correct their flight direction during ejection is the so-called *turn-*

around time. The shape of the measured ion distributions is determined by two contributions, the turn-around time and ion optical effects. The turn-around time has a velocity distribution that is gaussian like, but the ion optical effects do not show a gaussian distributed behaviour in general, they are depending on several effects summarised as Δt_{IO}. Both contributions are independent so their single widths can be added quadratically

$$\Delta t = \sqrt{(\Delta t_{\mathrm{IO}})^2 + (\Delta t_{\mathrm{trap}})^2} \tag{3.8}$$

with the turn-around time contribution Δt_{trap}. The mass resolving power R_m of the device is then given by

$$R_m = \frac{m}{\Delta m} \tag{3.9}$$

using equations (3.5)–(3.15) for equation (3.9) follows

$$R_m = \frac{\Delta t_{\mathrm{trap}}}{2t} \propto \frac{1}{E_{\mathrm{kin}}} \tag{3.10}$$

$$\text{and} \qquad R_m = \frac{\Delta t_{\mathrm{trap}}}{2t} \tag{3.11}$$

If the ion passes the analyser N times the time-of-flight changes and an additional time factor comes into play.

$$R_m = \frac{{}^{t_0}\!/_{N_{\mathrm{turn}}} + t_{\mathrm{turn}}}{2 \cdot \sqrt{\left(\frac{\Delta t_0}{N_{\mathrm{turn}}}\right)^2 + (\Delta t_{\mathrm{turn}})^2}} \tag{3.12}$$

with t_0 as tof of zero turns in the analyser, t_{turn} is the tof needed for one turn but performing multiple turns and Δt_{turn} and Δt_{turn} the peak width after passing the analyser N times and just one time, respectively.

Mass range

The mass range of an ion beam inside the analyser differs in flight times and calibration modes, extremly. The range can be defined by the mass range selector that deflects unwanted ions, that revolution number is unequal to the defined number of turns N. If one special turn number is selcted the time-of-flight comes into play.

In reality the flight path an ion takes is not field free especially if ions travel on the edge of the mass range. That means charged particles are not blind for pulsed voltages like the analyser ejection potential. If ions see these potential they are pushed either forward or backward in time and this results in incorrect flight times which leads to impropable mass / TOF deterimination. A real mass range is defined to strongly avoid such effects. It differs from the ideal range in its effective analyser

length and for the real mass range m_{max}/m_{min} follows

$$\frac{m_{\mathrm{max}}}{m_{\mathrm{min}}} \leqslant \left(\frac{N_{\mathrm{turn}} + \lambda_{\mathrm{inj}}}{N_{\mathrm{turn}} + \lambda_{\mathrm{inj}} - (1 - \lambda_{\mathrm{mir}})} \right)^2 . \tag{3.13}$$

Where $\lambda_{\mathrm{inj}} = t_{\mathrm{inj}}/t_{\mathrm{turn}}$ describes the time from injection until the first mirror of the lower reflector and $\lambda_{\mathrm{mir}} = t_{\mathrm{mir}}/t_{\mathrm{turn}}$ is the time the ions are influenced by the pulsed reflector (ion optical mirror), both parameters are given in units of t_{turn}, see also [Yavor et al., 2015].

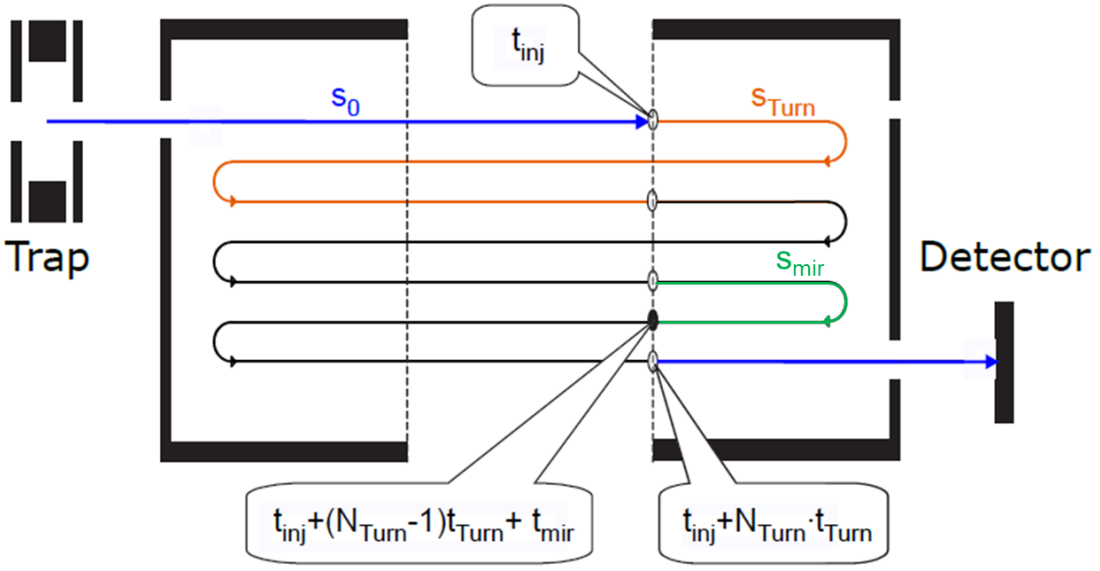

Figure 3.4: Schematic view of a time-of-flight analyser system consisting of an injection trap, a reflection system and a TOF detector. The ion's path length is divided into three parts relative to the position of the time foci. The corresponding flight times are given are represented by (t_{turn}, t_{inj}, t_{mir}). The condition for the maximum unambiguous mass range, as described in equation (3.13), follows from this illustration [Yavor et al., 2015].

For high accurate mass measurements either all components of the system (voltages, pulsing delays, ...) need to be very well known. The precision of these parameters need to be as good as the requested accuracy or better. Since this is not as easy to achieve the second possibility for mass determination is established, performing these kind of measurements with a reference mass. Though the system is calibrated such that the measured mass is relative to the calibrant mass, always.

Ions with velocity v fly a path of length s in the time of flight t. For the TOF –

mass correlation follows

$$\frac{1}{2}m\frac{s^2}{t^2} = qeU \tag{3.14}$$

$$m = at^2 \text{ with } a = \frac{2qeU}{s^2}. \tag{3.15}$$

For high injection fields the velocities effort a relativistic treatment and for the mass m follows

$$m_{\gamma 0} = \gamma m \tag{3.16}$$

$$\text{with the Lorentz-factor} \qquad \gamma = \frac{1}{\sqrt{1-\beta^2}} \tag{3.17}$$

$$\text{and} \qquad \beta = \frac{v}{c_0} \tag{3.18}$$

$$\tag{3.19}$$

with c_0 as the speed of light, m_γ the relativistic mass and the ion's mass at rest m. In case of a none relativistic treatment [Ebert, 2016] calculated the additional error of the measurements. With the conditions given in chapter 4 the probable error that must be considered is below 10^{-8} and thus can be neglected.

3.3.1 Calibration

Internal ion sources as described in chapter 4.2.2 are producing ions for measurement calibration. Taking equation (3.15) and express parameter a as

$$a(N_{\text{turn}}) = \frac{C}{(1 + N_{\text{turn}} \cdot b)^2} \tag{3.20}$$

$$m = \frac{C(t - t_0)^2}{(1 + N_{\text{turn}} \cdot b)^2} \tag{3.21}$$

witch includes an constant offset t_0 resulting from time delays, the number of turns N_{turn} and enables the mass calibration even for different turn numbers between calibrant and ion of interest [Ebert, 2016, Haettner, 2012]. Calibrating an MR-TOF MS with its different operation modes efforts several steps done with the program 'MAc' [Bergmann, 2015] [Pikhtelev, 2014].

t_0 **determination** For one measurement period t_0 stays constant, since it is a delayed caused by electronic issues. It is determined either by a spectrum with more than one calibrant or with a different spectrum (which is then mainly a no-turn spectrum)

Multi-turn calibration The final calibration of the recorded mulliple turn mass spectrum using equation (3.21)

TRC Termperature changes can lead to changes in voltages. Especially voltage

drifts at the MR-TOF analyer can lead to a time-of-flight shift of mass spectra. Therefore a time resolved calibration (TRC) is done. Thus the TRC drift corrects the mass spectra to avoid peak broadening and a loss in mass resolution, for more detailed information see [Ebert, 2016].

Binning

The correct binning of data is essential for reaching the optimal solution the data points can offer. Regarding at mass/time-of-flight data the lines are assumed to be gaussian shaped (compare page 17) and normal distributed around the real mass value. The Freedman-Diaconis rule is fitting for this type of data, it calculates an optimum binwidth h [Freedmann and Diaconis, 1981].

$$h = 2\frac{IQR(x)}{\sqrt[3]{N}} \tag{3.22}$$

with $IQR(x)$ the interquartile range of the distribution. The advantage of the IQR is the smaller sensitivity to outliers in data and describes the spread of data around the median.Comparing to the standard deviation which gives at $1\sigma \approx 67\%$ the IQR describes the 50% spread around the mean. The binning is sensitive to the region it must be but not to single events

3.3.2 Mass fitting

The fitting of MR-TOF MS spectra is done with the Hyper-EMG [Purushothaman et al., 2017]. It is a convolution of truncated exponential functions with a gaussian function. Three exponential tails are possible to add on each side, depending on the required peak shape that describes the data best.
For the right side it looks like

$$\begin{aligned}\frac{f(x)_{\text{right}}}{A_1} = \; & \frac{1}{2\tau_1} exp\left[\frac{x-x_0}{\tau_1} - \frac{\sigma^2}{2\tau_1^2}\right] erfc\left[\frac{x-x_0}{\sqrt{2}\sigma} - \frac{\sigma}{\tau_1}\right] \cdot (1-\eta_2-\eta_3) \\ & + \frac{1}{2\tau_2} exp\left[\frac{x-x_0}{\tau_2} - \frac{\sigma^2}{2\tau_2^2}\right] \cdot erfc\left[\frac{x-x_0}{\sqrt{2}\sigma} - \frac{\sigma}{\tau_2}\right] \cdot \eta_2 \\ & + \frac{1}{2\tau_3} exp\left[\frac{x-x_0}{\tau_3} - \frac{\sigma^2}{2\tau_3^2}\right] \cdot erfc\left[\frac{x-x_0}{\sqrt{2}\sigma} - \frac{\sigma}{\tau_3}\right] \cdot \eta_3 \end{aligned} \tag{3.23}$$

Left side:

$$\begin{aligned}\frac{f(x)_{\text{left}}}{A_2} = \; & \frac{1}{2\tau_1} exp\left[\frac{x-x_0}{\tau_1} + \frac{\sigma^2}{2\tau_1^2}\right] erfc\left[\frac{x-x_0}{\sqrt{2}\sigma} + \frac{\sigma}{\tau_1}\right] \cdot (1-\eta_2-\eta_3) \\ & + \frac{1}{2\tau_2} exp\left[\frac{x-x_0}{\tau_2} + \frac{\sigma^2}{2\tau_2^2}\right] \cdot erfc\left[\frac{x-x_0}{\sqrt{2}\sigma} + \frac{\sigma}{\tau_2}\right] \cdot \eta_2 \\ & + \frac{1}{2\tau_3} exp\left[\frac{x-x_0}{\tau_3} + \frac{\sigma^2}{2\tau_3^2}\right] \cdot erfc\left[\frac{x-x_0}{\sqrt{2}\sigma} + \frac{\sigma}{\tau_3}\right] \cdot \eta_3 \end{aligned} \tag{3.24}$$

With peak area A_1 and A_2 implementing the area (A) weighting of the exponential

tails with factor Θ while they are added up.

$$A_1 = A \cdot \Theta \tag{3.25}$$

$$A_2 = A \cdot (1 - \Theta) \tag{3.26}$$

The treatment of the data in general is explained and discussed in all details in [Ebert, 2016]. As a short summarise the steps are listed

- Determination of the peak shape parameters is done via least square and with the high statistics calibrant peak. The peak shaped of calibrant and IOI is defined to be the same. For a least-square fit the data is binned as discussed in paragraph before.
- Using the determined peak parameters the peak position of calibrant and IOI is determined with the maximum likelihood method for unbinned (list mode) data. This results in a final mass value for both mass lines.
- Parameter and systematic errors are determined in addition to the peak position using statistical tests.

t_0 Error contribution

In cases where t_{meas} is short and t_0 cannot be neglected it contributes to the total error of the measurement. Therefore general systematic investigations of the error contribution have been done for the particular case that

- calibrant and ion of interest do perform the same number of turns ($N_{\mathrm{cal}} = N_{\mathrm{ioi}}$)
- calibration is done with using one calibrant only

Taking equation (3.21) and the above listed constrains a system of equations needs to be solved.

$$m_{\mathrm{ioi}} = \frac{C(t_{\mathrm{ioi}} - t_0)^2}{(1 + b \cdot N)^2} \tag{3.27}$$

$$m_{\mathrm{cal}} = \frac{C(t_{\mathrm{cal}} - t_0)^2}{(1 + b \cdot N)^2} \tag{3.28}$$

It follows the final equation

$$m_{\mathrm{ioi}} = \frac{(t_{\mathrm{ioi}} - t_0)^2}{(t_{\mathrm{cal}} - t_0)^2}. \tag{3.29}$$

For the error contribution to the mass $\frac{dm}{m_{ioi}}$ the deviation $\frac{dm}{dt_0}$ needs to be built.

$$\frac{dm}{dt_0} = \frac{2m_{\mathrm{cal}}}{(t_{\mathrm{cal}} - t_0)^3} \left[(t_{\mathrm{ioi}} - t_0)^2 - (t_{\mathrm{ioi}} - t_0) \cdot (t_{\mathrm{cal}} - t_0)\right] \tag{3.30}$$

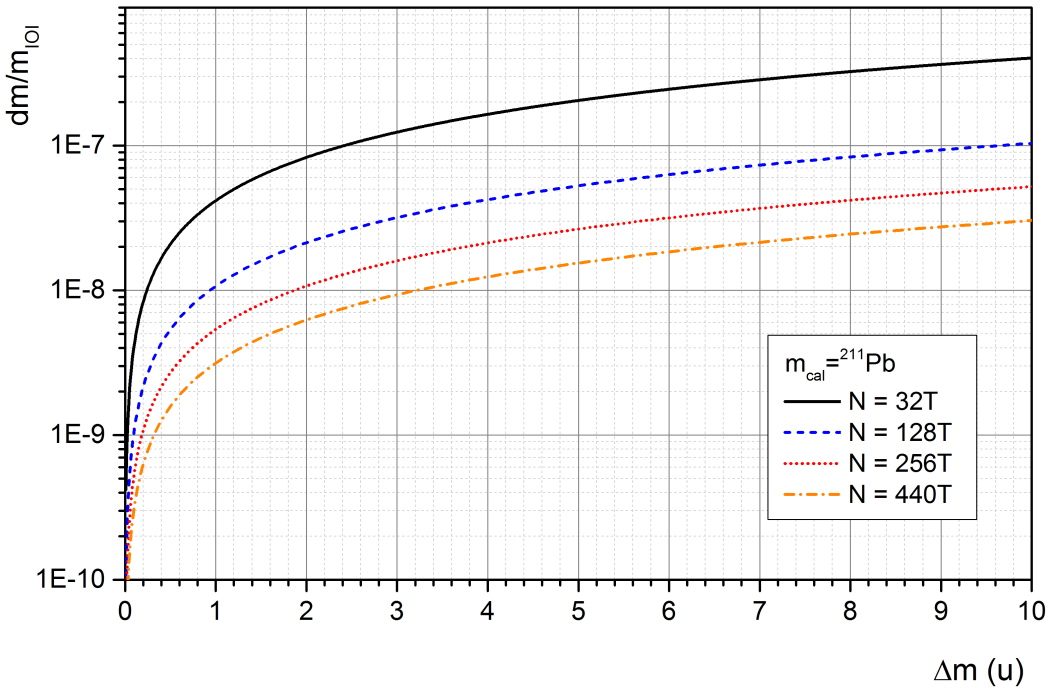

Figure 3.5: The contribution of the uncertainty of t_0 to the final mass accuracy for the mass difference Δm between the calibrant m_{cal} and the ion of interest. The calculations are done with equation (3.36) for the reference mass of ^{211}Pb isotope.

To determine t_0 depending on the mass difference $\Delta m = m_{\mathrm{ioi}} - m_{\mathrm{cal}}$ of the ion of interest and its calibrant. After some transformations and substitutions of

$$(t_{\mathrm{ioi}} - t_0)^2 = \sqrt{\frac{m_{\mathrm{ioi}}(1 + b \cdot N)^2}{C}} \tag{3.31}$$

$$(t_{\mathrm{cal}} - t_0)^2 = \sqrt{\frac{m_{\mathrm{cal}}(1 + b \cdot N)^2}{C}} \tag{3.32}$$

$$m_{\mathrm{ioi}} = \Delta m + m_{\mathrm{cal}} \tag{3.33}$$

follows

$$\frac{dm}{dt_0} = 2\frac{\sqrt{C}}{(1 + b \cdot N)} \left[\frac{m_{\mathrm{ioi}}}{\sqrt{m_{\mathrm{cal}}}} - \sqrt{m_{\mathrm{ioi}}} \right] \tag{3.34}$$

with

$$\frac{dm}{dt_0} = \frac{dm}{m_{\mathrm{ioi}}} \cdot \frac{m_{\mathrm{ioi}}}{dt_0} \tag{3.35}$$

$$\frac{dm}{m_{\mathrm{ioi}}} = 2dt_0 \cdot \frac{\sqrt{C}}{(1 + b \cdot N)} \left[\frac{1}{\sqrt{m_{\mathrm{cal}}}} - \frac{1}{\sqrt{\Delta m + m_{\mathrm{cal}}}} \right] \tag{3.36}$$

Figure 3.5 shows the relation between Δm and the t_0 error contribution as described in equation (3.36). For the plot the constants b, C are $b = 0.82\,\frac{\mu s}{u}$ and $C = 0,069\,u$ deduced from measurements.

3.3.3 Multiple-reflection time-of-flight mass spectrometer fast operation mode

For a fast but accurate mass measurement of a short-lived nuclei with an MR-TOF-MS the measurement time and the measured accuracy need to find an optimum. Since the ion of interest (^{215}Po, see chapter 7) does have a half-life of 1.781(4) ms only, the optimum MR-TOF cycle time t_{cycle} needs to be determined. The standard measurement time and frequency of the MR-TOF-MS is 20 ms and 50 Hz, respectively. That is more than ten times longer than the half-life of the targeted polonium isotope. Therefore the system needs to be faster.

For gaussian shaped peaks and a number of entries $N >> 10$ the accuracy of a measurement is

$$\frac{\delta m}{m} = \frac{1}{R_m} \tag{3.37}$$

where R_m is the mass resolving power defined as

$$R_m = \frac{m}{\Delta m(FWHM)} \tag{3.38}$$

at the full width half maximum $FWHM = \sigma \cdot 2,36$. The connection to the measurement time is reached with

$$R_m = \frac{TOF}{2\Delta T} \tag{3.39}$$

The number of survived ions (N_{TOF}) after they passed the MR-TOF MS (with cycle

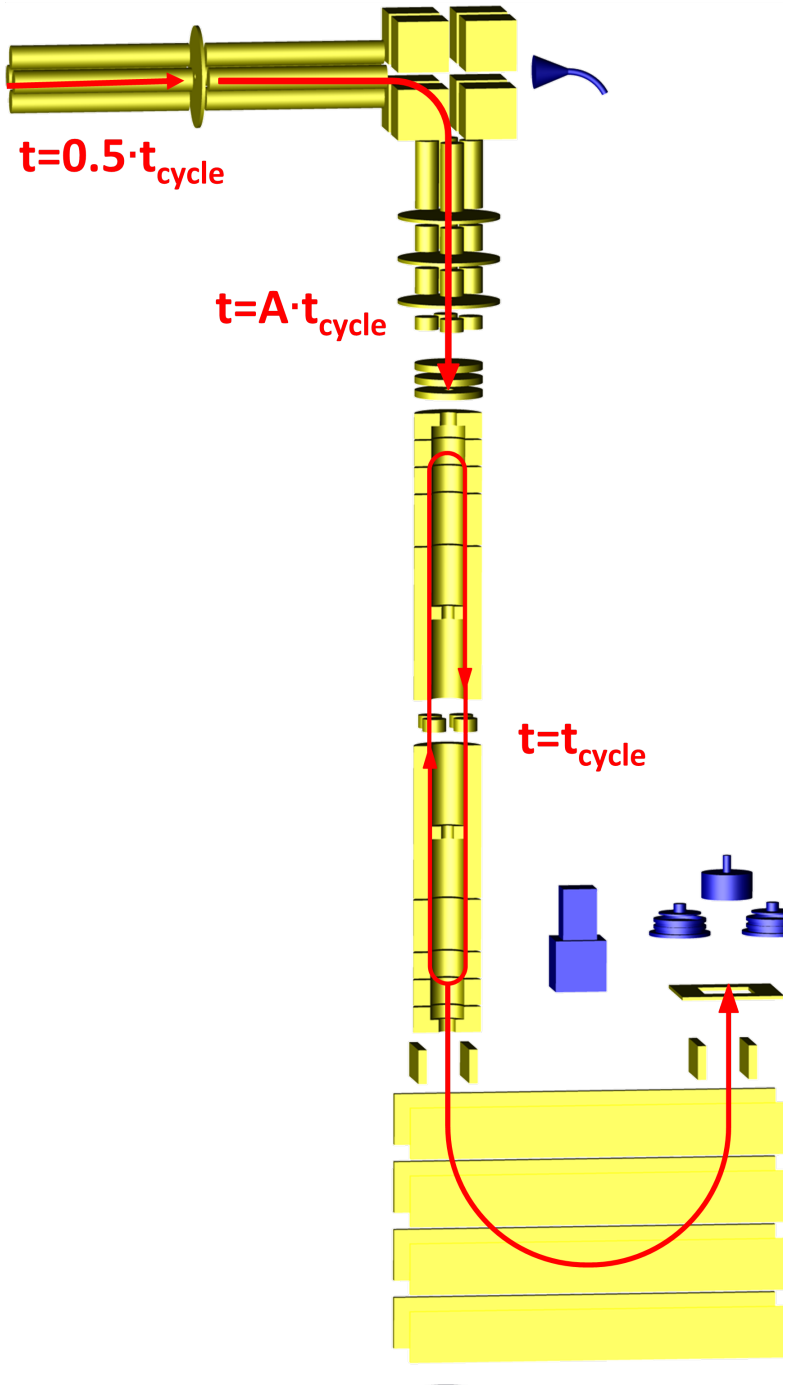

Figure 3.6: Ion path through the MR-TOF-MS. The red arrows indicate the stepp-wise transported ion beam. The first step is the apperture to enter the MR-TOF, the waiting timeof the ion is estimated to be $0.5 \cdot t_{\text{cycle}}$. The second step is the transport to the TOF analyser and the cooling in the last ion trap and is assumed to be $A \cdot t_{\text{cycle}}$, where A is a selected number of cycles in step 2. The last step is the mass measurement including the detection with $t = t_{\text{cycle}}$

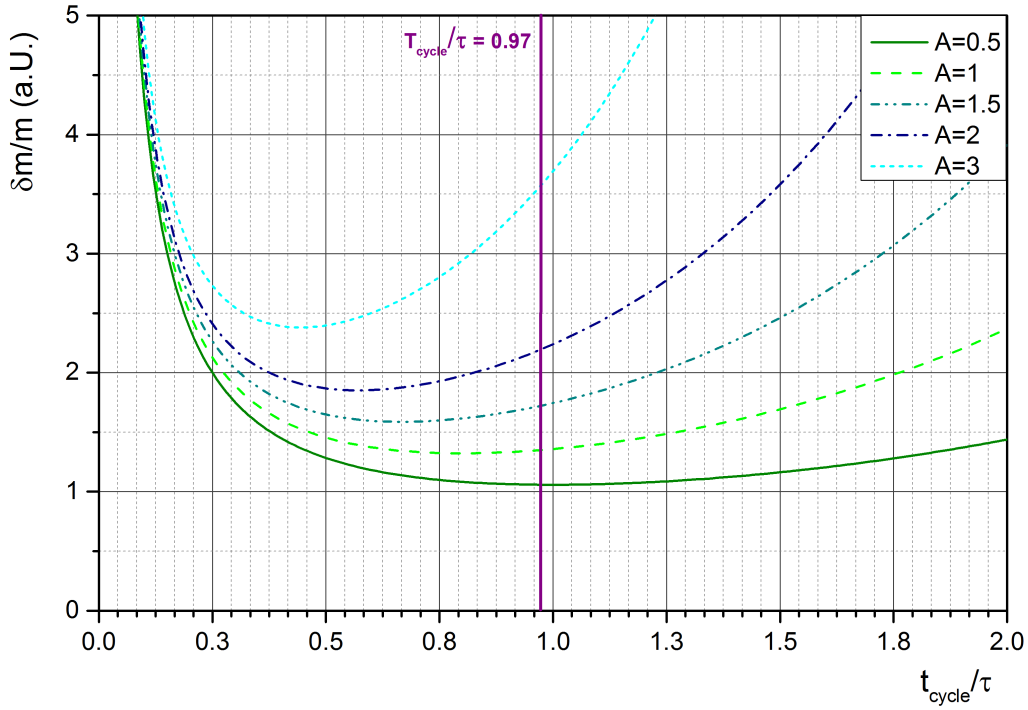

Figure 3.7: Calculated accuracy versus the t_{cycle}/τ for different measurement cycle times. For $t_{cycle}/\tau = 0.8$ it is the minimum of the green dotted line ($A = 1$) corresponding to one MR-TOF cycle for ion preparation plus one measurement cycle. The vertical line (purple) defines the $t_{cycle}/\tau = 0.97$ of the final measurements.

time t_{cycle}) is given by the law of radioactive decay

$$N_{TOF} = N_0 \cdot e^{-\frac{TOF}{\tau}} \tag{3.40}$$

$$\frac{\delta m}{m} = \frac{1}{2 \cdot \Delta T \cdot TOF \sqrt{e^{-\frac{TOF}{\tau}}}} \tag{3.41}$$

$$\text{with const}_1 = \frac{2 \cdot \Delta T}{2.36 \cdot \sqrt{N_0}} \tag{3.42}$$

$$\text{for } t_{cycle} = \frac{TOF}{\tau} \implies \frac{\delta m}{m} = \frac{\text{const}_2}{t_{cycle} \cdot \tau e^{-\frac{t_{cycle}}{2}}} \tag{3.43}$$

Until now only the decays in the MR-TOF MS have been taken into account. For simplicity reasons the regarded time is given in multiple of an MR-TOF MS cycle time $A \cdot t_{cycle}$ from now on. Thus the entire time an ion takes to reach the TOF detector. This number is composed of 0.5 cycles to enter the MR-TOF MS, A cycles to make it through the trap system and 1 cycle through the analyser to the detector,

as it is illustrated in 3.6.

$$\frac{\delta m}{m} = \frac{\text{const}_2}{t_{\text{cycle}} \cdot \tau \cdot exp(-\frac{1.5+A}{2} \cdot t_{\text{cycle}})} \tag{3.44}$$

The solution results from the partial derivative

$$\frac{\partial}{\partial t_{\text{cycle}}} \left(\frac{\delta m}{m} \right) = 0 \tag{3.45}$$

$$-\frac{1 - Bt_{\text{cycle}}}{t_{\text{cycle}}^2 \tau \cdot exp(-Bt_{\text{cycle}})} = 0 \tag{3.46}$$

$$\text{with } B := \frac{1.5 + A}{2} \tag{3.47}$$

since $t_{\text{cycle}} \neq 0 \wedge \tau \neq 0$ only the numerator is taken to account and it follows

$$t_{\text{cycle}} = \frac{TOF}{\tau} = \frac{2}{1.5 + A} \tag{3.48}$$

Typical dimension for A is $A = 1$, which leads to a cycle time $t_{\text{cycle}} \cong 0.8\tau$, where $\tau(^{215}\text{Po})$=2.569 ms. The accuracy versus t_{cycle}/τ is plotted for several A and is given in figure 3.7.

3.4 Determination of nuclear half-lives

Radioactivity is in general defined as a conversion of a nucleus into a lower energetic state by spontaneous particle emission. This lower energetic state can either be a decay from exited into e.g. a ground state by γ-emission or the emittance of particles e.g. αs or βs and so forth. This particles can either be light nuclei or fermions like electrons, positron, neutrinos or high energy photons. As a result in optimising the energy status of the nucleus it converts its excess energy into particles, this process happens spontaneously and induces e.g.

- γ-decay
- Fission
- β-decay
- α-decay

and sub-reactions. The higher the probability for such a transition to happen the shorter the life-time of the mother nuclide.

Mean life determination of radio-active nuclei in counting experiments e.g. decay spectroscopy can either be calculated as done in [Peierls, 1934] or be fitted.

In general the half-life of a nucleus is given as the time a certain number of nuclei N_0 has decayed to 50 % of its original amount. With the universal law of radio-active

decay

$$N(t) = N_0 \cdot e^{-t/\tau} \tag{3.49}$$

$$N(t) = N_0 \cdot e^{-\frac{ln(2)}{t_{1/2}} \cdot t}. \tag{3.50}$$

the remaining number of ions in time t, can be calculated or by forming the equation the decay constant λ can be determined. With $1/\tau = \ln 2/t_{1/2}$ follows the half life of the ion of interest.

$$s = \frac{\sum t_\nu}{m} \tag{3.51}$$

The sum describes the arithmetic mean of the distributed events which is an not weighted mean of the distribution, m is the total number of events. If the measurement time is large compared to the mean life, the mean life can be described by the arithmetic mean of the decay distribution fully, compare fig 3.8. Naturally, the time counting must start at zero. In the case the measurement period $T \simeq \tau$ or smaller the arithmetic mean s cannot describes the mean life τ accurately. The general relation between arithmetic mean s and mean life τ to calculate the ion's mean life is given in [Peierls, 1934]. It is calculated via the probability $p(t)$ for each decay happening. (It is $p(t)dt = 1$)

$$p(t)dt = \frac{1}{\tau} \cdot e^{-t/\tau} dt \tag{3.52}$$

and the measurement time T the arithmetic mean and mean life of an radioactive decay

$$s = \frac{\int_0^T t e^{-t/\tau} dt}{\int_0^T e^{-t/\tau} dt} \tag{3.53}$$

Integrating the time intervals and the consideration of the universal law of radioactive decay as described in equation (3.49) it follows for the mean life τ and the correction factor τ/s

$$s = \frac{\tau(\tau - e^{-T/\tau}(\tau - T))}{\tau - \tau e^{-T/\tau}} \tag{3.54}$$

$$\tau = \frac{T}{e^{T/\tau} - 1} + s \tag{3.55}$$

$$\frac{\tau}{s} = \frac{T/s}{e^{T/\tau} - 1} \tag{3.56}$$

where s is the calculated mean life from the data and a continuous integral $\int tdt$. If the factor T/τ is $\gg 1$ follows $s = \tau$ and no correction factor is necessary. Figure 3.8 shows the calculated result for s/τ vs. τ/T. If the measurements period is in the order of the expected mean life ($T \approx \tau$) equation (3.56) will be taken into account.

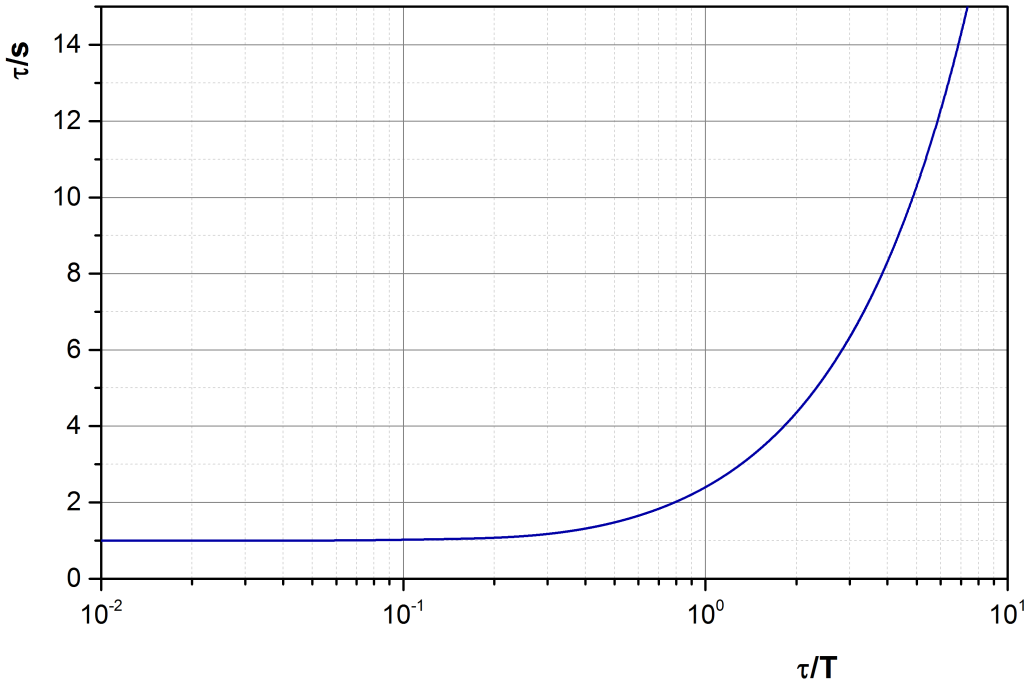

Figure 3.8: Numerical calculation of the behaviour of τ/s versus τ in units of the measurement time T. The plot is based on equation (3.56).

Error calculation

The error contribution for the half-life calculations are assumed to be given by the measurement period time and thus the not detected ones due to too short acquisition times T. In [Peierls, 1934] the error calculation is done in smaller steps and is given by the variance of the mean life equals the inverse number of entries $\delta\tau^2/\tau^2 = 1/N$ (whereas the final error estimation in this thesis will be done via the root mean square deviation).

Thus error contribution can be

- losses due to short measurement cycles
- additional counts resulting from dark counts (natural effects.)

The probability that τ has a certain value is given by

$$\mathcal{P}(\tau) = \sum_N P(N,\tau) = \text{const}\frac{1}{p}[f(\tau)]^m, \tag{3.57}$$

with the probability P for different number of counts N and the probability for a single event with a certain time p. For closer details please see [Peierls, 1934].

The mean square σ is defined from statistics and a Taylor expansion of f at $\tau = \tau_0$ [Peierls, 1934]

$$f = \frac{e^{-s/\tau}}{\tau(1-e^{-T/\tau})} \tag{3.58}$$

$$\sigma = m\frac{\delta\tau^2}{\tau^2} = -\frac{f}{f''} \tag{3.59}$$

$$\text{and the second derivative } \quad f'' = -\frac{f}{\tau^2}\left[1 - \frac{(\tau - s)\,(T - s + \tau)}{\tau^2}\right] \tag{3.60}$$

If the measurement time T is not much bigger than the expected life time τ the detected number of events m need to be corrected for the missed events ($N - m > 0$).

$$m = N\left(1 - e^{-T/\tau}\right) \tag{3.61}$$

where m gives the detected number as a function of the measuring time and considers none detected ions due to too short measurement cycles.

A "clean" detector without any radio active pollution does show dark counts with a certain rate "α". For the rate α we assume the appearance of dark counts is a statistical effect with a constant probability to appear at a time t_ν during the measuring time T. The count rate for mean life calculations thus consists not only of real decay signals but as an overlap of decay signals and dark counts. To consider and correct for the noise rate they are subtracted from the detected values and it results a weighted average for the arithmetic mean given by

$$s = \frac{m_\alpha s_\alpha - m_N s_N}{m_\alpha - m_N} \tag{3.62}$$

with m_α and s_α corresponding to the total number of real decay entries and m_N and s_N corresponding to noise on the detector due to the dark count rate. The variance $\delta\tau^2/\tau^2$ gets a correction term to consider the noise rate in addition.

$$\frac{\delta\tau^2}{\tau^2} = \frac{\sigma}{m} + \frac{1}{\tau^2}\left(\frac{d\tau}{ds}\right)^2 \delta s^2 \tag{3.63}$$

with the variance δs^2 calculate from equation (3.52)

$$\delta s^2 = \frac{\alpha\left[(T-s)^3 + s^3\right]}{3m^2} \tag{3.64}$$

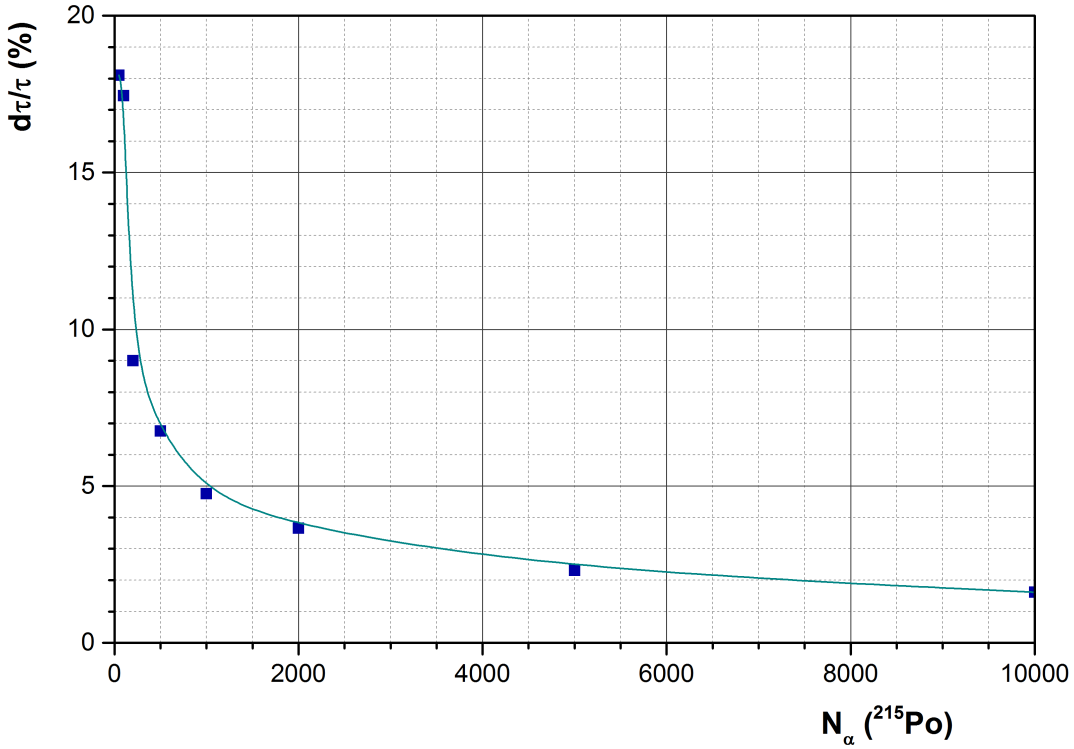

Figure 3.9: Calculated error distribution of the mean life depending on the data points. The graph shows the relative error contribution depending on the number of detected decays N_α. The blue line is meant to guide the eye.

and equation (3.59) follows

$$m\frac{\delta\tau^2}{\tau^2} = \sigma + \frac{\alpha}{3m}\sigma^2\left[\frac{(T-s)^3+s^3}{\tau^2}\right] \tag{3.65}$$

Extending (3.65) with τ/τ and sum up $N/\alpha\tau = \lambda$ and considering the total number of counts (see equation (3.61)) instead of the real ones only the error does look like

$$N\frac{\delta\tau^2}{\tau^2} = \frac{\sigma}{(1-e^{-T/\tau})} + \frac{1}{3\lambda}\left(\frac{\sigma}{(1-e^{-T/\tau})}\right)^2\left[\frac{(T-s)^3+s^3}{\tau^3}\right] \tag{3.66}$$

For a complete error estimation the binning needs to be considered as well. Thus the Taylor expansion is done around the interval size $t = d$.

$$s = \frac{1}{m}\sum_i n_i\left(t_i + \frac{1}{2}d\right) - \frac{1}{12}\cdot\frac{d^2}{\tau} + \frac{23}{360}\cdot\frac{d^4}{\tau^3} \tag{3.67}$$

for $d \ll 0.3\tau$ the last terms become comparatively small and can be neglected

In our case the standardised way to give error contributions is the deviation $\delta\tau/\tau$ of value τ. In figure 3.9 the number of events is plotted versus the relative deviation of the mean life. The light blue line is given to guide the eye. For short measurement times as it is calculated in section 3.3.3 the relative error contribution raises up to 18 % for poor statistics. With high statistics the error contribution is at $\sim$ 2 %, which means the combination of short measurement cycle time and low statistics result in high error contributions to the final value.

Artefacts in the data acquisition

If the taken data is not continuous but interrupted for any reasons and data points at that specific time may not be considered the integral in equation (3.53) has to be re-written in a way to part it into the different time intervals t_i depending on the number of artefacts during the data aquisition.

$$\bar{s} = \frac{\int_0^{t_1} te^{-t/\tau}dt + \int_{t_2}^{t_3} te^{-t/\tau}dt + \cdots}{\int_0^{t_1} e^{-t/\tau}dt + \int_{t_2}^{t_3} e^{-t/\tau}dt + \cdots} \tag{3.68}$$

resulting in a cut between e.g. t_1 and t_2 in time where no contributions are taken in to account for the estimation of the arithmetic mean and mean life. With these *cut outs* equation (3.56) thus looks like

$$\begin{aligned} \textit{denominator} &= \left[\tau(-e^{-t/\tau})(\tau+t)\right]_0^{t_1} + \left[\tau(-e^{-t/\tau})(\tau+t)\right]_{t_2}^{t_3} \\ &\quad + \left[\tau(-e^{-t/\tau})(\tau+t)\right]_{t_4}^{t_5} \\ &= -\tau\left[-\tau + e^{-t_1/\tau}(\tau+t_1) - e^{-t_2/\tau}(\tau+t_2)\right. \\ &\quad \left. + e^{-t_3/\tau}(\tau+t_3) - e^{-t_4/\tau}(\tau+t_4) + e^{-t_5/\tau}(\tau+t_5)\right] \end{aligned} \tag{3.69}$$

$$\begin{aligned} \textit{enumerator} &= -\tau\left[e^{-t/\tau}\right]_0^{t_1} - \tau\left[e^{-t/\tau}\right]_{t_2}^{t_3} - \tau\left[e^{-t/\tau}\right]_{t_4}^{t_5} \\ &= -\tau\left[-1 + e^{-t_1/\tau} - e^{-t_2/\tau} + e^{-t_3/\tau} - e^{-t_4/\tau} + e^{-t_5/\tau}\right] \end{aligned} \tag{3.70}$$

Combining denominator and enumerator the arithmetic mean can be calculated with the following expression

$$s = \frac{\sum_n(-i^{2n}(\tau+t_n)e^{-t_n/\tau}) - \tau}{\sum_n(-i^{2n}e^{-t_n/\tau}) - 1} \tag{3.71}$$

In graphic 3.10 an exemplary curve is plotted, it contains three parts between $0-t_1$, t_2-t_3 and t_4-T and the neglected artefacts in between.

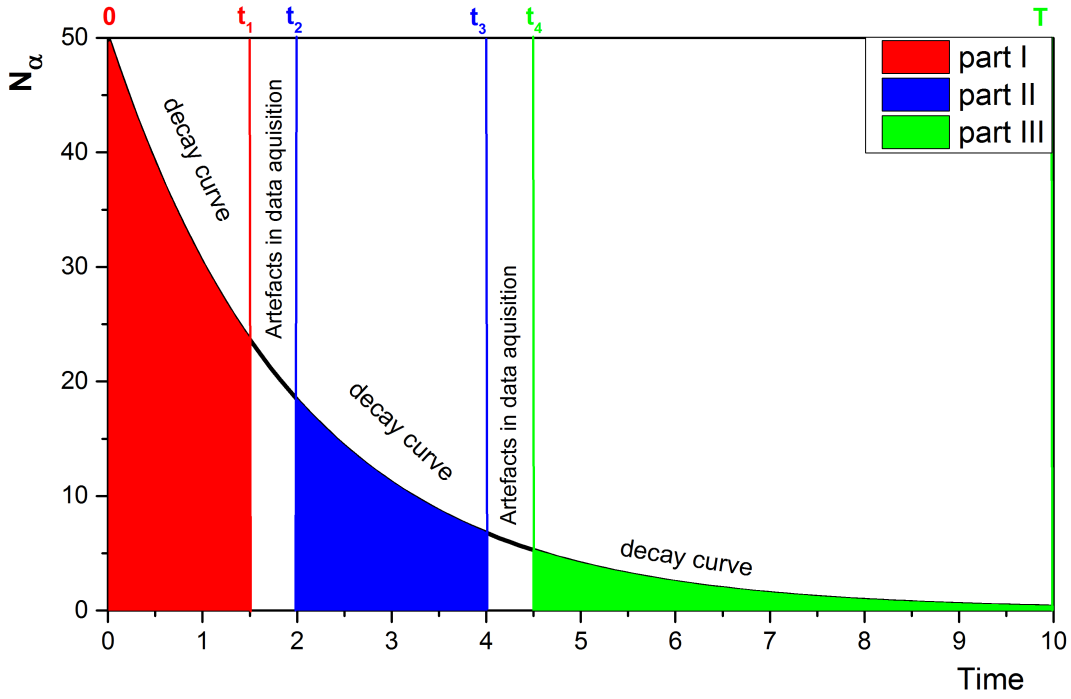

Figure 3.10: The graph shows a typical decay curve with artefacts that should be neglected in the evaluation process. The measurement time is T, the intervals $t_1 - t_2$, as well as $t_3 - t_4$ are removed in the analysis. Regarding at equation (3.68) in this case $i = 5$ where $t_5 = T$.

3.5 Extraction and transport time measurements

The extraction times describe a time ΔT the ions need to travel from the ion source inside the stopping cell until their decay is recorded Si-surface barrier detector implemented in the RFQ beam line. Somewhat similar to time-of-flight measurements a reliable start point $T = t_{\text{start}}$ and a stopp signal $T = t_{\text{stop}}$ is necessary. For experiments with radioactive ion beams a clear signal for the beam entering the stopping cell is difficult and was not implemented for the on-line experiments. In 2014 the only time information given is the "spill-start" signal, when the ion beam exits the accelerator and enters the FRS. The extraction of ions is assumed to happen without decay losses (see [Purushothaman et al., 2013] and [Reiter, 2015])

For an ion beam of an off-line measurement start and stop signal are defined clearly. t_{start} is the time the off-line source is switched on and t_{end} -as before- the detector signal resulting either from the decay (Silicon-detector) or from hitting (TOF-detector).

Quite contrary to the definition of the extraction time in [Purushothaman et al., 2013] (t_{extr} = mean time of extracting through the complete stopping cell) the off-line measurements defines t_{extr} as the time the first ion is detected. To say it another way the moment the number of entries starts raising. For calculations the following assumptions are made

- when the source is switched off, no ions of that species are extracted
- during the 'on' period of the source the extraction rate P is constant

According to equation (3.49) the extraction profile detected with a silicon detector (α-detector) is described in three intervals

$$N_\alpha = \begin{cases} B & \text{for } t < t_{\text{extr}} \\ B + N_\alpha \left(1 - exp\left(-\frac{ln2}{\tau}(t - t_{\text{extr}})\right)\right) & \text{for } t_{\text{extr}} \leq t \leq t_{\text{on}} \\ B + N_\alpha \left(1 - exp\left(-\frac{ln2}{\tau} t_{\text{on}}\right)\right) \cdot exp\left(-\frac{ln2}{\tau}(t - t_{\text{extr}} - t_{\text{on}})\right) & \\ & \text{for } t > (t_{\text{extr}} + t_{\text{on}}) \end{cases} \tag{3.72}$$

with background B, amplitude (decay to population equilibrium) N_{alpha}, half-life τ, extraction and source-on time t_{extr} & t_{on}, respectively. For $t_{\text{extr}} > t$ no ions can be detected, the ions are not extracted yet, $N = 0$. The setup is triggered in two different ways to meet the requirements of different data acquisition systems.

(a) To measure extraction times only a silicon detector (surface barrier detector) is used.

(b) In the second case a TOF detector in the mass spectrometer is used to measure the extraction and transport time through the complete system.

The pulsing scheme of (a) is sketched in figure 3.12a. The data acquisition is resetted for each measurement cycle, which is given by the duty cycle of the pulsed source. Each time the source is pulsed high the clock of the DAq is reset to zero and started again. The software is programmed to start acquisition by the first incoming signal after the time reset (CAEN reset) such that an artificial trigger signal starts

the clock again (CAEN trigger).

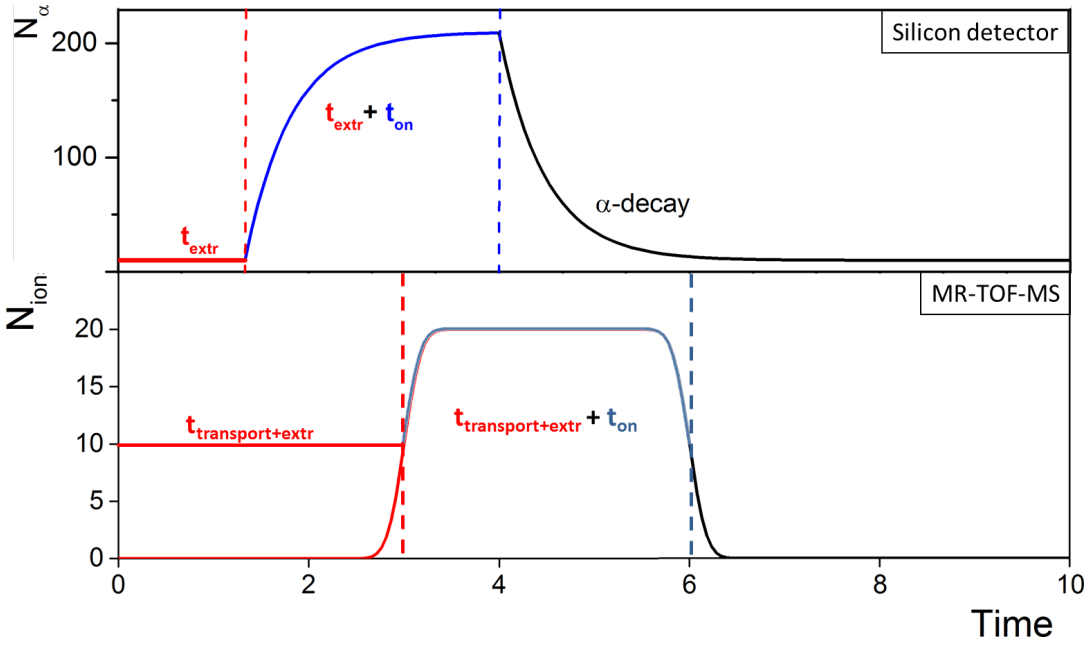

Figure 3.11: Top panel: Fit function for extraction time measurements as described in equation (3.72); Bottom panel: Fit function for extraction and transport time measurements for the complete system as discussed in equation (3.73)

For method (b) the pulsing scheme needs to be modified to fit in. The sketched trigger scheme can be taken out of figure 3.12b. The DAq is triggered by the MR-TOF-MS cycles, that source and MR-TOF-MS cycles are correlated. In addition a trigger signal is given to the TDC which is one entry each cycle (TDC Gate) but the last five signals of a measurement cycle to have a clear start time. The two different data acquisition modes require thus a different fit. For the MR-TOF-MS transport time spectrum of ions being extracted from the CSC is described by a function of two added up error functions, see figure 3.11 bottom panel. The 50 % value gives the wanted time and the distance between both half-maxima of the two functions correspond to the extraction duration (the "on time" of the ion source).

$$N_{\text{ions}} = \frac{N}{2} + \frac{N}{2} \cdot (\mathbf{Erf}(\lambda \cdot t - d_{\text{rise}}) \cdot \mathbf{Erf}(-\lambda \cdot t + d_{\text{falling}})), \tag{3.73}$$

where λ describes the rising and falling edge, respectively. d_{rise} and d_{falling} mark the shift in time of the error function at 50 % height, which corresponds to the transport time and the duration of ion extraction, respectively. The extraction time t_{extr} is then given by d_{rise}/λ.

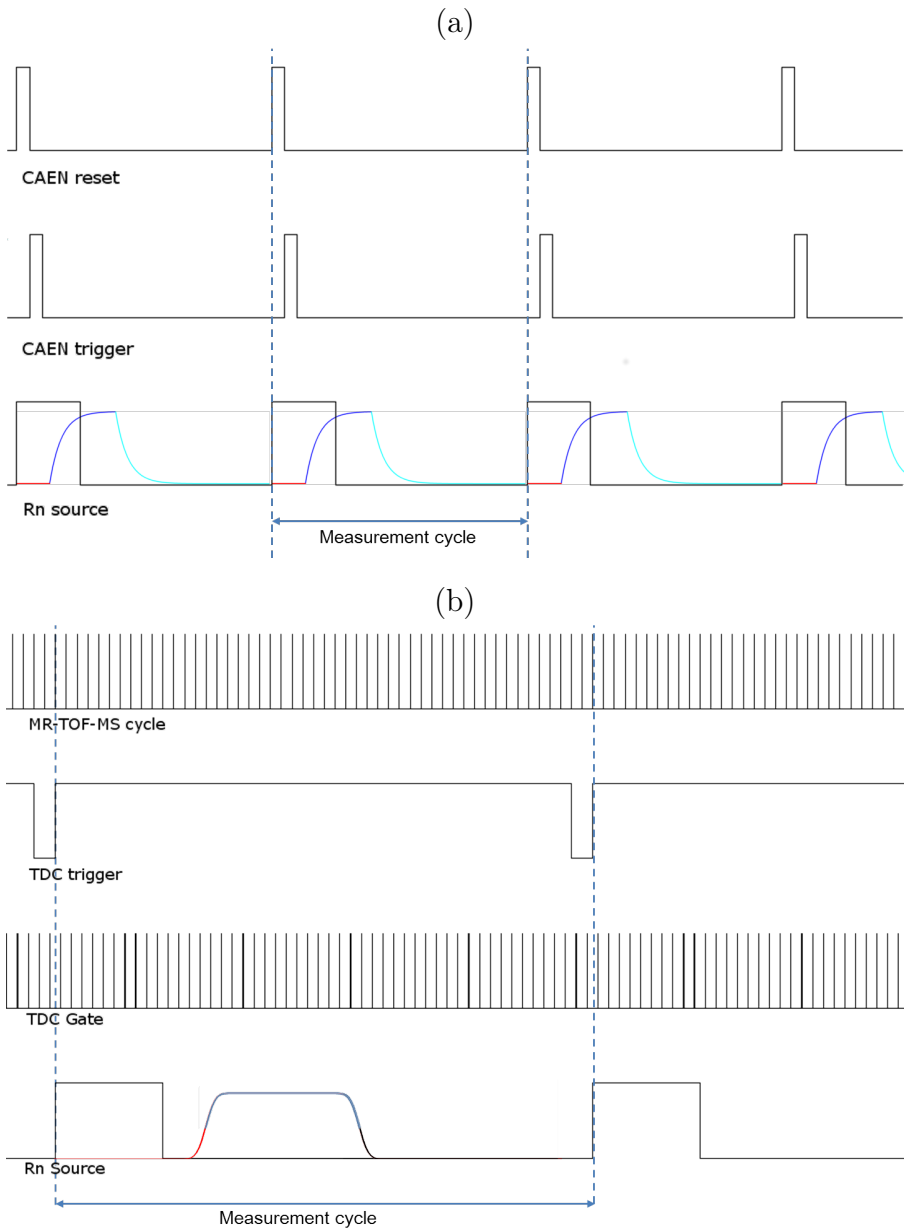

Figure 3.12: Schematic drawing of the pulsed data acquisition for extraction time measurements.
(a) Trigger scheme for the silicon detector located behind the extraction RFQ of the CSC; The ion source runs with a constant frequency applied and triggers the data acquisition. The CAEN software gets a time reset signal to set the time counter to zero and a start signal to start the time counting for each measurement cycle.
(b) Trigger scheme for extraction time measurement at the MR-TOF-MS TOF-detector; The MR-TOF-MS cycle signal pulses the other trigger signals, the TDC fake signal produces one entry for each MR-TOF cycle and the TDC trigger registers the signal if it is switched high, the ^{223}Ra source is triggered by the MR-TOF-MS cycles and runs for a defined measurement cycle.

4 Experimental setup

The FRS Ion Catcher experiment [Plaß et al., 2013a] is a test facility for the Low Energy Branch (LEB) of the Super-FRS at FAIR and was developed and commissioned successfully at GSI. The current setup at the fragment separator consists of a cryogenic stopping cell including an RFQ beam line with implemented tools for beam diagnostics and an MR-TOF-MS which can be used for detection and identification, high precision mass measurements and separation of isotopes thermalised and extracted from the cryogenic stopping cell. The schematic view of the complete setup (FRS + Ion Catcher) is shown in figure 4.1.

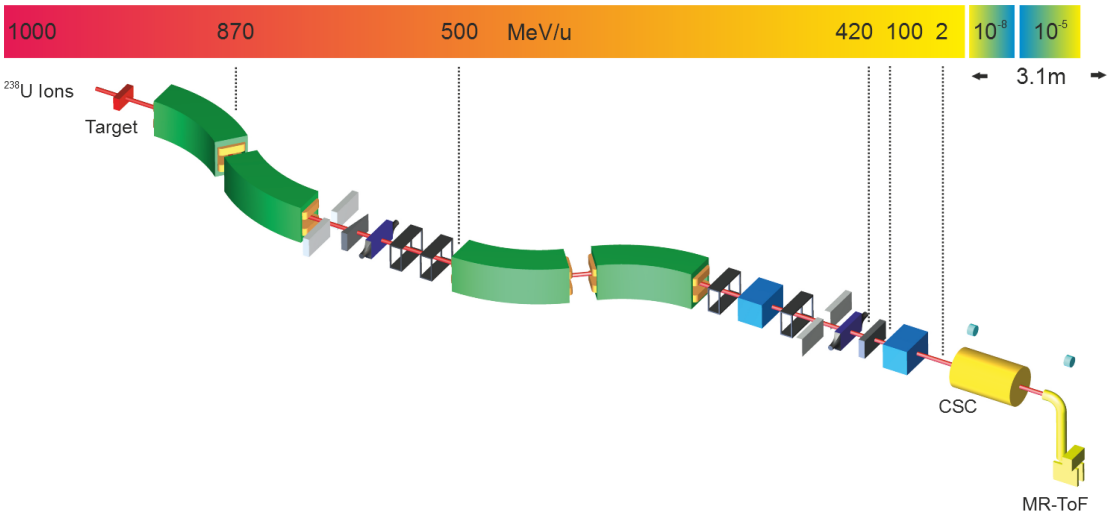

Figure 4.1: The Fragment Separator (FRS) produces and separates exotic nuclei in-flight. The energy scale on top indicates the different slowing down phases. The incident 1000 MeV/u uranium projectile beam is focused on the target at the entrance of the FRS. The four dispersive stages of the FRS are indicated by the four dipole magnets (green). In the midplane and final focus aluminium degraders (grey) are positioned to slow down the fragments before they enter the CSC and the MR-TOF-MS system (yellow) [Purushothaman et al., 2013].

4.1 The GSI fragment separator FRS

The Fragment Separator (FRS) [Geissel et al., 1992] [Münzenberg, 1992] is a large ion optical spectrometer, located behind the "Schwerionen Synchrotron" (SIS 18)

which handles all kind of ion beams up to energies of 4.5 GeV/u. Secondary beams are produced either in projectile fragmentation or in projectile fission as shown in chapter 3.1.2. In the presented measurements a Beryllium target was taken for production. For separation four 30° dipole magnets in combination with quadrupole magnets installed in front of and behind each dipole magnet are set up. The separation mechanism that is used is the so called $B\rho - \Delta E - B\rho$ method. The produced fragments have a certain momentum spread and can be sorted by the magnetic field and slits ($B\rho$), on the middle focal plane (dispersive focal plane). The ions in the second part of the separator pass a monochromatic degrader system to separate the ions via their energy loss in matter (ΔE) [Geissel et al., 1989].

For identification of the ion / region of interest several detectors are implemented in the beam line. The identification in A and Z is done via time-of-flight measurements from the middle focal plane to the final focal plane of the FRS. Energy loss (ΔE) and coincidence measurements in Multiple-Sampling Ionisation Chambers as well as position measurements on both focal points are used to calculate the $B\rho$ that is necessary to determine the A/Z of each fragment.

4.2 Cryogenic stopping cell

The cryogenic stopping cell [Ranjan et al., 2011] [Reiter, 2015] [Purushothaman et al., 2013] is located directly behind the FRS final focal plane. It is made of an outer vacuum chamber enclosing and isolating the inner cryogenic chamber of the stopping cell (see figure 4.2). After thermalising the ions are guided via an DC field applied on the ring electrodes to the radio-frequency extraction structure called the RF-carpet and are extracted in beam direction. The ring electrodes consist out of stainless steel and form a cage structure (DC cage) with overlapping rings. They have a diameter of 25 cm for the inner laying rings and 27 cm for the outer positioned rings. The rings are connected via 3.3 MΩ resistors to generate a DC gradient pointing in direction of the radio-frequency (RF) carpet. The full cage length for highest stopping efficiency as shown in figure 4.2 contains 36 rings. With a stopping volume of 1.045 m length and 0.25 m in diameter, thermalising, extraction and measurements with exotic nuclei in combination with the degrader system at the FRS, is possible. Stopping and extracting these high energy ions with high efficiencies requires high density buffer gas. For the on-line operation in beam time 2014 the areal density went up to 5 mg/cm^2 for measurements. A variable off-line ion source is mounted on the beginning (beam entrance window) to have transport through the full cryogenic chamber and an electrical discharge ion source is mounted in the last third of the DC cage (see 4.2.2).

Experimental parameters

The measurements presented in chapter 5 have been taken under specific conditions that are listed the following in table on page 40. The data presented is taken during two commissioning experiments in 2012 and 2014. For data acquisition in 2012 a

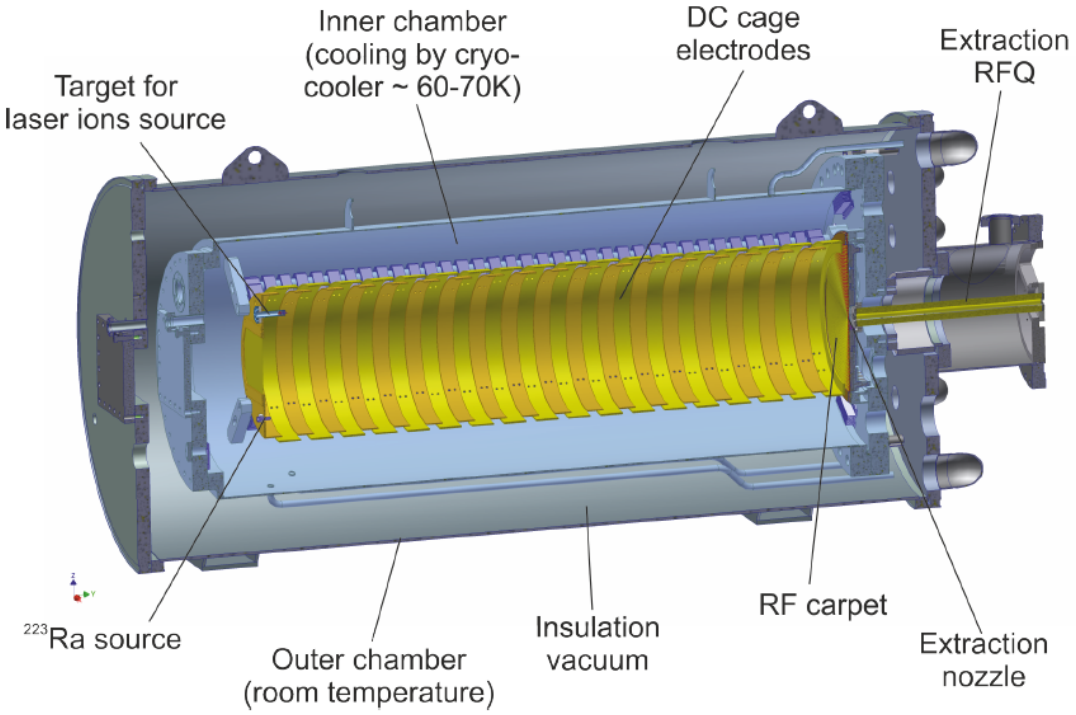

Figure 4.2: Profile drawing of the cryogenic stopping cell. It shows the outer chamber surrounding the cryogenic chamber. The cryogenic chamber is the beam stopping region that includes the DC cage with 36 DC ring electrodes to transport the stopped ions through the He gas in direction of the RF carpet and extraction nozzle. To maximise the stopping efficiency, the he gas density is increased by the operation at temperatures around 70 K. [Reiter, 2015]

Si-detector was mounted in the RFQ beam line and was used together with the CAEN software saving timestamps for each ^{221}Ac event. In 2014 a different nuclide (^{213}Fr) was chosen and detected in pass through mode with the MR-TOF-MS (see page 46).

The high rate studies have been made for two different voltage settings along the DC cage to investigate the extraction behaviour depending on the extraction field strength and with that the extraction times. For ion extraction two DC fields have been chosen for each data set (see table on page 40 for more details).

4.2.1 RF-carpet

The RF-carpet has a diameter of 25 cm and is equipped with 500 ring electrodes that are connected via an 100 $k\Omega$ resistor chain to provide a radio-frequent field. An extraction nozzle located in the middle of the carpet releases the ions from the CSC. As shown in figure 4.3 the carpet does contain nine layers to provide a stable operation. The first one is the layer of ring electrodes followed by a layer of isolating

DC Voltage	RF Carpet		Temperature	Pressure	Areal Density	Internal source
$[V]$	DC $[V]$	Amplitude $[V_{pp}]$	$[K]$	$[mbar]$	$\left[\frac{mg}{cm^2}\right]$	status
1500	50	22	75	49	3.2	on
2500	60	22	75	48	3.2	on

CSC settings that where used for the rate capability studies during the experiments in 2012 with an ^{221}Ac beam detected with the Silicon detector in the RFQ beam line behind the CSC.

DC Voltage	RF Carpet		Temperature	Pressure	Areal Density	Internal source
$[V]$	DC $[V]$	Amplitude $[V_{pp}]$	$[K]$	$[mbar]$	$\left[\frac{mg}{cm^2}\right]$	status
1100	80	79	86	63	3.7	on
2200	80	78	86	63	3.7	on

CSC settings that where used for the rate capability using an ^{213}Fr beam studies during the experiments in 2014 detected with the MR-TOF-MS TOF detector.

Table 4.1: Setting of CSC operation during the rate-capability studies in 2012 and 2014.

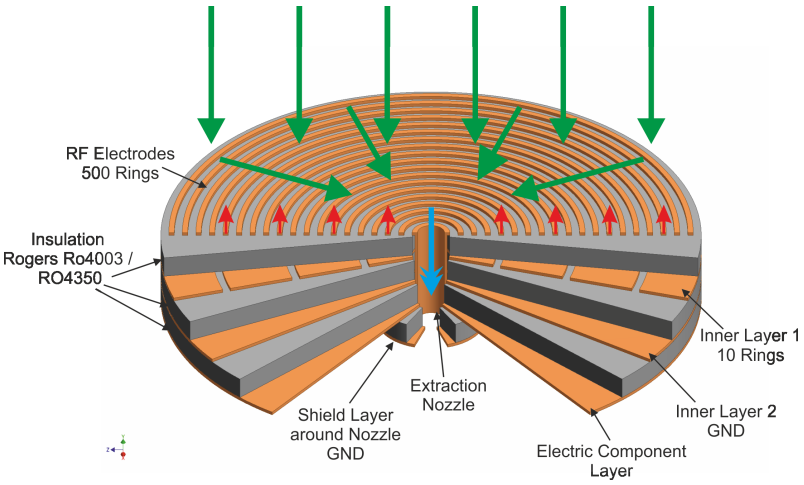

Figure 4.3: Schematic drawing of the RF-carpet shows a cut through the different layers of the device. Grey parts are isolation material, orange marks electrodes (either DC or RF). The arrows in green and red indicated the DC field and the RF field, respectively, whereas the blue arrow illustrate the gas flow through the extraction nozzle. [Reiter, 2015]

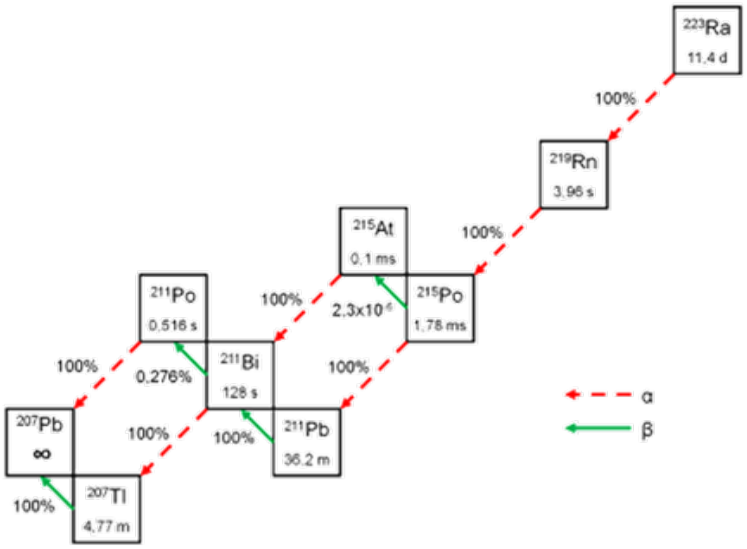

Figure 4.4: Decay path of the ^{223}Ra nuclide to stability

material (Rogers Ro4003/RO4350) to protect the different electrical layers from touching each other. The RF structure and its insulation is followed by two inner layers again separated by the insulation material. Inner layer number one is departed into 4 rings connected via a DC chain and it is possible to apply different voltages on the outer and inner ring and use the connection via a resistor chain as voltage divider. It supplies the a DC field along the RF carpet which can be at constant voltage or have a DC gradient. Inner layer number two is a grounded layer to shield the electric components that are placed on the back layer. The last layer is not the full carpet size, it shields the extraction nozzle from electronics and protects it from possible electrical discharges.

4.2.2 Internal ion sources

Radioactive ion sources

The main ion source for off-line operation has been the ^{223}Ra source. ^{223}Ra belongs to the Actinium decay-series its decay chain is shown in figure 4.4. The source delivers 7 short-lived daughter nuclei that can be used to test and optimise the ion extraction of the CSC and transport via RFQs to the different detectors. With the direct daughter ^{219}Rn it is possible to determine transport and extraction efficiency of the system off-line. The source is mounted on a motor driven arm to be able to change the radial stopping position of the ions. It reaches about 5.5 cm into the stopping region, positioned off beam axis ($\sim$ 11 cm radial offset) it disturbs an incoming ion beam as less as possible.

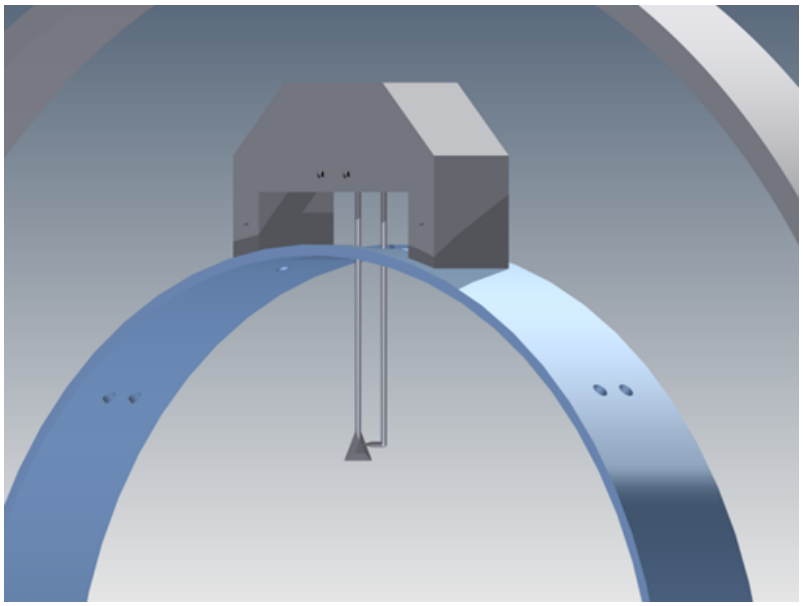

Figure 4.5: Electrical discharge source mounted on the 25^{th} ring of the DC cage. It ignites a discharge and ionises the residual gas around for either testing the cleanliness of the system or studying the reliability of the system under space charge conditions.

Laser ablation ion source

A laser ablation ion source was developed and commissioned [Rink, 2012] to investigate transport and extraction alone the RF-carpet element specific. Therefor a motor driven target wheel was mounted on the entrance flange behind special laser window.

Electrical discharge source

Another source installed at the CSC is an electrical discharge ion source which delivers ions by producing a discharge between two electrodes formed as a needle and plate. [Greiner, 2013] For production of ions over a broad mass range at variable intensities this source can be used for investigations on high intensity beams and in addition space-charge behaviours. Mass dependent transport to carve out territories of interest for on-line experiments can be done with ions from the ionised residual gas as well. The ion source itself does produces ions of gas components and contaminants and give a good estimation on the cleanliness of the cryogenic system itself. Especially for studies concerning space charge effects like ion transport along the disturbed DC fields of the DC cage and the RF-carpet behaviour can be studied.

4.2.3 Cryostat

The cryostat [Ranjan et al., 2015] delivers the cold Helium gas to cool down the stopping volume of the stopping cell. It consists of a compressor - cold head combination for cooling down the gas in a cooling loop, a cryofan that circulates the He-gas through the system and a heat exchanger to pre-cool the buffer gas before it enters the CSC. In addition it has an implemented dewar for liquid Nitrogen (LN_2) that procure additional cooling capability for the He-gas cooling loop. The filled dewar provides cooling power that enables especially in the beginning of the cooling cycle a faster cool down. There are four couplings for two cooling lines wrapped around the inner chamber to cool down the vacuum vessel. They built a closed loop that uses $5 - 6$ bar He to keep the system cold.

4.2.4 System upgrades

Short cage CSC

For fast operation experiments as proposed for the final version stopping cell for the LEB at FAIR [Rodriguez et al., 2010] [Dickel et al., 2016] the ion's path length through the He buffer gas was shortened drastically from about 1 m down to ~ 7 cm. Therefore the ring structure of the DC electrodes was shortened from 36 rings to 4 DC electrodes as illustrated in figure 4.6. In addition to the reduction of the rings sources and diagnostics tools (electrical discharge ion source, movable Laser ablation ion source, residual gas analyser, getter pump) have been removed to protect them from high field conditions and possible electrical discharges. Due to these reductions it is possible to apply higher extraction DC fields on the set up. Having less than $^1/_{10}$ of the original path length the extraction time is also expected to be shortened the same way and opens the possibility to measure short-lived nuclei, see chapter 7. With an flight path dominated by ions travelling along the RF-carpet conclusion about the transport time along the RF-carpet can be drawn. Therefor the radioactive ^{223}Ra source was mounted in two different positions using the movable source mount (see below). The first position was on beam axis, directly in front of the extraction nozzle of the RF carpet. The second position was 7 cm off beam axis, so that ions need to be transported by the RF-field along the RF-carpet ~ 7 cm to the nozzle. Checking the transport (extraction times, RF-amplitudes of the RF-carpet at varied densities and DC fields along the ring electrodes) for different source positions give conclusions about possible limitations of the next-generation stopping cell and its perpendicular extraction as explained in chapter 5.

Experimental parameters

The systematic studies have been performed for up to seven different densities and voltages between 150 V and 750 V. For source positioned off the beam axis the RF-carpet inner layer voltage was scanned in addition. Goal of this parameter variation was the systematic check if this voltage does influence the ion transport along the

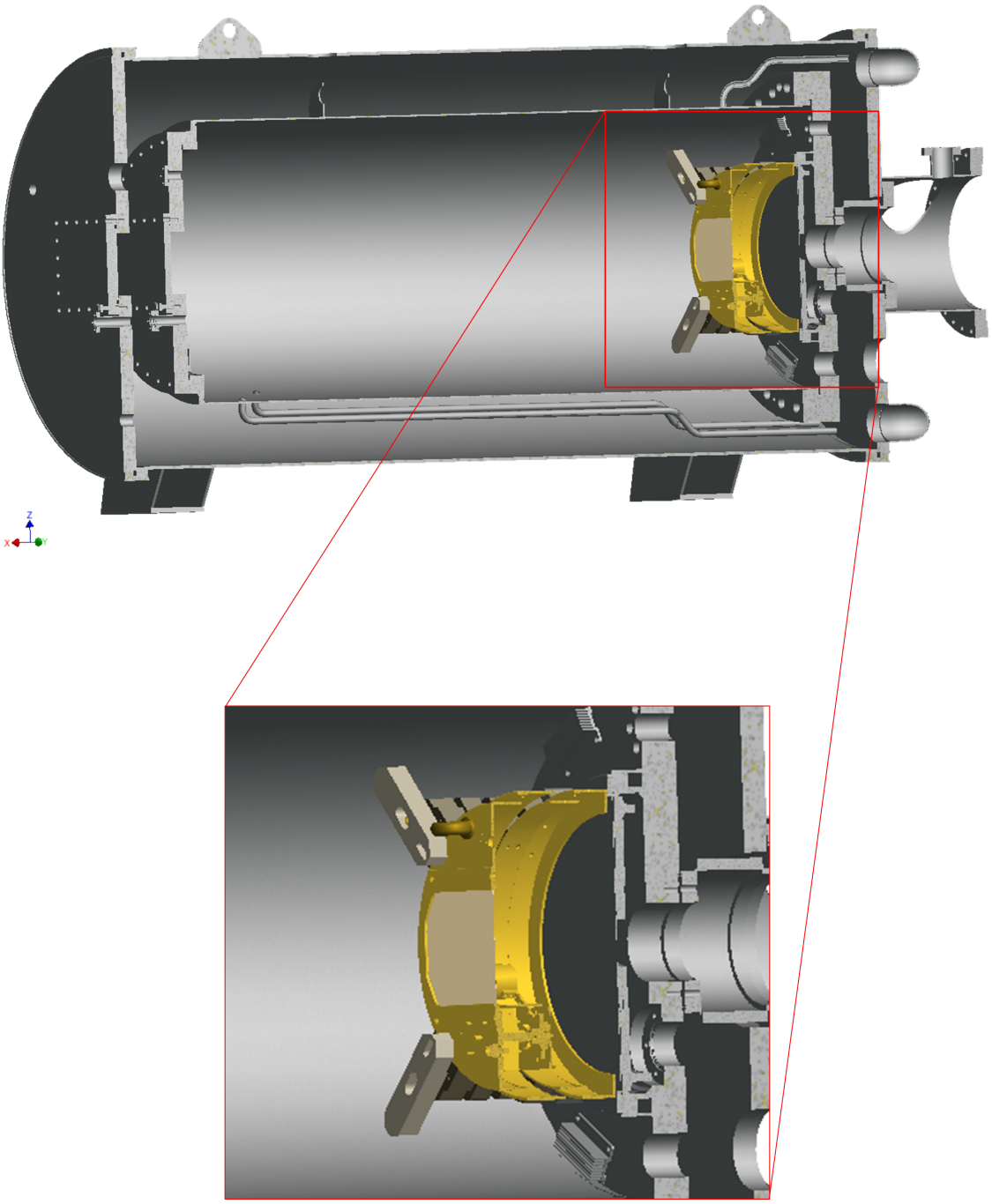

Figure 4.6: Cryogenic Stopping Cell with modified DC body; Optimised for fast extraction times and high fields.
The lower picture shows a zoom onto the 4-ring electrode structure including the source support structure mounted on its movable arm (round cylinder) reaching about 5 cm into the He-gas. The source-carpet distance is ~ 7 cm.

RF-carpet.

Ion sources

The radioactive ion source and the possibility of changing the source's position enables new test cases for the system. The efficiency can be optimised on different positions depending on the starting point if the ions. Optimising for an incoming ions beam as well as position dependent transport tests are possible by the moving arm. The movable arm is driven by a stepper motor of type AML C14X.

4.3 Radio-frequency quadrupole beam line

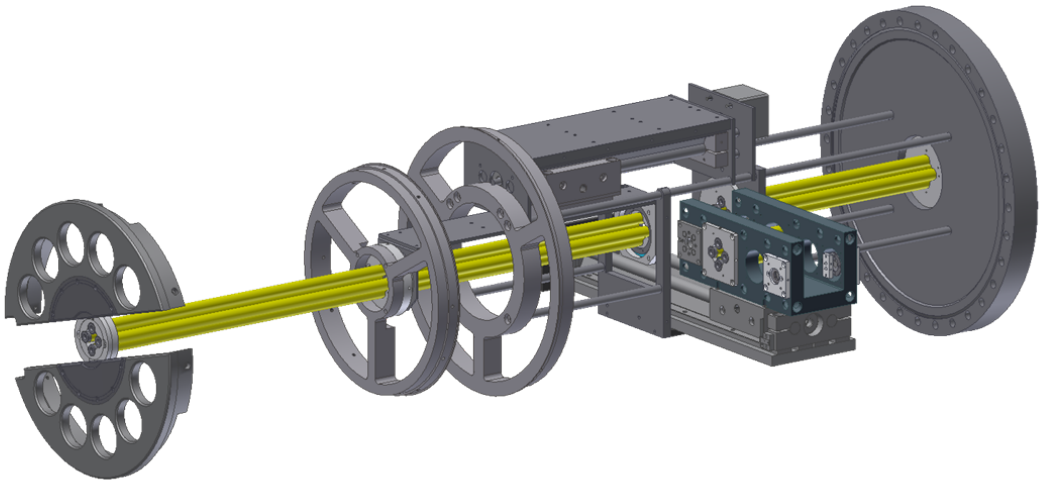

Figure 4.7: Multi-Purpose RFQ Beam Line; Existing of the extraction RFQ to capture the ions extracted by the CSC, which in addition can be run as a mass filter, a movable RFQ segment to clear for a gate valve to decouple the CSC from the MR-TOF-MS and a detector sled to move in detectors for beam monitoring and diagnostics. [Reiter, 2015]

For beam diagnostics and the transport to the MR-TOF-MS the ions are extracted in a multi-purpose radio-frequency quadrupole (RFQ) beam line connecting CSC and MR-TOF-MS, respectively. The RFQ are made of a resistive carbon filled PEEK [Takamine et al., 2005] [Simon, 2008]. They have a diameter of 11 mm and are arranged with a distance of 10 mm. The beam line consists out of four major parts, the RFQ in the extraction region of the CSC, a horizontally movable RFQ that allows to close a gate valve in case of venting either the MR-TOF or the CSC, an RFQ with an implemented detector sled for beam diagnostics and detection and the RFQ beam line connecting the MR-TOF-MS to the CSC finally.

For beam diagnostics either a channeltron or a Si-detector can be moved into the RFQ beam line, see figure 4.7 [Reiter, 2011] [Reiter, 2015]. The sled is built as in-vacuum system, with two remote controlled UHV stepper motors [Lotze, 2014]. A second radioactive source is a triple-α-source of ^{239}Pu, ^{241}Am and ^{244}Cm. It is located next to the RFQ beam line in range of the detector sled (see section 4.3) to calibrate the silicon detectors without polluting them. In addition the extraction RFQ can be run in a mass filter mode reaching a mass resolution of ~ 100 [Miskun, 2014]. With this a rough mass range scan of the extracted ions can be performed and the beam line can be prepared to transport ions further to the MR-TOF-MS efficiently.

4.4 Multiple-reflection time-of-flight mass spectrometer

The MR-TOF-MS is a powerful tool to perform precision and high resolved mass measurements as well as isobar separation [Dickel, 2010] [Dickel et al., 2015a]. In figure 4.8 a schematic view of the MR-TOF-MS can be seen, with detailed information about the setup given. Entering the MR-TOF-MS the ions pass an RFQ based switch yard (SY) [Greiner, 2013] [Ebert, 2016] [Plaß et al., 2015] and make a 90° turn into the injection trap system [Jesch, 2008]. The trap system is built up of three single traps, that first accumulates the ions, second cools them down and third does the potential lift before their injection into the analyser. The ions primarily are cooled with pure He-gas that can be regulated by a gas-inlet system. The time-of-flight analyser is a drift tube with electromagnetic mirrors on both ends to give the possibility of reflecting the ions inside the analyser to extend their path length and increase the spatial resolution between ions with different m/q. To clean up the ion bunch from contamination and unwanted ions a deflector, the so-called mass range selector (MRS) is placed in the middle of the analyser. It deflects ions of unwanted mass regions. After ejection the ions are bend 180° and time-focus shifted on the detector with passing the post-analyser reflector on the bottom of the MR-TOF MS. Depending on the measurement goal (see the different modi following on page 46) two detector system are available. System one is a standard MagneTOF DM167 (SGE Analytical Science Pty Ltd.) to perform time-of-flight measurements. The start signal for TOF detection is given by the ejection of the analyser. For getting the full time information the flight time inside the analyser needs to be considered which is set by the trigger system. Detector system two is a combination of an ion gate - a so-called Bradbury Nielson gate (BNG) [Bradbury and Nielsen, 1936]- and a Silicon detector. The BNG is a thin grid [Yoon et al., 2007] that, if pulsed, deflects unwanted ions and lets the ion of interest pass through. Located directly behind the BNG is a Silicon surface barrier detector for α-spectroscopy.

Three different performing modes can be chosen.

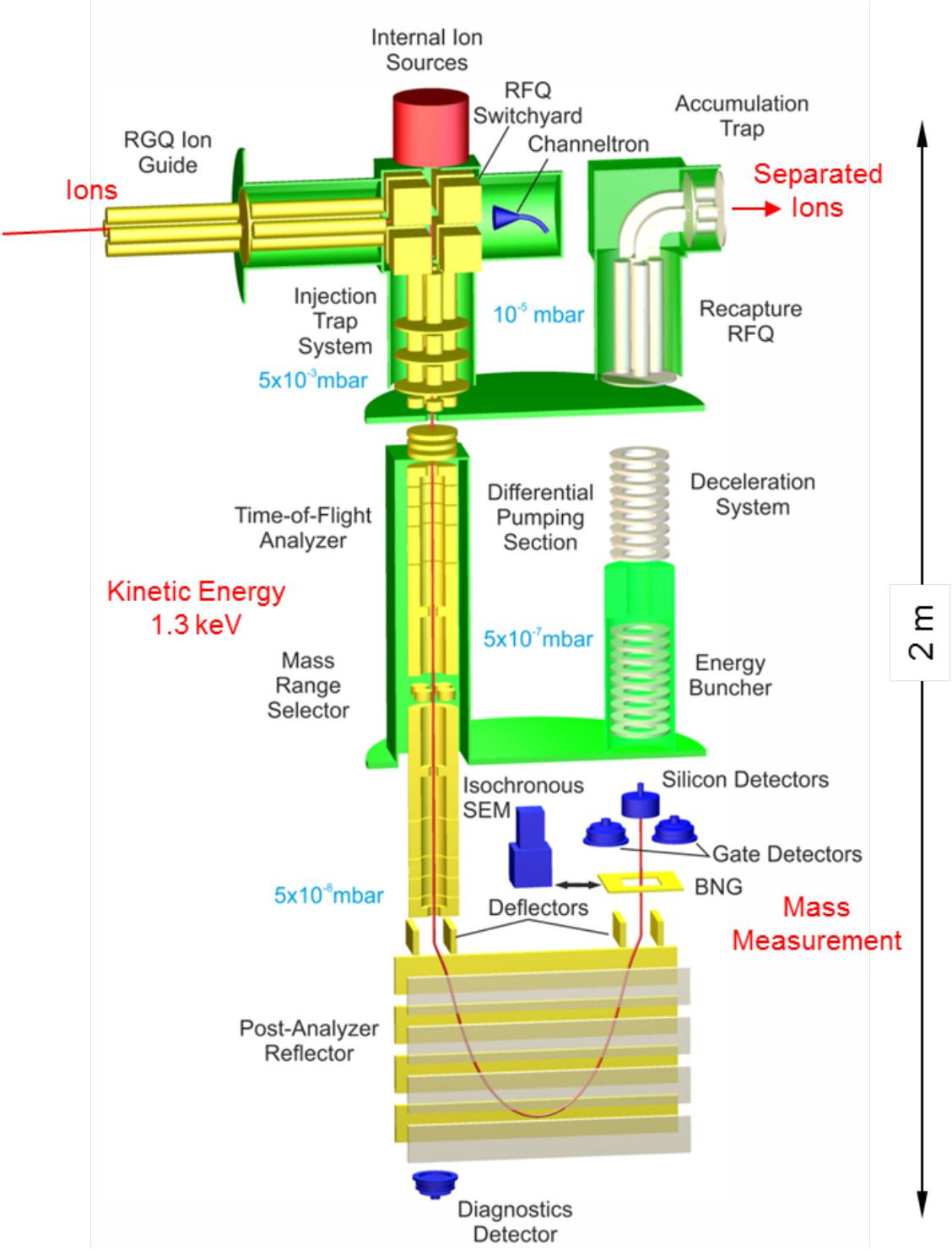

Figure 4.8: Schematic drawing of the multiple-reflection time-of-flight mass spectrometer, with different pumping stages in green and the ion optical parts in yellow. Ions coming from the left, entering the MR-TOF MS via the SY passing the trap system and are injected into the analyser where thy are separated by their time-of-flight. After ejection from the analyser they are deflected in the post-analyser and detected.

The pass through mode let the ions pass the analyser only once, they 'pass through'. This mode is fast ($30-50\mu s$) and gives a broadband view of the incoming mass spectrum with a mass window of $\approx 70\,u$. A MagneTOF detector is used to detect the signals.

High resolution mass measurements can be performed the way that the ions make several turns in the analyser before leaving. Extending their path length leads to a better spatial resolution of ions. The ions are detected with the MagneTOF detector.

The isobar separation mode is based on the previous modes. But instead of detecting the ions with the TOF detector they pass the BNG and hit the Silicon detector. This modus allows isobar/ isomer separation of the incoming beam [Dickel et al., 2015a]. These measurements can be performed with the pass through as well as the high resolution mode.

In agreement of the calculations shown in fig. 3.7 the chosen settings for the MR-TOF-MS fast operation are a cycle time of 2.5 ms, with the ions performing 32 turns inside the analyser. To inject cooled ions in the required time the cooling gas was switched from the light but very less reactive Helium to the heavier but more reactive Nitrogen. The advantage of Nitrogen cooling is the bigger energy transfer per ion-N_2 collisions, compared to He buffer gas cooling with N_2 buffer gas it is faster. A clear disadvantage is the reactivity of N_2.

With this settings the overall time for one cycle is comparable to the extraction time of the stopping cell (gas transport, transport along the RF Carpet), the transport times of the RFQ beam line, the cooling time and the measurement cycle (flight time inside the analyser and from the analyser to the detector)

4.5 Data acquisition

The data acquisition is divided into two main parts. The first one is meant for decay measurements and is the CEAN MC^2 analyser and the second one is meant for mass measurements which is the TDC 9353 from ORTEC.

4.5.1 α-decay spectroscopy

The output of the silicon detector is pre-amplified by either an ORTEC or a CANBERRA pre-amplifier and further given either to a Tennelec TC 44 amplifier (beam time 2014 data) and an ORTEC 926 MCB analogue to digital converter or the table top CAEN hardware that combines amplifier and ADC in one tool.

CAEN MC^2 analyser

The CAEN data acquisition (DAQ) is an ADC especially made for spectroscopy. It it a desktop system with two independent multichannel analyser that combines amplifier and digitiser to one stand alone unit. It records the decay spectrum and if selected a list mode file in addition. The data taken in list modus (corresponding time stamps of the detected events) allow time resolved data analysis which is in particular required for decay spectroscopy and extraction time and profile measurements.

To get reliable time stamps the DAQ's internal clock needs to be triggered from the outside. The correct pulsing signals have been applied by the in MAc implemented trigger software [Pikhtelev, 2014] For extraction time measurements the time reset signal was given by the pulse triggering the ^{223}Ra source, to detect the exact time the ions need to travel from the source itself to the detector. For the decay spectroscopy the reset signal was given by the ejection pulse of the TOF analyser as explained in chapter 3.5 and visualised in figure 3.12.

4.5.2 Mass measurements

For mass measurements two data acquisition software are available. The *Time Digitiser* 9353 from *Advanced Measurement Technology Inc.* as well as the MAc software programmed by Alexander Pikhtilev [Pikhtelev, 2014] and further developed by Julian Bergman [Bergmann, 2015].

Time digitiser 9353

The advantage of the *Time Digitiser* 9353 is the directly implemented list mode operation that safe the exact time of the event with an accuracy of 100 ps. Which makes the software of choice for extraction time measurements of the complete system (CSC to MR-TOF MS). The disadvantage of the software is the clock reset.

MAc software

The MAc software is a non-commercial software developed for mass data acquisition from TDC and ADC signals of MR-TOF MS data. Thus it is able to do a quick real time analysis during a measurement or help to identify possible mass lines with special features like the functions 'peak detection' and 'mark masses'. Next to the standard calibration function it is suited to MR-TOF application in the way that calibration is possible even for different turn numbers of the detected ions inside the analyser. For further data evaluation the function 'time resolved calibration' is implemented. This features allows to correct signal drifts due to e.g. temperature changes of the power supplies.

5 Cryogenic stopping cell for the low-energy branch of the Super-FRS

FAIR (Facility for Anti-proton and Ion Research) and other future radioactive ion beam (RIB) facilities will be built and are built to produce exotic nuclei far off the valley of stability. Getting access to new nuclei that have not been measured before or are rarely known opens up new possibilities in nuclear physics. It also does address new requirements to detectors and data acquisition systems.

5.1 FAIR / Super-FRS

The superconducting Fragment Separator (Super-FRS) at FAIR [Geissel et al., 2003] will consist of two major parts. The first part is the pre-separator that directly follows the production target to perform a first separation of the produced exotic nuclei. The second part is the main separator that does the final selection of the ion of interest. The separation is done with the $B\rho - \Delta E - B\rho$ method, that is successfully working at the fragment separator (FRS) at GSI.

The incoming ions hit the production target with energies up to 1.5 GeV/u. It produces rare isotopes of all elements in unprecedented rates and thus enables the access to more short-lived nuclei. Separated ions species are then guided further to one of three possible branches.

- Ring Branch - to do investigations with ring experiments like ILIMA [Walker et al., 2013]
- High energy branch - to study reactions under complete kinematics (R^3B)
- Low energy branch - to perform precision experiments with laser spectroscopy and penning traps (MATS and LaSpec [Rodriguez et al., 2010])

5.1.1 Super-FRS low-energy branch

An ion beam needs to be almost at rest to perform mass measurements with penning traps. Therefor the separated ions need to be slowed down from relativistic energies to thermal kinetic energies. With a beam spot of $< 200\,\mathrm{cm}^2$ and intensities up to 10^7 ions per second at the end of the separator the ions will be slowed down and thermalised in a He-gas filled cryogenic stopping cell (CSC) and extracted into a low

energy beam line. This hybrid method combines the best properties of the in-flight and ISOL method (see chapter 3.1.2 and 3.1.1) [Scheidenberger et al., 2003].

Challenges and requirements

Slowing down and thermalising incoming ion beams is one major task for the low-energy branch (LEB). Due to the high kinetic energies during and after the production the ions have a large momentum and energy spread which makes it hard to stop ions within a CSC efficiently. A focussing of the ion of interest's energy is needed, therefore the last stage of the main separator can be operated as energy buncher [Scheidenberger et al., 2003]. The ions are passing a combination of higher order magnets for beam aberration corrections. Leaving the Super-FRS the ions have a remaining energy of $< 350\,\mathrm{MeV/u}$. This together with the beam size, energy and ion rate makes beam stopping a challenging task and needs special considerations. Current requirements to the cryogenic stopping cell are [Dickel et al., 2016]

high rate capabilities to avoid space charge effects like losses in extraction efficiencies or plasma creation inside the stopping gas,

high gas density to increase the beam stopping efficiency,

high DC fields to reach fast extraction times and thus minimise space charge limitations.

For efficient stopping at Super-FRS conditions the gas volume has to be sufficient. The current CSC system has a factor of ~ 3 higher density compared to room temperature stopping cells [Wada et al., 2003, Savard et al., 2003, Neumayr et al., 2006, Petrick et al., 2008]. The next generation is designed to handle even higher gas densities up to $\gtrsim 100\mu\ \mathrm{g/cm^3}$ [Dickel et al., 2016]. In experiments the prototype CSC has been commissioned successfully at the FRS at GSI [Purushothaman et al., 2013]. During experiments in 2014 (on-line) and 2015 (off-line) the CSC was pushed to its limitations for the whole system or single parts of it (see chapter 6 for more details). Thus the final conceptual design was developed due to conditions given by the Super-FRS.

5.2 Conceptual design of the cryogenic stopping cell for the super-FRS low energy branch

The design of the stopping cell is specially suited to the above mentioned conditions and shown in figure 5.1. It consists of two main chambers plus an extraction region. The outer chamber is meant to isolate the inner chamber system from room temperature and has a beam window on the left side. The inner chamber system is divided into two connected sub-chambers. One high density region to thermalise the incoming ion beam in cryogenic helium buffer gas and one low density region as differential pumping stage and for fast extraction of thermalised ions.

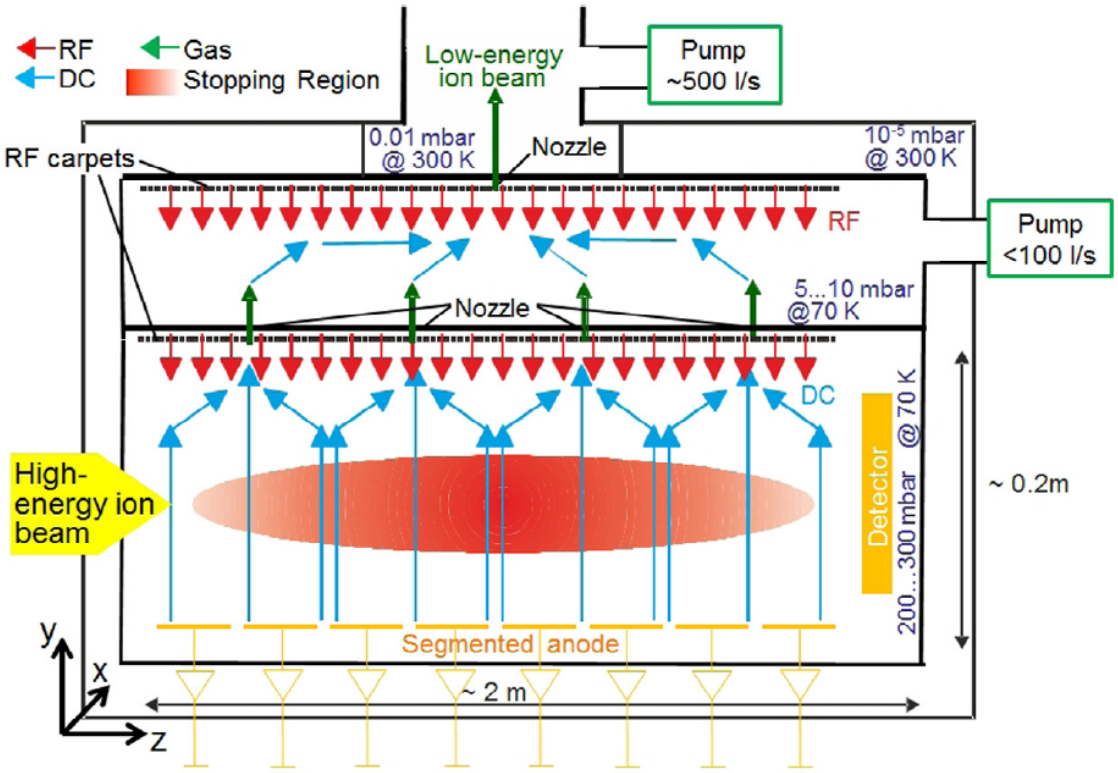

Figure 5.1: Conceptual design of the next generation CSC [Dickel et al., 2016]. The incoming ion beam (left hand side) is stopped in high density He gas ($\sim (200 - 300)$ mbar at ~ 70 K) (red spot) and guided via an electrical DC field (blue) in direction of a dual-layer rectangular RF carpet that extracts the ions applying RF repelling field (red arrows) through a multiple nozzle system into a second low density chamber (green arrows). With gas pressures in the 10 mbar region the ions are now fast extracted with another RF carpet into the RFQ beam line to distribute the ions to the different experiments.

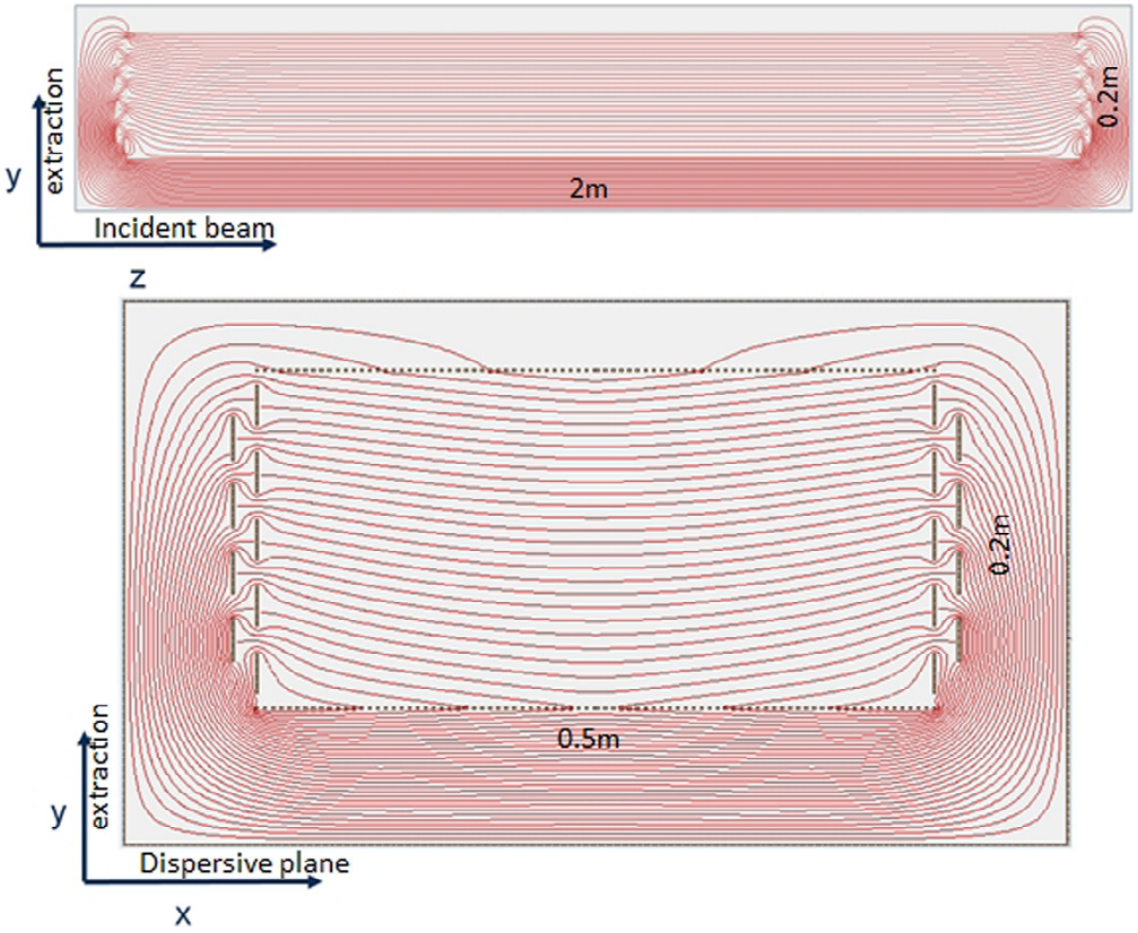

Figure 5.2: Schematic drawing of the stopping region, with electrodes (black) and including the calculated potential field lines (red) [Dickel et al., 2016].

High density region

The high density region of the cold chamber, which is the bottom chamber in figure 5.1, is 2 m in length and $\approx$ 25 cm in height. The ion beam enters from the left (yellow arrow) and is stopped inside the helium gas with a pressure of $\sim 200 - 300$ mbar at $\sim$ 70 K. The thermalised ions are transported via applied DC fields vertically to an radio-frequency carpet system where they are extracted. The RF carpet is a dual-layer PCB-system consisting of a rectangular electrode structure with a size of ≥ 6 electrodes per mm. On the bottom of the chamber a segmented anode will be placed. It is meant to measure the ionisation current and to optimise the DC fields. The ionisation current is space-resolved. Due to perpendicular extraction there is an empty area at the end of the stopping region for detectors. This detector can be used to perform beam diagnostics to identify and to count long range ions, optimising the beam position, focussing and thus allowing an efficient stopping.

Low density region

The high gas densities required for efficient beam stopping require again differential pumping following the stopping region, since the RFQ beam line cannot handle pressures ≥ 1 mbar. Therefore the low density / extraction region was designed to avoid limitations in stopping gas density by too high gas pressures in the RFQ beam line. It is the medium pressure region which means gas pressures are in the range of ≈ 10 mbar of helium. Extracted from the stopping region (the first extraction stage) the ions are transported again via DC fields to a second RF carpet that transports the ions to a single nozzle that extracts the ions as a low energy beam into an RFQ beam line that guides the ions further to the high precision experiments MATS and LaSpec [Rodriguez et al., 2010]. The ions' velocity along the RF carpet is faster than it is in the high density region due to a different operation mode of the RF carpet that guides the ions with the RF wave velocity to the second stage extraction nozzle.

5.3 Expected performance

The above given design parameters and the including simulations [Heiße, 2015] are expected to fulfil the requirements for the Super-FRS. Vertical beam extraction through a multiple nozzle system allows fast extraction times due to short distances between the stopping positions and the nozzles and high extraction fields. The given structure and size of the RF carpet together with the focusing field of the DC electrodes towards carpet result in a super positioned field to focus the ions onto one of the extraction nozzles on every spot inside the stopping region. The corresponding field is shown in figure 5.2 with a view on the extraction-beam axis-plane (top) and extraction-dispersive-plane (bottom).

5.3.1 Simulations

The simulations are made for the produced He_3^+ - e^- pairs because of the space charge effects caused by the produced charge from the ion beam that is stopped in and passing through the CSC, respectively. One impinging ion creates about $10^6 - 10^7$ He ion-electron pairs. Based on the increased DC fields higher rates and therefore higher He_3^+ - e^- production is possible since the extraction or expansion of ionised He gas is deported as fast as the stopped ions. The simulation start at an ionisation rate of 10^{13} He_3^+ per second and ends at 10^{16} He_3^+ ions per second which is even higher than the maximum allowed rate at the LEB [Dickel et al., 2016]. Even for the highest possible rate the expected efficiency does not drop below 50 % due to increased DC fields by the factor of 5 and a decreased extraction time by a factor of 10.

The simulations of the next generation CSC are Monte-Carlo simulations done with the program SIMION [Dahl, 2000]. With respect to space charge effects (see also chapter 2.2.1) and the applied electromagnetic fields the ion transport and diffusion

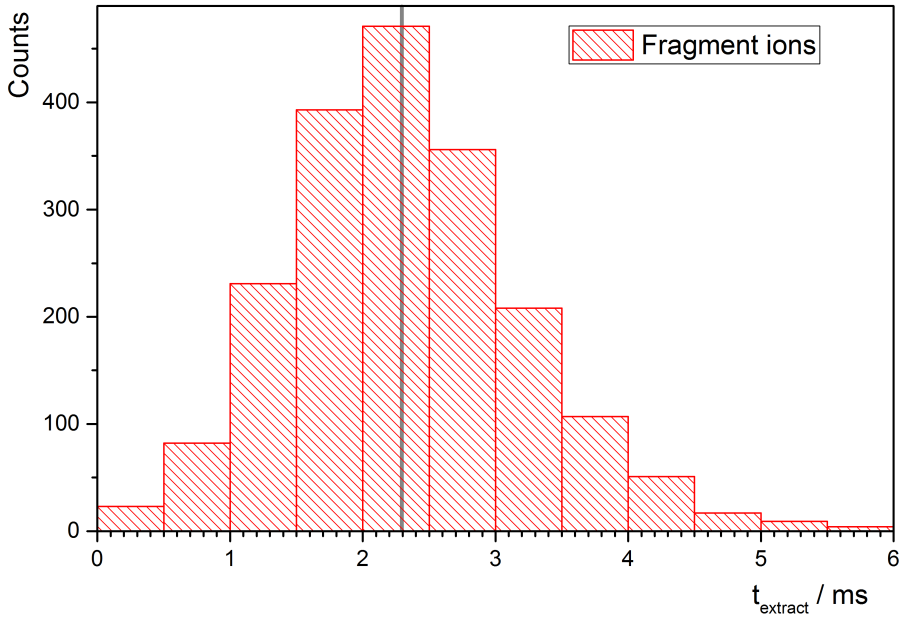

Figure 5.3: Simulated extraction times for beam fragments thermalised inside the stopping region at ion rates producing $\sim 10^{14} He_3^+$ ion pairs per second and DC fields $\sim 300\,\mathrm{V/cm}$ [Heiße, 2015]

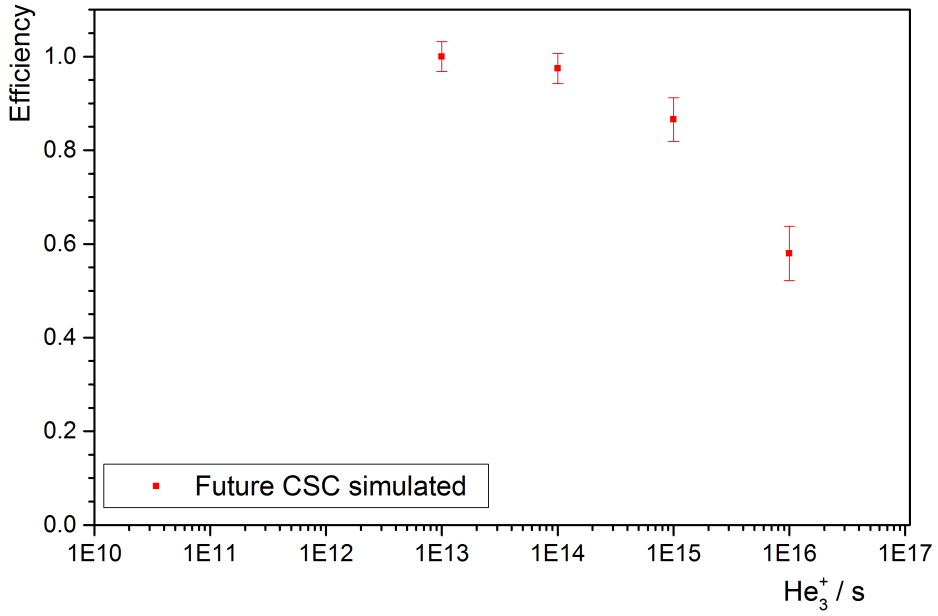

Figure 5.4: Simulated extraction efficiency for the next generation CSC. The different number of charge carriers (He_3^+/e^-), produced by varied incident beam intensities and determined the extraction efficiency modified from [Heiße, 2015].

is calculated via SIMION. The simulation parameters have been tested to validate the results. The three models diffusion, mobility and the Poisson solver were tested and compared with the expected behaviour. The results show a good agreement with theory (for details see [Heiße, 2015]). The result for diffusion is a Gaussian shaped distribution of the ions including the expected standard deviation. The test for ion mobility was done by a check of flight times for ions distributed homogeneously in the stopping gas flying to the RF carpet without any space charge effects. The recorded times conform to the calculated times from mobility theory. At last the Poisson solver was checked with a simple potential array of a capacitor recording the velocity perpendicular and parallel to the electric field of two point like charges. These velocities are compared to the calculated Coulomb deflection of two point like charges and in good agreement. All tests have been made for a variation of parameter sets with the given result in good agreement with the calculations.

The simulated extraction times for beam fragments stopped and extracted for $\sim$ 100 % survival and extraction efficiency and 10^{14} He ion-electron pairs is about 2.3 ms as shown in figure 5.3 done by [Heiße, 2015]. At higher beam intensities (increased number of He ion-electron pairs) the extraction efficiency drops (see figure 5.4) and so does the extraction time due to a shifted mean of the stopped ions that are extracted. Further simulations regarding the rate capabilities of the new design are shown in figure 5.4.

6 Measurements and results

The current system of the FRS Ion Catcher has been commissioned successfully during three experiments. Details about these experiments can be found in [Purushothaman et al., 2013, Dickel et al., 2015a, Reiter, 2015].

6.1 Rate capability

Future experiments require high rate capabilities as already stated in chapter 5. The rate limits of a He gas filled stopping cell are dominated by space charge induced by high ion rates entering the stopping gas. The ionisation rate (number of electron-ion pairs per second per cm^3) in the gas cell is directly proportional to the incoming ion beam intensity. The space charge build up and the consequent decrease in the efficiency (rate capability) of the gas cell is studied in detail during the on-line tests in 2012 and 2014 [Reiter et al., 2016]. The stopping and extraction behaviour of the system at high rates is investigated when space charge is not negligible. The rate capability simulations and measurements are systematic studies to map the limitations of the existing system and to draw conclusions for the next generation stopping cell as shown in chapter 5.

6.1.1 Simulations

The simulations done for the present (prototype) stopping cell have been done in the context of a master thesis [Heiße, 2015]. The operational configuration of the CSC, that is taken for the simulations, is based on the beam time setup of the present CSC as described in chapter 4.2. Due to the limited file size of SIMION the simulation file has a mirror symmetry and therefore two internal sources (bottom and top) in figure 6.1. Furthermore, figure 6.1 shows a vertical cut of the inner chamber where the ring electrodes are given by the horizontal lines (brown) on the bottom and the top of the gas chamber in figure 6.1a. The electrical field is drawn in green and it can be described as homogeneous in the stopping region. The ions enter the CSC (figure 6.2) from the left and are transported to the right where they are transported along the RF carpet towards the nozzle.

At liquid nitrogen temperatures He gas forms cluster molecules of three helium atoms (He_3) and the ionisation does not change the structure such that He_3^+ ions are produced [Helm, 1976]. The thermalised ions will diverge as they are transported towards the RF carpet due to thermal diffusion. The beam size is small compared to the radius of the CSC's stopping region, thus the diffusion does not harm the

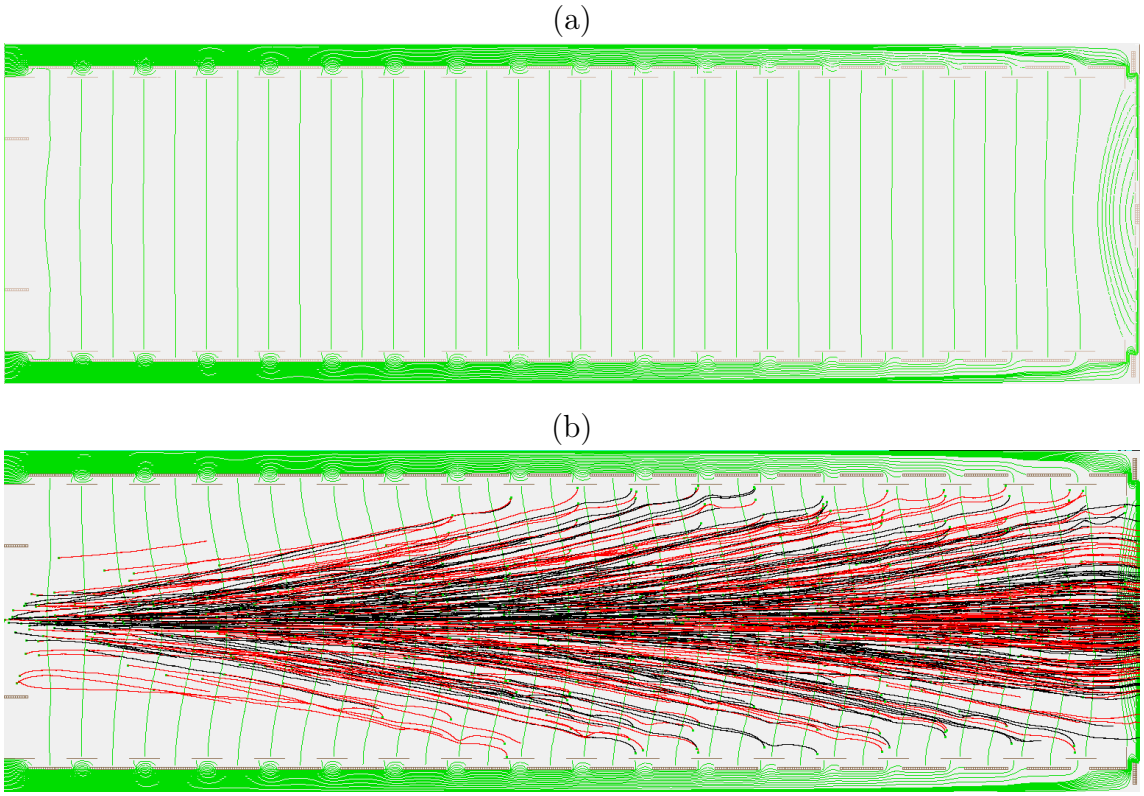

Figure 6.1: Calculated potential lines (red) inside the cryogenic stopping cell. Panel (a): no beam injected. Panel (b): ion beam is stopped inside the CSC. For high ionisation rates the ion beam is defocused due to high space charge creation [Heiße, 2015, Reiter et al., 2016].

efficiency. At high ion beam rates the stopped ions diffuse more due to the huge charge carrier production. Thus the ions can end up neutralised at the DC electrodes of the DC cage as it can be seen in figure 6.1, panel b.

To simulate extraction efficiencies for different ion beam rates first of all it needs to be calculated how many helium-electron pairs are produced for one incoming ion. Because there is not one particular isotope stopped or passing the CSC this needs to be taken into account while calculating the overall amount of helium-electron pairs. Therefor the program LISE^{++} is used [Tarasov and Bazin, 2003] to calculate the deposited energy of the incoming ion beam. It is assumed that each ion entering the CSC releases a clear amount of energy in the helium gas. Since LISE^{++} cannot calculate the single energy deposition, it is estimated by ABRABLA07 calculations [Gaimard and Schmidt, 1991, de Jong et al., 1997]. To finalise the calculations the assumed projectile beam has the following parameters:

- Mean energy loss per He-electron ion pair of 41 eV [Leo, 1994]
- Reduced mobility
  - for heavy ions is assumed to be $\approx 17.5\,\frac{cm^2}{Vs}$

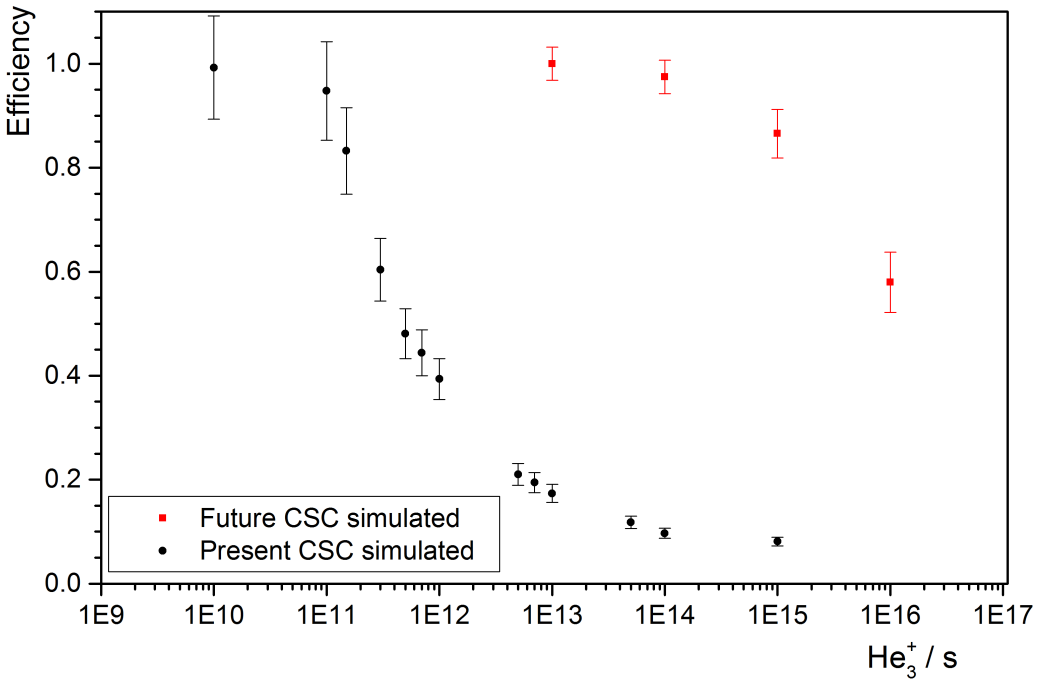

Figure 6.2: Simulated rate capabilities for the present system (black) in comparison with the simulations for the LEB-CSC (red), see also chapter 5 [Dickel et al., 2016].

  - for He molecules is $\approx 18\ \frac{cm^2}{Vs}$
- Helium gas densities
  - for ^{221}Ac 3.3 $\frac{mg}{cm^2}$ (49 mbar at 74 K)
  - for ^{213}Fr 3.7 $\frac{mg}{cm^2}$ (63 mbar at 86 K)
- Beam intensities are given in table 6.1.

The produced amount of He_3^+-e^- pairs inside the buffer gas depends on the energy deposition of each individual fragment entering the buffer gas. For comparison the produced He_3^+-e^- pairs are converted to a rate of the ion of interest as an equivalent to the deposited energy. Via the determination of the overall deposited energy using the He_3^+-e^- pairs a conversion factor was determined for ^{213}Fr ions and ^{221}Ac ions because they are the ions of interest in the evaluated data. The conversion factors for ^{213}Fr beam is $9.5 \cdot 10^6 He_3^+$ and for the ^{221}Ac beam $6.4 \cdot 10^6 He_3^+$ [Heiße, 2015].

With these parameters the simulation results are shown in figure 6.2 where the general trend of gas cell efficiencies for varied beam intensities is shown. The black dots show the results for the present (prototype) stopping cell at the FRS Ion Catcher and the red squares present the results for the next generation CSC as already discussed in chapter 5. The efficiency of the present system is stable until $\approx 10^{11}$ He_3^+ - e^- pairs, where the simulated curve starts dropping immediately, whereas the

	Areal Density $\frac{mg}{cm^2}$	DC Field $\frac{V}{cm}$	Rate $\frac{ions}{s}$	He_3^+ - e^- pairs $\frac{ions}{s}$
^{213}Fr	3.7	9.7	$1.9 \cdot 10^3$	$1.85 \cdot 10^{10}$
			$3.2 \cdot 10^4$	$3.06 \cdot 10^{11}$
			$4.9 \cdot 10^4$	$4.65 \cdot 10^{11}$
			$1.8 \cdot 10^6$	$1.76 \cdot 10^{13}$
^{213}Fr	3.7	20.3	$1.0 \cdot 10^3$	$9.78 \cdot 10^{09}$
			$1.3 \cdot 10^3$	$1.27 \cdot 10^{10}$
			$2.1 \cdot 10^3$	$1.98 \cdot 10^{10}$
			$3.1 \cdot 10^3$	$2.94 \cdot 10^{10}$
			$3.4 \cdot 10^3$	$3.22 \cdot 10^{10}$
			$3.5 \cdot 10^3$	$3.33 \cdot 10^{10}$
			$4.9 \cdot 10^4$	$4.62 \cdot 10^{11}$
			$6.6 \cdot 10^4$	$6.30 \cdot 10^{11}$
			$1.8 \cdot 10^6$	$1.69 \cdot 10^{13}$
^{221}Ac	3.3	12.8	$3.3 \cdot 10^3$	$2.10 \cdot 10^{10}$
			$1.1 \cdot 10^4$	$7.35 \cdot 10^{10}$
			$1.6 \cdot 10^4$	$1.04 \cdot 10^{11}$
			$1.9 \cdot 10^5$	$1.23 \cdot 10^{12}$
^{221}Ac	3.3	22.2	$1.8 \cdot 10^1$	$1.1 \cdot 10^8$
			$1.4 \cdot 10^4$	$8.9 \cdot 10^{10}$
			$2.6 \cdot 10^5$	$1.6 \cdot 10^{12}$

Table 6.1: Measured effective number of ^{213}Fr and ^{221}Ac ions penetrating the gas volume of the stopping cell. The corresponding energy deposition mainly cause ionisation of the He buffer gas and thus create He_3^+ - e^- pairs. For the production of He_3^+ - e^- pair an energy of 41 eV is assumed.

CSC built for the LEB can handle four orders of magnitude more intensity due to its improved extraction geometry.

For experimental data points simulations have been done as well. Each measured point has its corresponding simulated value. The experimental conditions that have been taken for the special simulations as well are written in table 6.1.

6.1.2 On-line experiment

During commissioning experiments of the FRS Ion Catcher at the FRS at GSI uranium projectile fragments were thermalised and extracted. The fragments were produced in-flight by bombarding a ^{7}Be target with an areal density of 1.629 g/cm^2

with a 1000 MeV/u ^{238}U primary beam. For maximum ionisation of the produced fragments the target is followed by a 0.223 g/cm^2 Nb stripper foil. In the course of these experiments rate capability studies as well as extraction time measurements have been performed. In two experiments the projectile fragments of ^{223}Ac and ^{213}Fr have been produced, range focused and energy bunched using the last stage (dispersive stage) of the FRS and were finally thermalised inside the helium buffer gas of the CSC. With the setup and the settings as they are discussed in chapter 4.2 both fragments have been stopped and thermalised for three different ion intensities. In addition two different extraction field strength along the DC structure (see table 6.1) have been applied for each ion beam intensity.

Rate capability studies

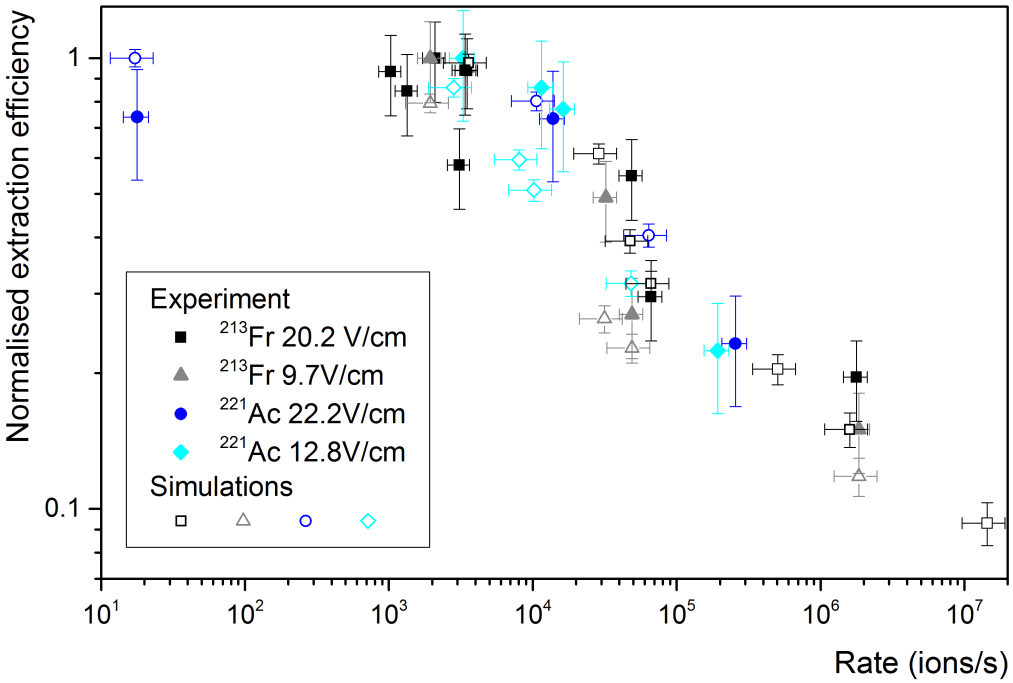

Figure 6.3: Intensity limitation scan for the cryogenic stopping cell done with radio active ion beams of ^{221}Ac (cyan & blue) and ^{213}Fr (black & grey) for high and low extraction fields along the DC cage of the system and their corresponding simulated values (open points) [Reiter et al., 2016].

During the experiment in 2012 rate capability studies have been performed with ^{223}Ac. The ions have been stopped, extracted and detected by α-decay with a silicon detector implemented in the RFQ beam line directly behind the CSC. In the experiment in 2014 the rate capability studies have been performed with ^{213}Fr. This time the ions have been guided further to the MR-TOF-MS and detected with

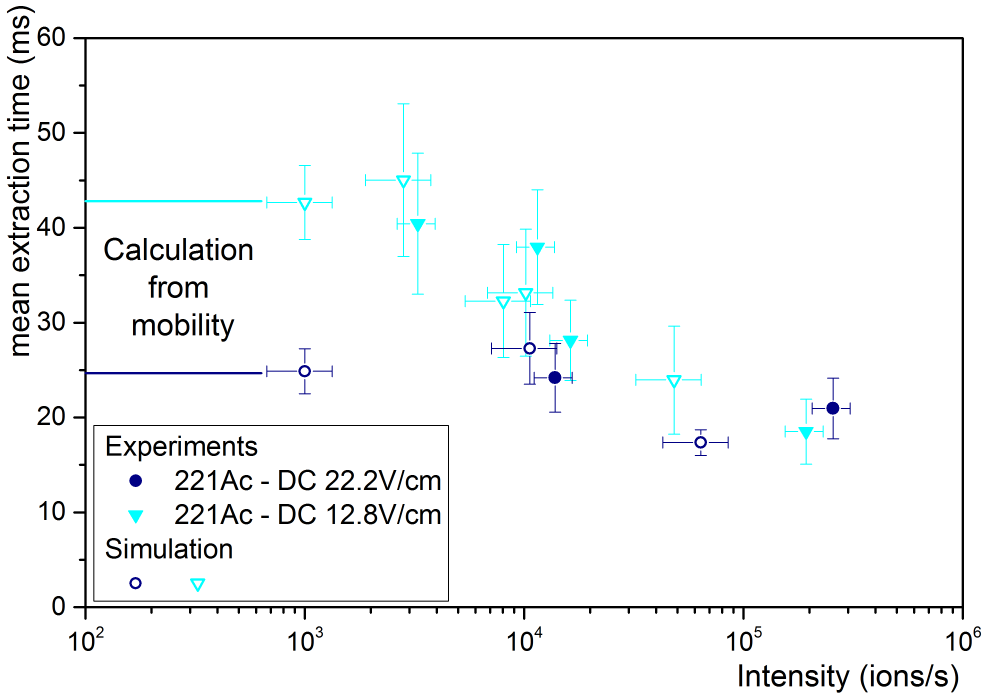

Figure 6.4: Mean extraction time of the ^{221}Ac isotope depending on the the ionisation rate of the He buffer gas that is ionised by the incoming ion beam. The given time is the mean extraction time ions stopped in the middle of the cell need to be transported off the CSC. The measurement was done for two different extraction field strengths of 22.2 V/cm (blue circles) and 12.8 V/cm (cyan triangles) and it is compared with calculations done with mobility theory (open points) [Reiter et al., 2016].

the time-of-flight detector after passing the analyser only once. In figure 6.3 the normalised extraction efficiencies of the CSC are summarised for ^{221}Ac (cyan & blue) and ^{213}Fr (black & grey) ions. The efficiency is given in for ^{221}Ac and ^{213}Fr ions per second, respectively. The measurements have been done for short ion beam bunches with 4 ms length and have been transformed into ions per second. In figure 6.3 the results for both experiment and simulation are shown. Open points in the same colour as the solid points represent the corresponding simulated efficiencies as explained beforehand. Since the ^{221}Ac and the ^{213}Fr data were taken in two independent experiments the settings differ in their parameters which that are in table form on page 62.

For ion rates up to 10^4 ions per second the extraction process is not hindered by the created amount of He_3^+ - e^- pairs as simulations in figure 6.1b illustrate. The normalised efficiency sticks to $\sim$ 100 % and no difference in high and low voltage setup can be seen. For increased intensities the efficiency is decreasing to a measured and simulated minimum of $\sim$ 10 %. In figure 6.3 the normalised extraction efficiency

is plotted against the incoming ion rate per second of ^{213}Fr and ^{221}Ac, respectively. Where the cyan diamonds and grey rectangles belong to low field measurements and the blue circles and black rectangles correspond to the high field operation. The measured results agree with the simulations, that are added as open points in figure 6.3. As it can be seen it is a clear indication for losses along the extraction path throughout the CSC DC body rather than plasma effects or space charge effects at the RF carpet [Reiter et al., 2016]. Due to a charge blow up in the stopping gas the ions are deflected and the beam spot can be widened out until ions come close to or reach the ring electrodes of the DC body and are lost. At high intensities ions will be extracted if they are stopped behind the charge blow up as shown by simulations. The fraction of ions that is stopped closer to the RF carpet can still be extracted. For the overall efficiency it follows a decrease but for extraction times an increase, due to the shifted mean of the extracted ions. Their centre is shifted closer to the exit nozzle, to shorter CSC length and thus these ions are extracted faster while the others are blocked by space charge. This effect is plotted in figure 6.4 for ^{221}Ac and two extraction fields. The extraction time is decrease the same moment the extraction efficiency is dropping blue rectangles (compare it with figure 6.3). The measured data (full points) reproduce the calculated times (open points) well within the error bars. All calculations are done with mobility theory.

6.2 Systematic studies of the RF-carpet

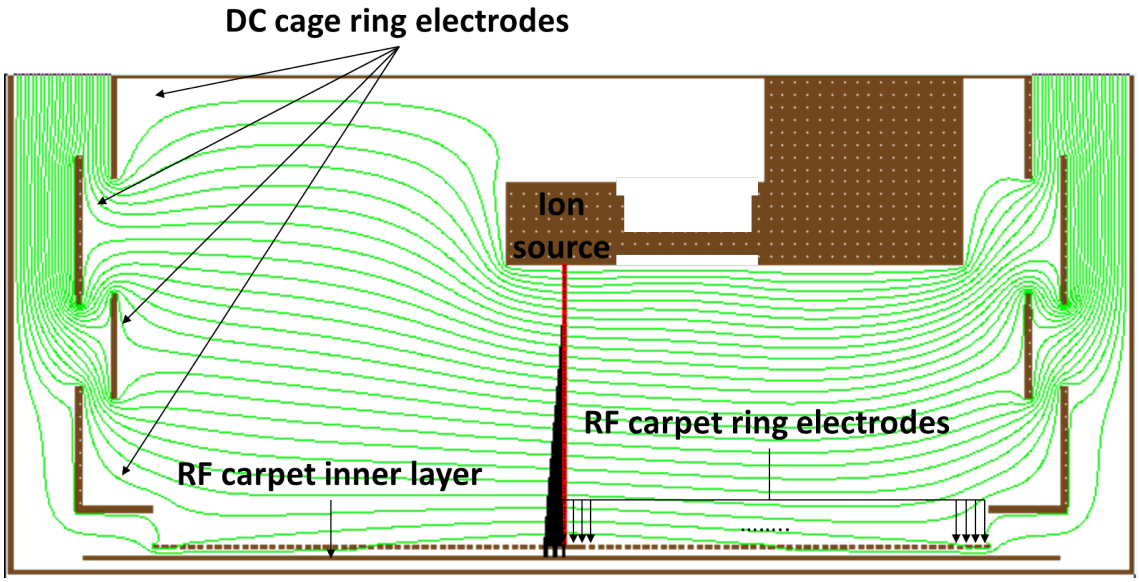

Figure 6.5: Schematic drawing of the short cage setup as described in chapter 4.2.4 with simulated extraction field and ion flight path (red/black) done with SIMION [Manura and Dahl, 2006]. It shows schematically the DC electrodes as there are the DC cage ring electrodes for the extraction DC field, the RF carpet inner layer electrode to apply an addition pushing/pulling field, the RF carpet ring electrodes that handle DC and RF voltage for ion transport and last the ion source itself as an electrode to be able to stop the ion extraction if necessary.

Next to the rate capability studies of the cryogenic stopping cell another question raises and needs to be clarified for the next generation stopping cell. The second limiting factor and the heart of the system – the performance of the RF carpet under high field and density conditions.

As already described in the previous chapter the system was changed a) to extract ions fast and b) to be able to apply high fields on the system to test it for future applications. In this section the systematic studies will be discussed only.

The short cage CSC has been drawn with SIMION [Manura and Dahl, 2006] determine the different fields applied at the measurements. The extracted field is corresponding to the highest field in front of the extraction nozzle. For calculations the exact voltages applied during the experiments have been taken. Since SIMION does have a limited file size and a minimum structure size for electrodes the RF carpet was approximated with 45 electrode rings instead of 500 but with kept relations of electrode – gap dimensions.

To test the system under high field and high pressure conditions it ran at He gas temperatures around 80 K and varied He gas pressures from 25 mbar up to 90 mbar, which corresponds to gas densities up to $< 50\,\mu g/cm^3$. This are basically the same

settings as for the commissioning experiments to keep the two setups comparable. The electrical fields that have been applied are between 13 V/cm and 72 V/cm. For the test the movable ^{223}Ra source (see also 4.2.2) was set to two positions. The first position was on beam axis in a way that the ions did not need to travel along the RF carpet. The second position was off beam axis and implemented an ion pathway to travel along the RF carpet.

The testing conditions have been changed to the on-line setup in the way that the system is now closer to its future operation setup, than it was before (see chapter 4.2 and 4.2.4). That opens up new possibilities for testing particular parts under LEB conditions. For preparation the RF carpet was put at its optimum radio-frequency amplitude which is the resonance frequency (in most cases) to avoid two different amplitudes for the two π-shifted RF phases.

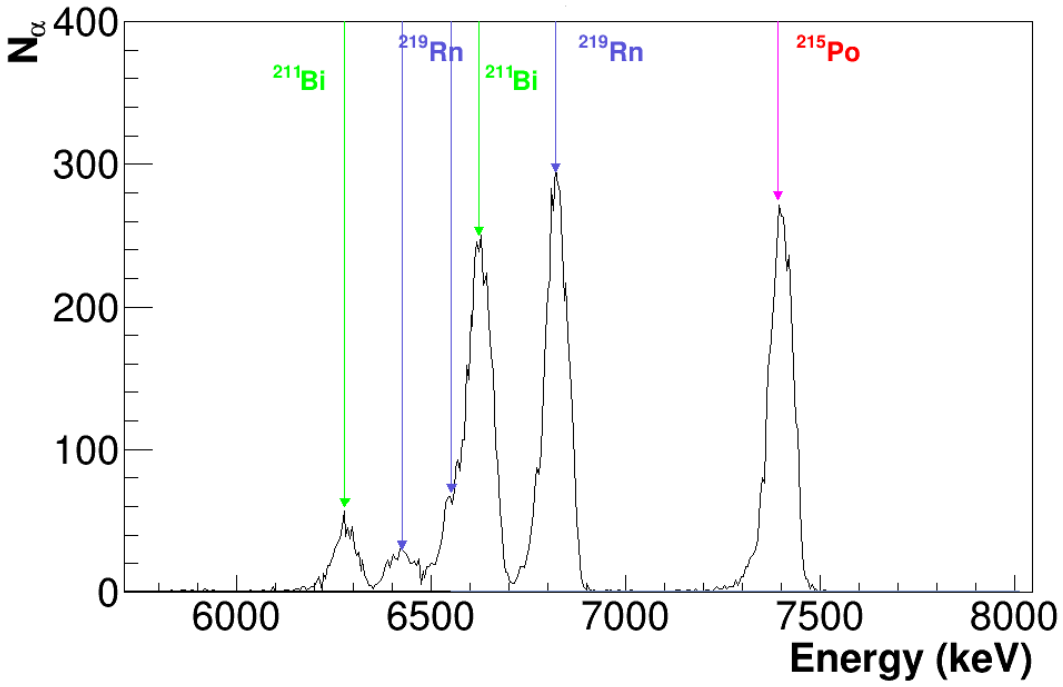

Figure 6.6: α - spectrum of the ^{223}Ra ion source taken with a Silicon detector, with the polonium line on the right, the highest and the very left peak are the two bismuth lines and the three remaining lines correspond to ^{219}Rn.

The α-spectrum of ^{223}Ra, shown in figure 6.6, exemplifies the data acquisition for systematic studies of the RF carpet. To count the number of entries only the corresponding channels of the decay line of interest have been taken for determination of extraction efficiency and the count rates, respectively. The decay energies of the second ^{219}Rn channel and the first ^{211}Bi channel are strongly overlapping and cannot be resolved due to a limited resolving power of $30 - 50$ keV of the Si-detector and its data acquisition that have been used. Thus only the prominent α-energy line representing 79.4 % of the decays is taken as well as the ^{215}Po decay channel on the very right of the spectrum.

To do systematic investigations the following settings have been varied:

- helium buffer gas density
- field strength along the DC body
- field strength along the RF carpet
- the source position that the ions have been transported from 7 cm of beam axis or directly on beam axis
- for off axis measurements the inner layer voltage was varied between 0 V offset and 60 V offset

6.2.1 Transport efficiency

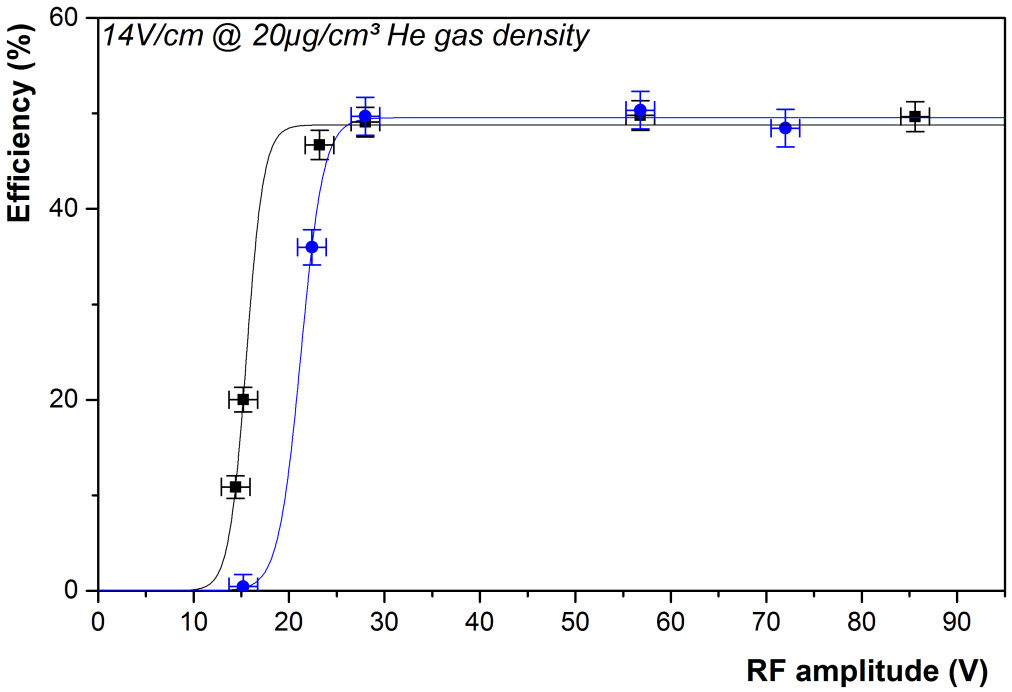

Figure 6.7: Scan of the radio-frequency amplitude on the carpet to optimise the ion transport efficiency. Two independent measurements for the same parameters are plotted.

To determine the transport efficiency of the RF carpet the RF amplitude is scanned and the number of extracted ions is detected. An α-spectrum is giving the number of events for the first decay channel of the ^{219}Rn isotope. This number is then converted into an efficiency using the well know activity of the off-line source. In figure 6.7 two exemplary RF scans are shown. The efficiency is fitted with a Boltzmann

distribution given by equation (6.1).

$$f_{\text{Boltzmann}}(x) = B + \frac{A_{\text{ampl}} - B}{1 + exp\left(\frac{x - x_0}{dx}\right)} \qquad \text{with } B = 0 \tag{6.1}$$

Both scans have been taken under similar condition to get an estimation on the reliability of the data points and the RF carpet. As shown, the efficiency on the plateau is stable and can be reproduced well. For the needed RF amplitude an error of 15 % was determined and is applied to all measurements in the following analysis sections of chapter 6.

The RF carpet is the heart of the system it needs to be clarified that it is working properly and the results are reliable. The measurements have been compared with the results discussed in [Reiter, 2015] to draw conclusions out of the results with the fast extraction setup. In figure 6.8 the dependency of the RF amplitude on the

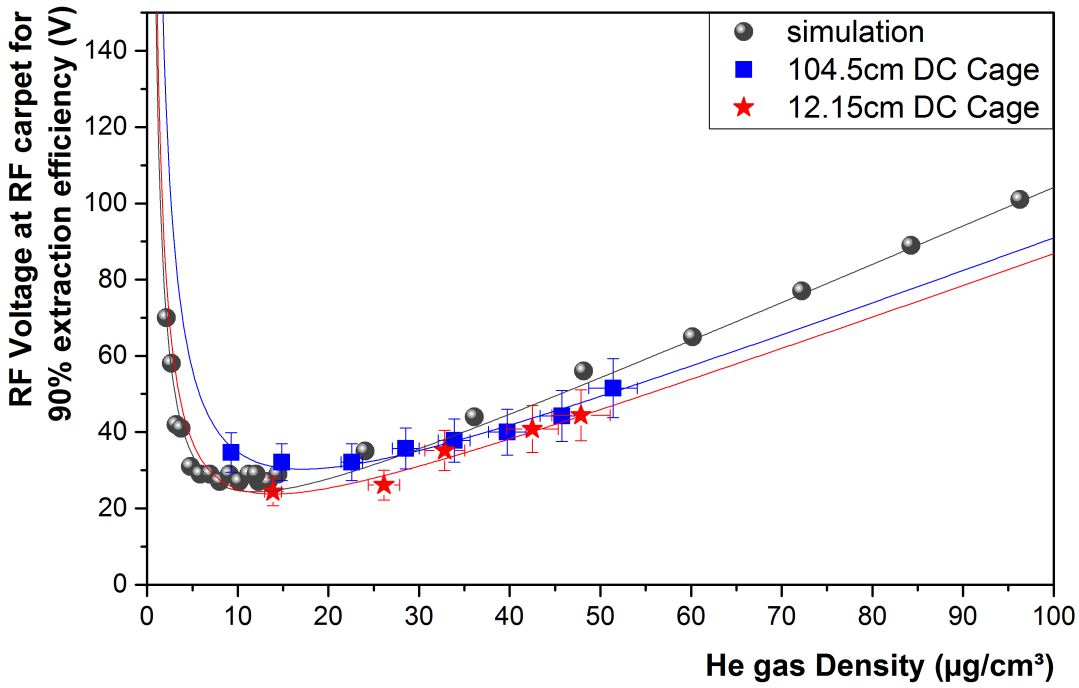

Figure 6.8: Systematic RF carpet studies of the short cage setup (12 cm)compared with the long cage setup (100 cm) as done in [Reiter, 2015]; The 90 % RF amplitude for the maximum extraction efficiency of the RF carpet is plotted in dependency of the areal density. Blue squares represent the long cage measurements and the red stars the short cage measurements. In addition the simulated behaviour of the RF amplitude is given.

areal gas density is shown. The amplitude for 90 % extraction efficiency of ^{219}Rn was determined by fitting an RF scan with a Boltzmann distribution of equation

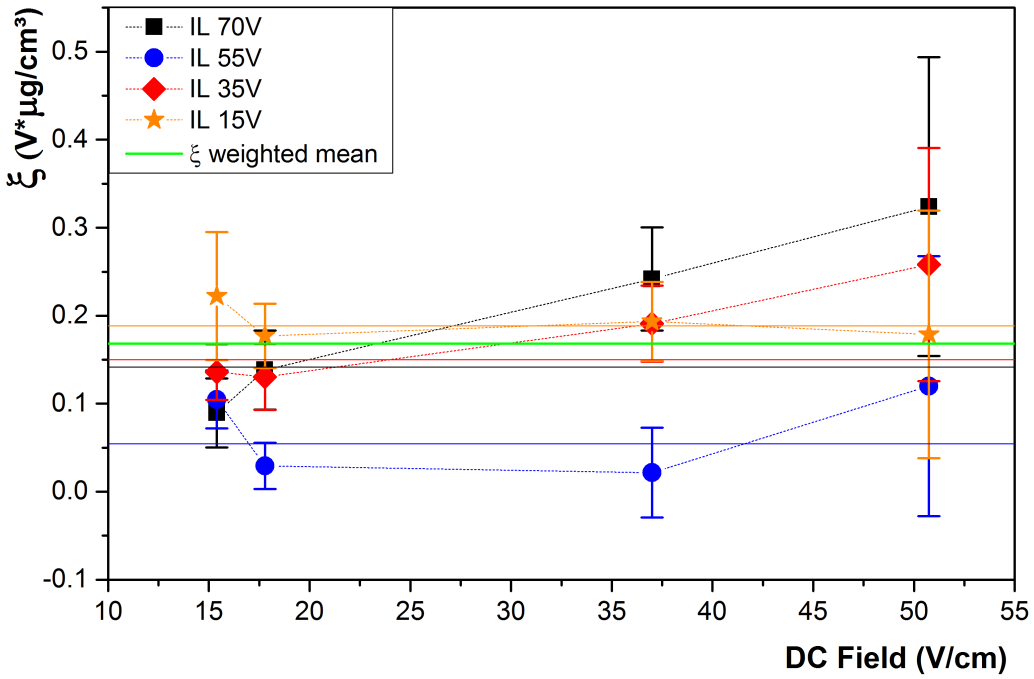

Figure 6.9: Fit parameter ξ of equation (6.2) plotted versus the DC voltage applied on the ring structure of the DC body of the CSC (see figure 6.5). This parameter was determined for four different RF carpet inner layer voltages (IL) 15 V, 35 V, 55 V and 70 V. For further calculations a weighted mean of ξ was determined as $\xi = (0.16819 \pm 0.00755)\,\mathrm{V}\cdot\mu\mathrm{g/cm^3}$.

(6.1) (see figure 6.7).

Since the standard Boltzmann fit does give the 50 % value only, the voltage for 90 % efficiency needs to be calculated from the given fit. Long cage (bluish) and short cage (reddish) measurements are compared, where the long cage data points are taken from [Reiter, 2015]. The plot shows a good agreement of the two systems, thus we can assume the changes in the DC structure of the DC cage do not change the behaviour of the system and especially the RF carpet.

Therefore the RF scan studies give information about the performance and we can carry on with the established tests for the cryogenic stopping cell.

Detailed investigations of the transport efficiency have been done for the setup with the source positioned off axis to include the ion transport along the RF carpet. This has been done for varied inner layer voltages of the RF carpet of $(15, 35, 55, 70)$ V DC and for four different DC fields along the DC cage ($(46.7, 32.3, 17.8, 13.7)$ V/cm). The presented results are based on results of RF scans for 50 % extraction efficiency on the contrary to the 90 % transmission of the data points in figure 6.8 and [Reiter, 2015]. The gained curve of the RF scans is fitted with a broken rational function to

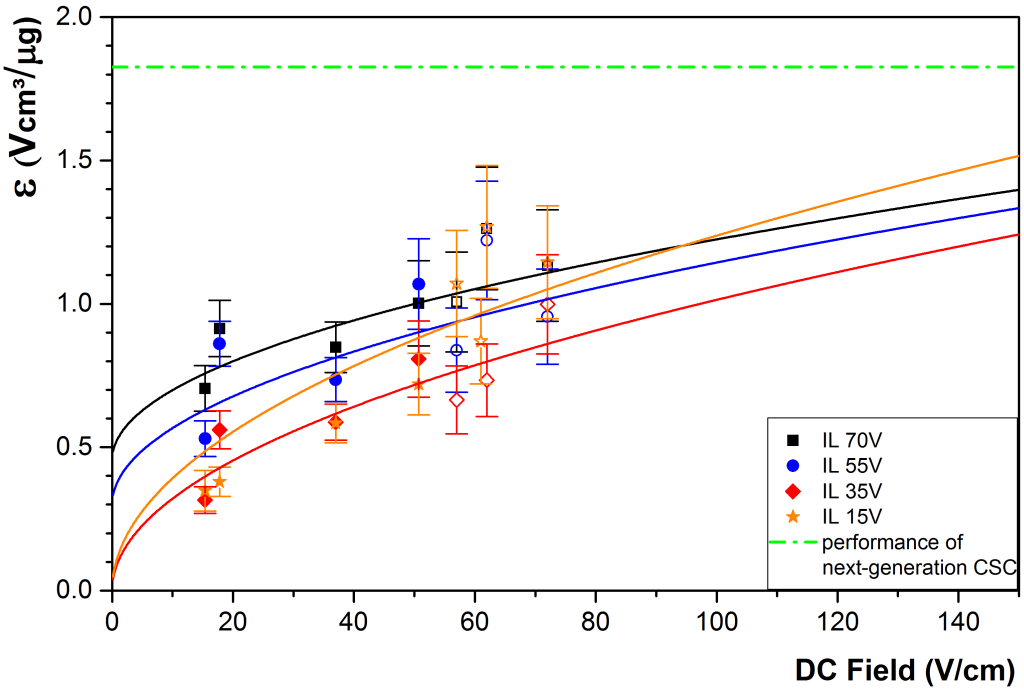

Figure 6.10: Dependency of the RF-amplitude on the areal gas densities as well as the applied DC fields for ion transportation/extraction. In detail it is the linear dependency of the transmission plot (parameter ϵ) as exemplary shown in figure 6.8 on the applied DC fields. Full data points are resulting from the complete measurement series whereas the open points are calculated from on particular RF scan.

describe the RF amplitude A_{RF}:

$$A_{\mathrm{RF}}(\rho) = \frac{\xi}{\rho} + \epsilon\rho \tag{6.2}$$

For densities $< 10\,\mu\mathrm{g/cm^3}$ the helium gas density is very low, thus the ions are fast and need higher RF fields to be repelled from the carpet electrodes. Figure 6.9 shows the trend for parameter ξ from equation (6.2). A global value for ξ has been determined by fitting a constant to each set of data and built a weighted mean (green line in figure 6.9). For densities $> 10\,\mu\mathrm{g/cm^3}$ the linear dependency (parameter ϵ) is the dominating trend of the needed RF amplitude, thus it is reasonable to focus on the evolution of parameter ϵ further. It is then plotted versus the applied DC fields and again fitted with

$$\epsilon = \zeta \cdot E_{\mathrm{DC}}^{0.5} + \mathrm{o}. \tag{6.3}$$

From section 2.3.2 and equation (2.35) follows a quadratic connection between the

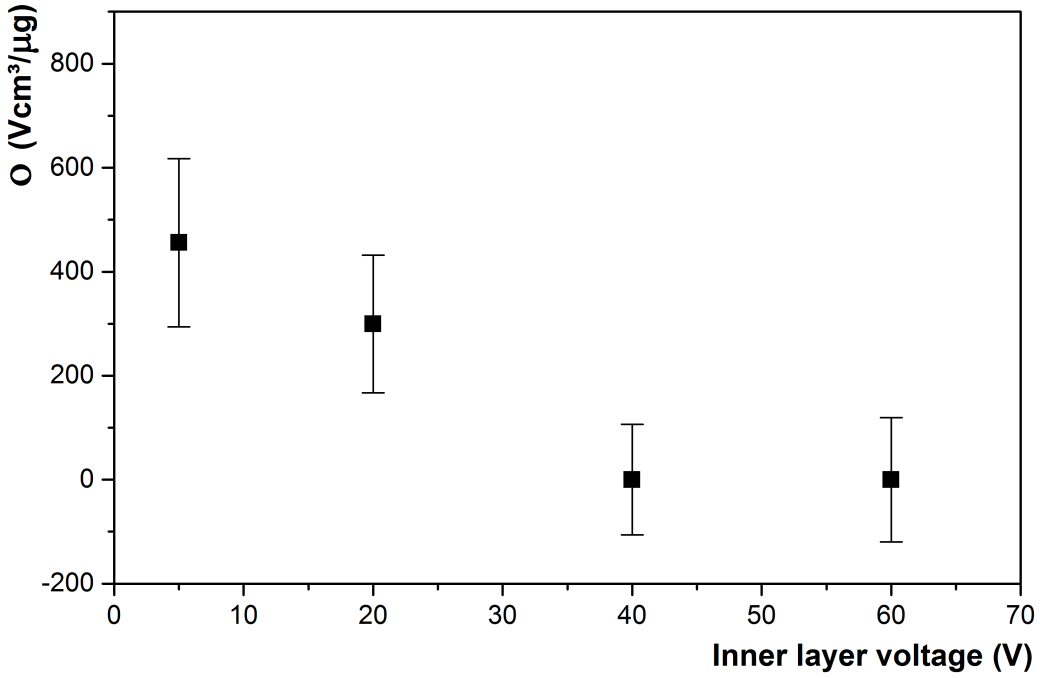

Figure 6.11: The influence of the inner layer voltage on the RF voltage of the RF carpet. Inner layer voltage vs offset of the fit of ϵ.

resulting electrical field and the necessary RF voltage of the carpet. Figure 6.10 shows the slope of the linear contribution of the RF amplitude for different DC fields applied to the DC cage. The data is plotted and fitted for four inner layer voltages using equation (6.3). The behaviour at higher gas densities and DC fields can be extracted. Full data points represent complete RF scan series whereas open data points represent particular RF scans, only and the ϵ is calculated with the given formula (6.2) and the fixed ξ as given from plot 6.9. Within the error bars parameter ζ gives the same value for each inner layer setting. However the offset o seems to have a characteristic behaviour for different inner layer voltages.

The conclusion for the next generation CSC is added in the green dotted line. It shows an operation value calculated from the maximum parameters of the next CSC. Since the structure size of the current RF carpet is bigger than the one of the future system, the value has been converted to fit to the current RF carpet. It can be extracted that the RF carpet is not limited by high densities and DC fields in its functioning.

Inner layer investigation

As already plotted in figure 6.9 and 6.10 there is a dependence on the pushing voltage of the inner layer electrode especially for low densities and small fields. In figure

6.10 the single fits of each data set of one inner layer voltage tend to get closer for high fields and corresponding to that high densities as well. Regarding the low field case only figure 6.11 shows the offset of equation (6.3) in dependence of the inner layer voltage. It describes the necessity of this voltage for efficient ion extraction at low RF voltages for low extraction fields which is described by the drop down of the offset o for high inner layer voltages.

Transport at high He gas density and high DC fields

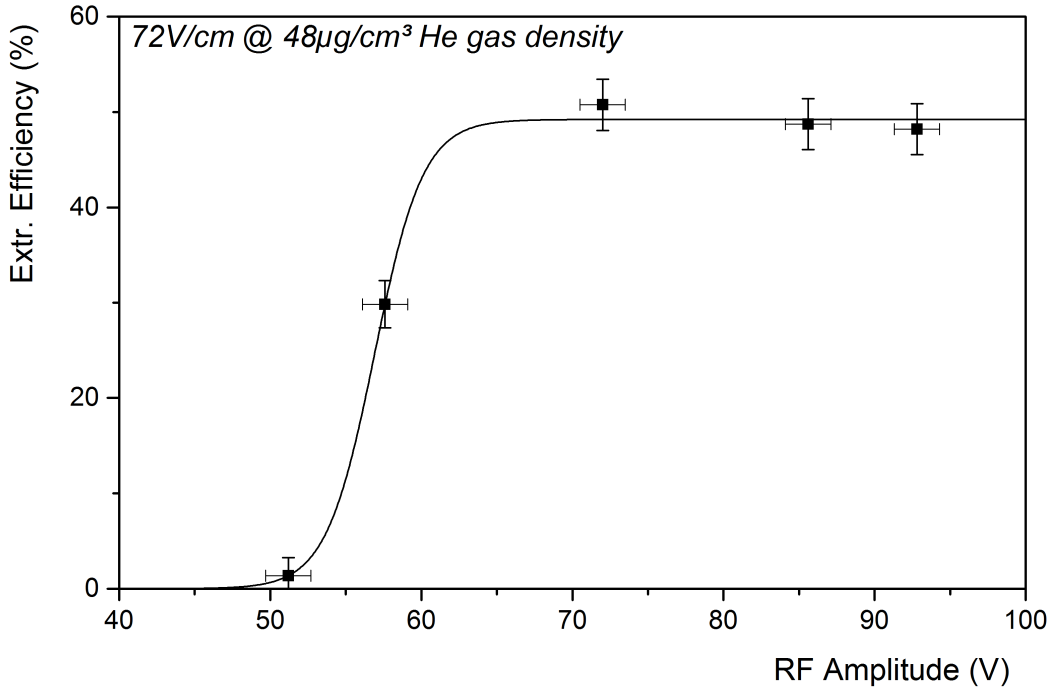

Figure 6.12: Measured extraction efficiency for different RF amplitudes applied to the carpet. A stable operation condition was even achieved at He gas densities of $48\,\mu g/cm^3$ and extraction fields of $72\,V/cm$ and yields 50 % extraction efficiency. The data points are fitted with a Boltzmann equation (6.1).

To investigate the limitations of the components the RF carpet was tested under extreme conditions of $72\,V/cm$ at helium gas densities of $48\,\mu g/cm^3$. The proper function of the RF carpet was checked and an RF scan was done as figure 6.12 states. The rising slope does imply a reliable function even at such high voltages and the standard extraction efficiency of 50 % of ^{219}Rn was achieved. An application of higher voltages at this densities was not possible due to discharge limitation of the setup.

6.3 Extraction time measurements of the short-cage setup

As already explained in chapter 5 and 6.1 to handle high rates of ion beam the extraction time of the stopped ions needs to be fast. With the short cage setup of the present stopping cell (see figure 4.2.4) the geometry of the system approaches the next generation CSC at least in extraction distances and probable fields. Therefor extraction times have been measured. Due to the electrical connection through a floated 19 pin feedthrough the maximum voltage difference has been 150V to avoid discharges between source and DC cage ring 1. This voltage difference was too low to be able to block the extraction of ions completely. Only for ^{215}Po it has been possible to retard ions long enough that they have been decayed before their extraction and have not been detected as polonium.

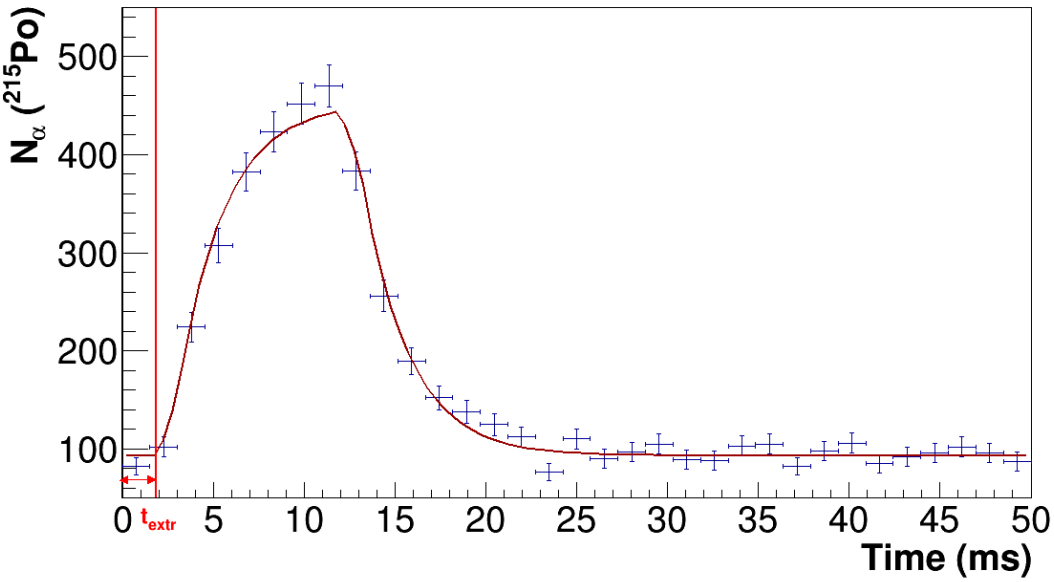

Figure 6.13: α-decay measurement of ^{215}Po ions extracted from the CSC during a time interval of 50 ms. The red line represents a fit to deduce the extraction time (t_{extr}), which is calculated from equation (3.72).

To measure extraction times the data acquisition and the off-line source run in pulsed mode. The trigger scheme has been shown in chapter 3.5 figure 3.12. The source is connected to a pulser can be pulsed 150 V down for a short time to stop extraction and the DC cage ring 1 voltage setting. Extraction times have been measured using the silicon detector located in the RFQ beam line that connects CSC and MR-TOF-MS. The extraction efficiency of a DC beam (none pulsed source) is $\sim$ 50 %, the efficiency with a pulsed source depends on the duty cycle of the pulsing scheme, thus can vary for different measurements. The extraction time detected by the Si-detector in the RFQ beam line is defined by the start of the rising slope fitted with

equation (3.72). A typical extraction form is shown in figure 6.13. Compared to

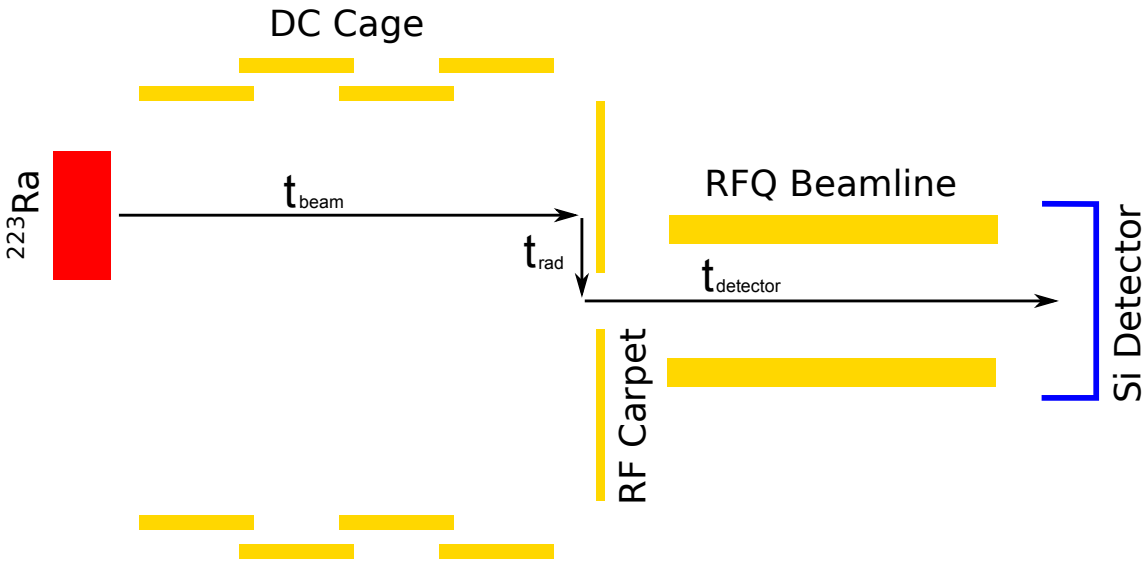

Figure 6.14: Ion path (black arrows) inside the CSC and to the detector placed at the RFQ beam line. The ions are emitted from the source (red) and travel on straight trajectories upto the RF carpet and then move radial until they are extracted until the nozzle.

given extraction times of the long cage setup, where the mean of the stopped beam is taken as it is done in [Purushothaman et al., 2013], this time the extraction time is given from the first detected ion which is related to the travel time through the complete setup (source-detector) an example function is plotted in figure 3.11 top panel. The extraction time of the CSC is not depending on the extraction field only, but on the He gas densities of the stopping region as well. With DC voltages of 200 V at the source and the corresponding field of 19 V/cm the extraction time is 2.5 ms at 11 μg/cm^3 gas density.

The extraction time was measured for two positions of the ^{223}Ra source to compare differences in transport times and behaviour. Source position one (see section 6.2) ejects the ions directly on beam axis into the gas that there is almost no transport along the RF carpet necessary to extract ions. For the second position the ions start from an off axis position and thus have to travel along the RF carpet to finally reach the extraction nozzle. For calculations the ion pathway is assumed to geometrically ways. It adds up the three different times needed to travel along the single pathways source–carpet, carpet–nozzle, nozzle–detector.

$$t_{\text{calculated}} = t_{\text{beam}} + t_{\text{radial}} + t_{\text{detector}} \tag{6.4}$$

$$\text{with} \qquad t_{\text{radial}} = r \cdot \kappa_{0,\rho,V} \tag{6.5}$$

$$t_{\text{calculated}} = t_{\text{beam}} + r \cdot \kappa_{0,\rho,V} + t_{\text{detector}} \tag{6.6}$$

where t_{beam} is the path in beam direction, t_{radial} is the time for travelling along the RF carpet, $t_{detector}$ is the time from exiting the CSC until the ions reach the detector.

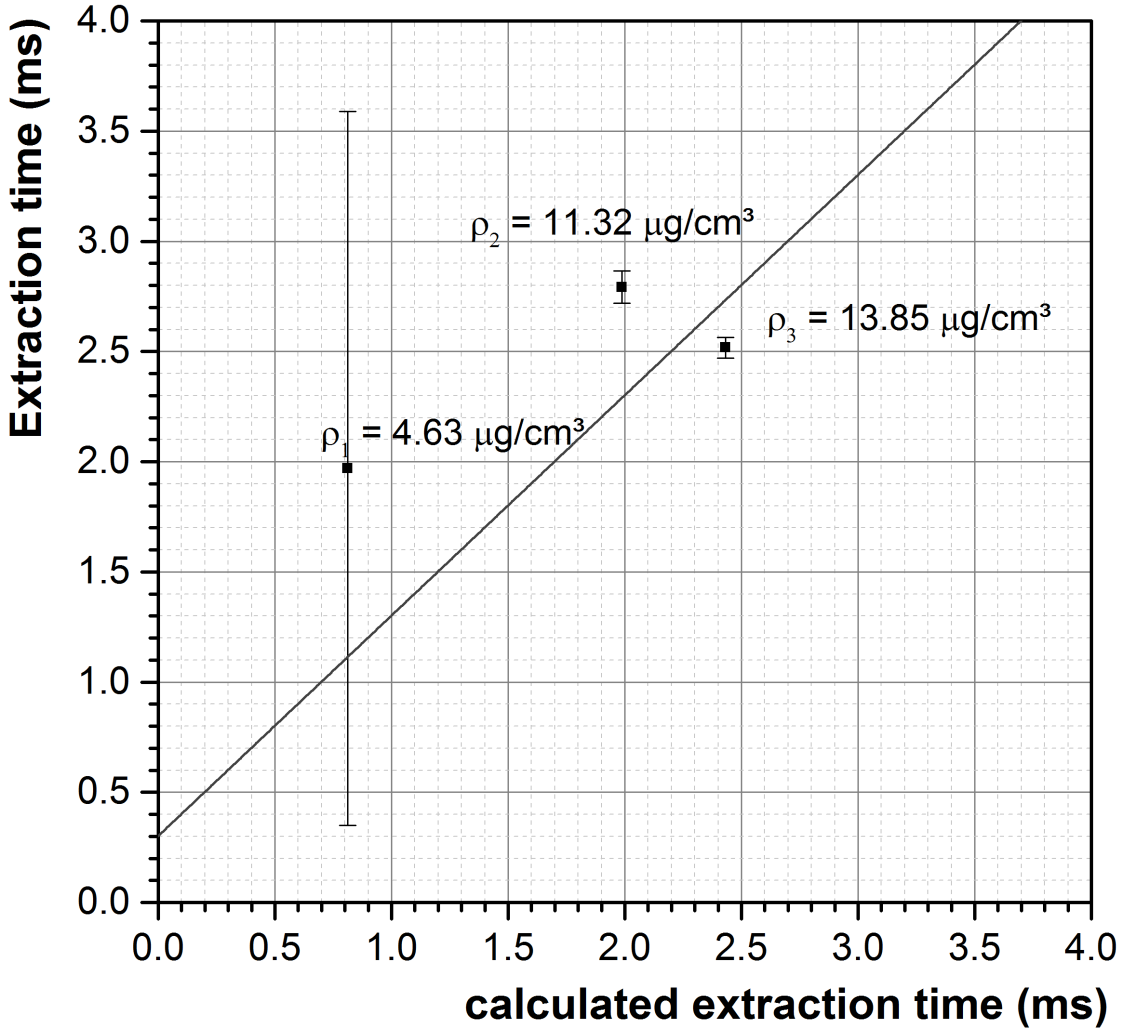

Figure 6.15: Calculated and measured extraction times of ^{215}Po ions for 19 V/cm and three different He gas densities. The calculated extraction time, based on mobility theory, is plotted versus the measured extraction time. The offset of the depicted linear fit represents the transport time from the nozzle to the detector.

$\kappa_{0,\rho,V}$ is a mobility factor consisting of the ion mobility κ_0, the he gas density ρ and the DC field along the RF carpet V.

From ion mobility the ions drift through the gas only by the applied DC field and the drift time t_d through the gas is defined as

$$t_d = l \cdot \rho \cdot \frac{1}{E_\mathrm{DC}} \cdot \frac{1}{m(\mathrm{He}) \cdot u} \cdot \frac{T_0}{T} \cdot \frac{p}{p_0} \cdot \frac{k_\mathrm{B}}{\kappa} \tag{6.7}$$

In figure 6.15 the measured extraction time for ions along the beam axis is plotted against the calculated time. For the calculation the single pathways are calculated via equation (6.7).

The data points in figure 6.15 are fitted with a linear equation

$$t_\mathrm{extr,measured} = t_\mathrm{extr,calculated} + t_\mathrm{detector}. \tag{6.8}$$

From the fit the offset is determined with $t_\mathrm{detector} = (0.30 \pm 0.23)\,\mathrm{ms}$.

6.3.1 Extraction time dependancy nozzle voltage

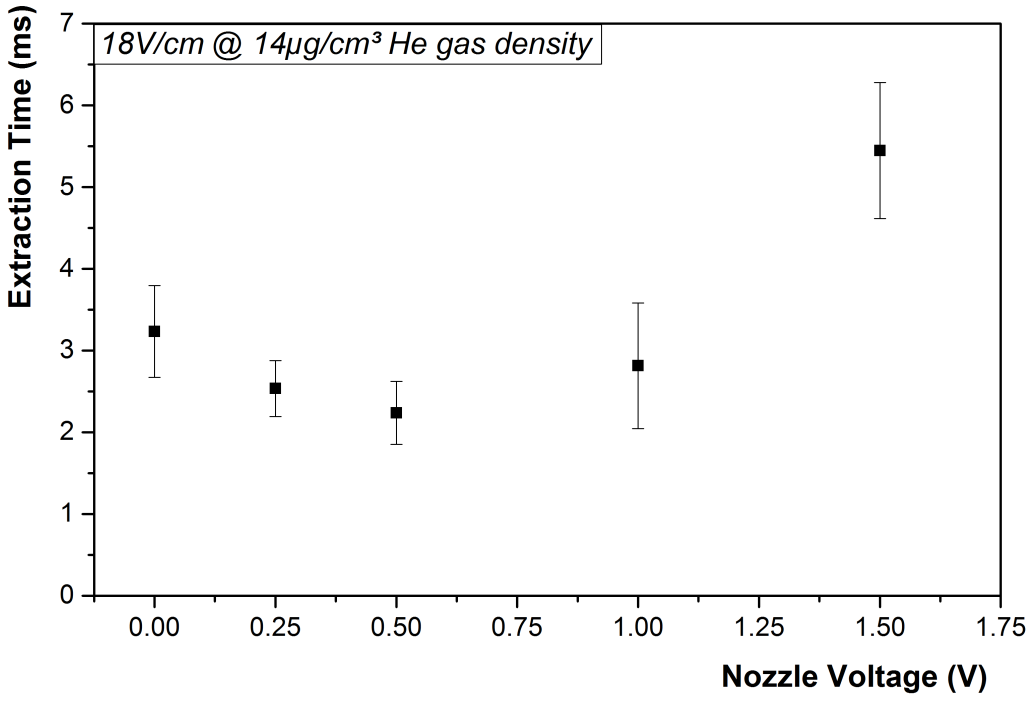

Figure 6.16: Extraction time measurement of ^{215}Po ions for varied nozzle blocking voltages.

Further investigations have been extraction time measurements with ^{215}Po ions stored at the nozzle. The extraction times have been stretched by applying a small

retardation field of $0 - 1.5\,\mathrm{V}$ on the nozzle electrode itself. In standard operation this voltage is used to slow down the ions before their extraction by applying $0.25\,\mathrm{V}$ or maximum $0.5\,\mathrm{V}$. To find the optimum voltage the extraction times have been measured for blocking voltages from $0 - 1.5\,\mathrm{V}$ with the result shown in figure 6.16. It illustrates the performance and the reliability of the measurements. The reason for the in general low efficiencies at pulsed operations of the source is caused by ions attracted from the surface, which thus are hindered on being extracted while the source potential is pulsed down. The extraction times clearly show a preference on the nozzle voltage, as expected the higher the voltage, the longer the extraction times. The more surprising effect is that there seems to be a the minimum that is not located at $0\,\mathrm{V}$ but between $0.25\,\mathrm{V}$ and $0.5\,\mathrm{V}$. The extraction seems to be faster if the transported ions are slowed down in front of the nozzle further. In course of the focusing field of the RF carpet the ions gain more energy than they loose by collisions with the stopping gas. But up to nozzle voltages of $\Delta + 1V$ within the error bars there is no major change in total extraction efficiencies.

Summarised extraction times

Table 6.2 summarises all extraction times given in this chapter. In addition the measurement parameters density ρ, temperature T, He gas pressure p and the electrical field E_{DC} are added. The first three rows belong to the measurements in figures 6.13 and 6.15, respectively. Rows $4 - 8$ belong to the measurements of the extraction time depending on the nozzle blocking potential shown in figure 6.16.

Table 6.2: Collected results of the presented extraction time measurements using ^{215}Po from the internal ion source of the CSC. Below the corresponding parameters of the CSC are given.

ρ $\frac{\mu g}{cm^3}$	T K	p mbar	E_{DC} $\frac{V}{cm}$	t_{extr}^{meas} ms	Δt_{extr}^{meas} ms	comments
14	88	25	19	2.52	0.10	
11	88	20.5	19	2.79	0.10	
5	278	26.5	19	1.86	1.62	
12	85	20.5	18	3.23	0.56	$U_{Nozzle} = 0\,\mathrm{V}$
12	85	20.5	18	2.53	0.34	$U_{Nozzle} = 0.25\,\mathrm{V}$
12	85	20.5	18	2.24	0.39	$U_{Nozzle} = 0.5\,\mathrm{V}$
12	85	20.5	18	2.81	0.77	$U_{Nozzle} = 1\,\mathrm{V}$
12	85	20.5	18	5.45	0.83	$U_{Nozzle} = 1.5\,\mathrm{V}$

6.3.2 Total extraction and transport time of the ion catcher

Another important aspect next to the extraction time of the cryogenic stopping cell is the transport time through the complete system, which means the time between the ejection from the source and the detection on the TOF detector of the MR-TOF-MS. This complete extraction time is plotted in figure 6.17.

Therefore the data acquisition (DAq) Digitizer9353 is used in course of its listmode option. As a trigger signal for the DAq system an additional pulser signal with a fixed correlation to the duty cycle of the ^{223}Ra source a correlated time stamp has been submitted to the Ortec-TDC. Due to the continuous elapsed time of the TDC (the single duty cycles are not summed up directly) each extraction time spectrum needs to be summed up modulated with the time of 0.5 s for one duty cycle. Figure 6.17 a contour plot of this measurement. During the cycle time the source was switched on for 50 ms (10 % duty cycle). The chosen binning for the extraction profile was one MR-TOF MS cycle and corresponds to 2.5 ms.

The extraction and transport time is determined by a data fit with equation (3.73) as demonstrated in figure 6.17 on the projection of the time axis on the top panel. Thus it follows for the transport and extraction time $t_{transport} = 10.44$ ms which mean 4-5 MR-TOF MS cycles for the ions to reach the detector behind the mass spectrometer. There is one cycle needed for extraction from CSC, about two cycles are necessary for transport to the MR-TOF-MS and cooling and there is one cycle the ions spend in the MR-TOF-MS analyser.

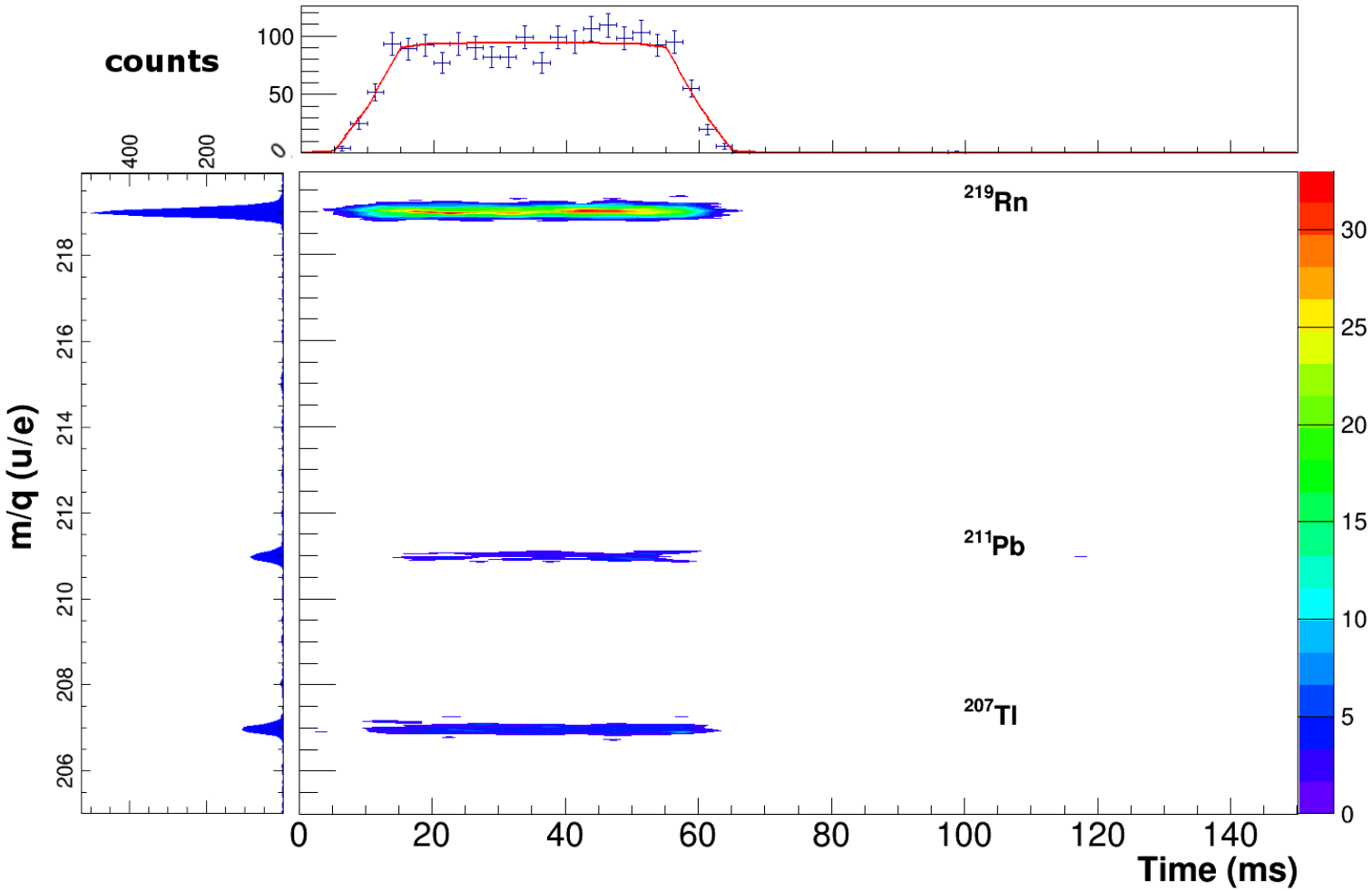

Figure 6.17: Transport time measurements of ^{219}Rn, ^{211}Pb and ^{207}Tl ions from CSC to the MR-TOF MS detector. The measurements cycle was 500 ms the source provided ion with a duty cycle of 10 %. In the spectrum the first 150 ms are shown. The projection of the time profile is shown for ^{219}Rn. The deduced transport time $t_{transport} = 10.44$ ms is evaluated with equation (3.73).

7 Mass and lifetime measurements of the ^{215}Po isotope

In the previous chapter we stated, that the current system and especially the single components can handle short-lived nuclei particularly at high fields and densities. As the extraction time measurements show the system is fast enough to detect even short-lived ions with half-lives in the millisecond range (see figure 6.17). Therefore the Polonium isotope ^{215}Po was chosen which has a half-life of 1.781(4) ms. For further measurements the MR-TOF MS was tuned for the fast operation mode as discussed in chapter 3.3.3 to perform decay spectroscopy and mass measurements with multiple turns.

7.1 Mass measurements of ^{215}Po

High accuracy mass measurements are challenging. We have shown that the FRS Ion Catcher specially overworked is able to measure short lived nulcei. As demonstrated in [Ebert, 2016] the most short-lived ion measured at the FRS IC has been the ^{220}Ra isotope with a half-life of 18 ms so far. With the measurement of the ^{215}Po isotope a new record for a mass measurement of short-lived ions was set. During the measurement period five mass measurements have been performed under different conditions. Due to different temperatures of the He buffer gas the over all gas density of the CSC varied between 28 μg/cm^3 and 49 μg/cm^3 (see table 7.1). The data evaluation was done with MAc (see chapter 4.5.2) and a specially programmed routine for mass measurements in R [Ebert, 2016]. The mass calibration as well as the time resolved calibration was done with MAc. For the mass fitting process the developed 'R routine' was taken.

7.1.1 Calibration

To do a mass calibration of a multi-turn spectrum at least two steps are necessary. First step is the time-focus-shift turn calibration. A spectrum in pass through mode has been taken and converted from time-of-flight to mass. Therefore mass lines of ^{207}Tl, ^{211}Pb and ^{219}Rn nuclei have been taken and fitted with a gauss function, only. The result of the fit delivers T_0 of the calibration function (3.14) and has been calculated for a measurement period only once. Since there are two periods taken in August and September 2015, T_0 has been determined once for each measurement period. For multiple-turn spectra parameters C and b must be fitted using the

corresponding multi-turn spectrum plus the pass through T_0 calibration. Secondly, the resulting mass spectrum needs to be calibrated one more time 'time resolved' to correct for possible peak drifts due to temperature and/or voltage changes. The final calibrated mass spectrum is exported from the data acquisition program MAc (see chapter 4.5) [Pikhtelev, 2014, Bergmann, 2015].

The final mass determination has been done with an exponentially modified gauss (EMG) [Bortels and Collaers, 1987] –the fit function Hyper-EMG [Purushothaman et al., 2017] (chap. 3.3.2). Two different kinds of multiple turn mass spectra have been taken. Since polonium is populated via α-decay and decays via α-decay as well, possible calibrants have a mass difference of $\sim 4\,\mathrm{u}$ always.

For spectrum type one the ions pass the analyser eight times and result in a mass spectrum with a mass resolving power of 16′000 and a mass range of $> 12\,\mathrm{u}$. The taken spectrum is evaluated two times, where the first evaluation is done with the ^{219}Rn isotope as a reference and for the second evaluation the ^{211}Pb isotope was chosen for calibration.

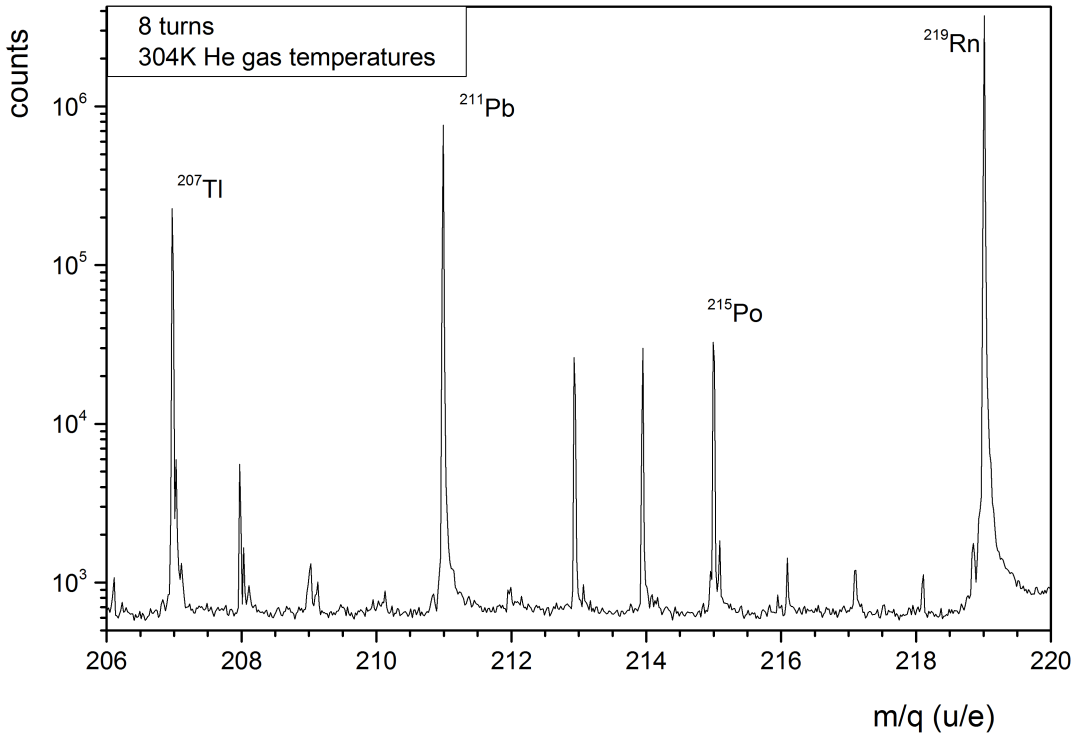

Figure 7.1: Mass spectrum taken with 8 turns in the MR-TOF-MS. The measured mass range was larger than 12 u. The conditions for the stopping cell have been $T(\mathrm{He}) = 304\,K$ ans $p(\mathrm{He}) \approx 25\,mbar$.

The second type of mass measurements are 32 turn spectra. Due to longer flight times the mass window shrinks for 32 turn spectra down to $\sim 8\,\mathrm{u}$. All in all four mass spectra have been taken at the high resolution mode with a maximum mass resolving

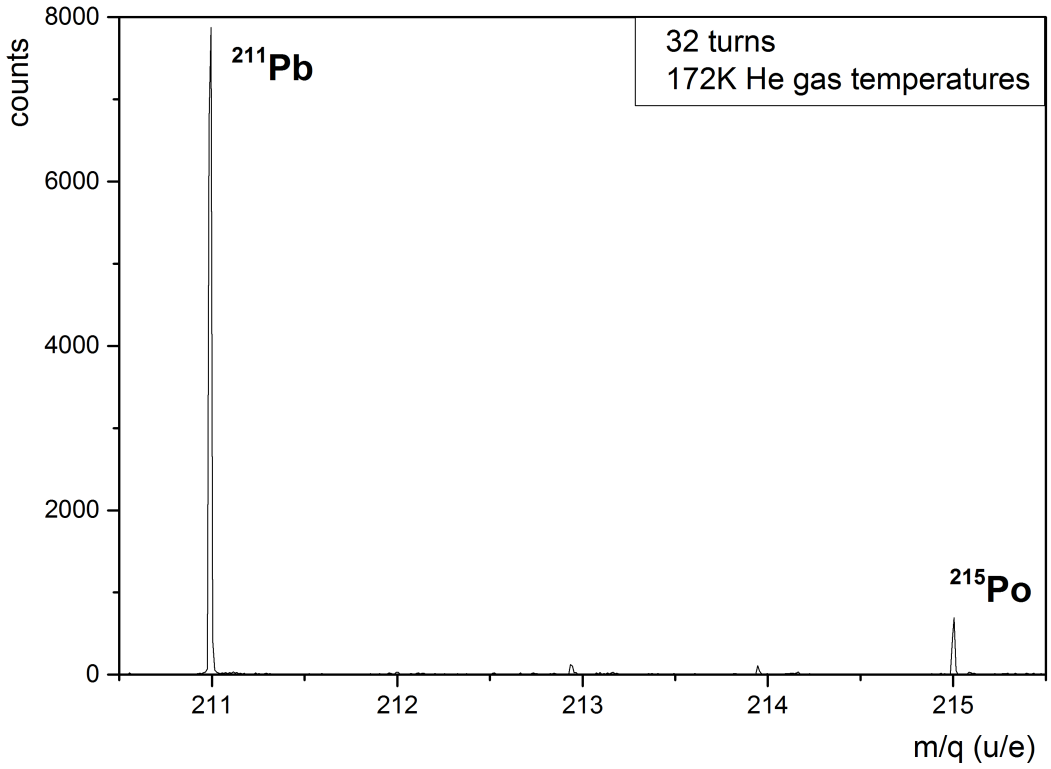

Figure 7.2: Mass spectrum taken with 32 turns inside the time-of-flight analyser, the mass range was set down to 6 u. The conditions for the stopping cell have been $T(\mathrm{He}) = 172\,K$ ans $p(\mathrm{He}) \approx 25\,mbar$

power of 60′000 and 137 ^{215}Po counts. For 32 turn spectra only one calibrant at a time can be taken for a mass determination. Each spectrum taken with a wide mass range that including ^{219}Rn and ^{211}Pb isotopes as possible reference masses the spectrum can lead to shifted flight times for one of the mass peaks. This is a result of not correct adjusted pulsed voltages, thus the shifted ion does see switching fields and is disturbed in its flight path.

In case of two reference ions it needs to be clarified which one is to be trusted or if both calibrations can be taken. The 8 turn spectrum does not give a reason to discard one calibration, that both ^{211}Pb and ^{219}Rn will be taken in the end. In four 32 turn spectra only the first one was taken with two calibrants in the same mass range. Regarding at the two calibration lines the lighter mass of ^{211}Pb is significantly ($\sim 30\%$) broader at the full width half maximum than the one of the ^{219}Rn mass. This peak width indicates a shift in flight times triggered by pulsed fields during the revolution inside the analyser. Thus the ^{219}Rn nuclei will be the final calibrant for analysis. But since ^{219}Rn implanted on the detector once produces noise due to its decay, which is more than having the ^{211}Pb isotope implanted only, for the upcoming measurements the mass window was shifted in such a way as to cut out the ^{219}Rn ions using the TOF analyser.

7.1.2 Mass determination

The final mass determination, i.e. the fitting procedure is done with MAc and the program R. After the time resolved calibration each spectrum is taken and imported in R where the peak shape of the calibrant is determined for each data set and is expected to be conform with the ion of interest's peak shape. During the mass measurements the cooling system of the cryogenic stopping cell was malfunctioning so that cooling was possible with liquid nitrogen and manual filling of the internal dewar only. Long term measurements, that were needed to gain statistics, have been possible with warm stopping gas, only. The expected cleanliness of the extracted ion beam is rather bad due to the warm temperatures. The 8 turn mass spectrum of figure 7.1 shows, besides the high statistic IOI, mass lines at each full mass unit in addition to the constant background. The constant high background can be explained by the fact that the spectrum was taken over 11.5 h constant extraction, a second reason is the pollution of the detector with radio-active nuclei at higher rates, that the decay chain producing α and β particles that trigger the data acquisition with random distributed events. Several tests stated that behaviour. In comparison to the 8 turn spectrum figure 7.2 shows a 32 turn spectrum with less background and a higher IOI rates due to colder stopping gas inside the stopping cell. Here the spectrum is calibrated with the ^{211}Pb isotope. A zoom into the 32 turn spectrum is shown in figure 7.3(bottom) and its calibration ion in 7.3(top). With a mass resolving power of 65000 and a measurement time of less than 2.5 ms.

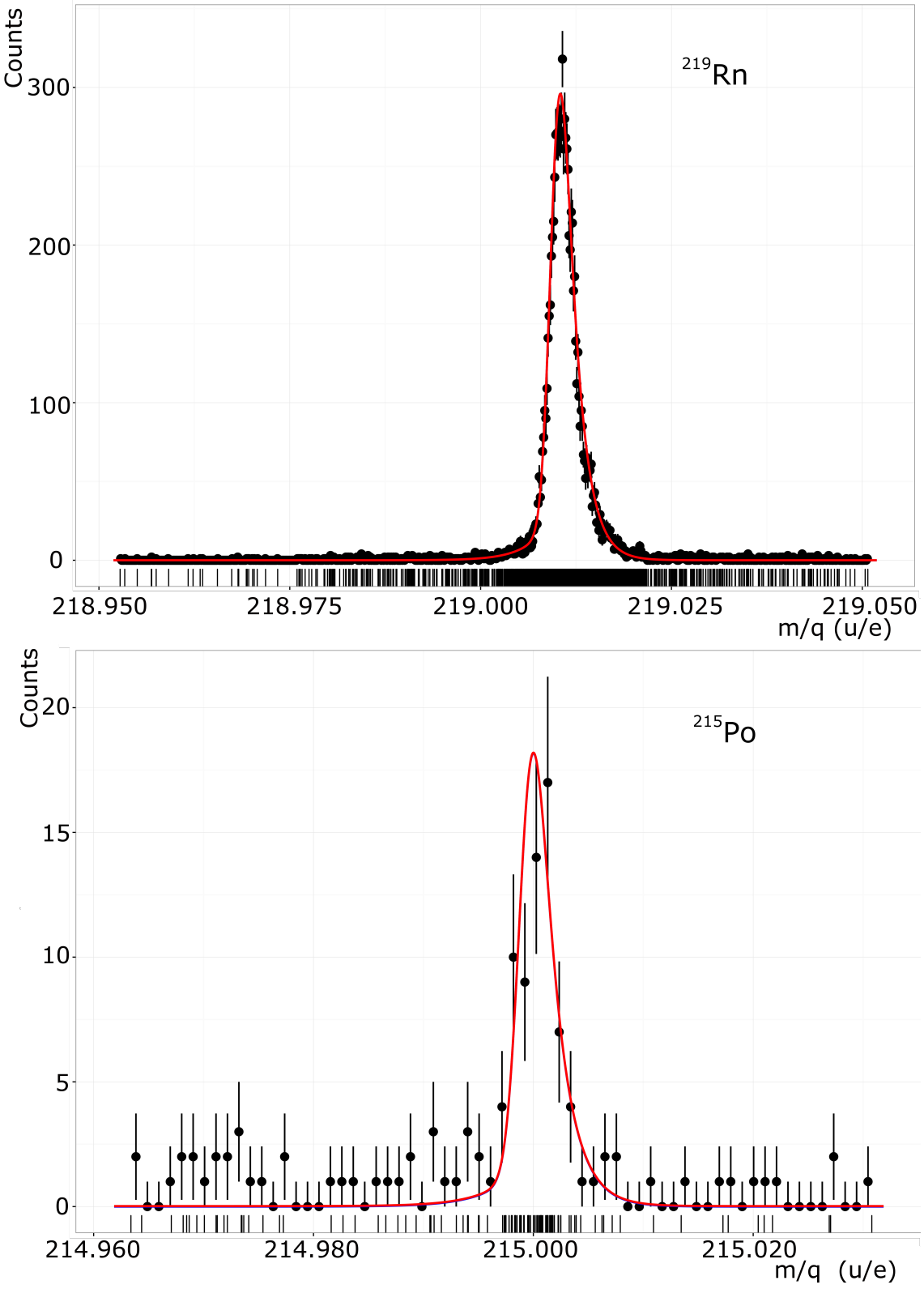

Figure 7.3: Measured mass spectra of ^{219}Rn (top) and ^{215}Po (bottom) ions. The radon isotope has been used as reference ion and provides the peak shape for the ^{215}Po isotope fit (red line). The mass spectrum has a mass resolving power of 60,000. The original unbinned data, recorded in list mode format, is plotted below the histogram and fitted mass spectrum.

Error contribution

The error contribution of the determined mass of the ^{215}Po nucleus is divided into a systematic error and a measurement error, which will be discussed in the following. The measurement error is resulting from the error propagation of five single errors as described in equation (7.1). The error of dt_0 determination (see chapter 3.3.2), the time resolved calibration error contribution dt_{TRC}, the parameter error contribution resulting from the EMG fits of the ion of interest $dm_{\mathrm{EMG,ioi,par}}$ and the calibrant $dm_{\mathrm{EMG,cal,par}}$ (for both see [Ebert, 2016]) and last the error contribution dm_{Bei} which consider a possible contamination of the ioi's mass line. The error contribution of dm_{Bei} is given by a contamination of the mass line of the ion of interest. That means the determined mass can be shifted either to higher or lower mass by having a close lying peak changing the centre of mass. Assuming an under lying second mass line an error was estimated by varying the distance between the two mass lines within ±2 FWHM. The peak height was rated by the background of the ion of interest.

$$dm_{\mathrm{meas}} = \left(dt_0^2 + dt_{\mathrm{TRC}}^2 + dm_{\mathrm{EMG,ioi,par}}^2 + dm_{\mathrm{EMG,cal,par}}^2 + dm_{\mathrm{Bei}}^2\right)^{1/2} \tag{7.1}$$

The contribution to the systematic error is given by the EMG fit's statistical errors. It is consisting of the of calibrant's and ion of interest's by statistical error.

$$dm_{\mathrm{sys}} = \left(dm_{\mathrm{EMG,ioi,stat}}^2 + dm_{\mathrm{EMG,cal,stat}}^2\right)^{1/2} \tag{7.2}$$

The fit results for all measurements are summarised in table 7.1. In figure 7.4 the results are plotted in the form

$$\frac{m_{\mathrm{measurement}} - m_{\mathrm{literature}}}{m_{\mathrm{measurement}}} \cdot 10^6, \tag{7.3}$$

giving the deviation from the literature value in parts per million (10^{-06}). The deviation of 2 ppm for the mass values of the measurement number 2 and 3 do not have a significant systematic error. It does show a slight shoulder which can either result from statistics or be an overlapping contamination that shifts the peak in direction of lower masses.

The weighted mean is calculated using all six data points weighted by their error bar with

$$m_{^{215}\mathrm{Po,final}} = \frac{\sum_{i=1}^{6} \frac{m_i}{\sigma_i}}{\sum_{i=1}^{6} \frac{1}{\sigma_i}} \tag{7.4}$$

and its corresponding error determination

$$\sigma_{^{215}\mathrm{Po,final}} = \left(\sum_{i=1}^{6} \frac{1}{\sigma_i^2} \right)^{-1/2} \tag{7.5}$$

Therefor the final mass value for the ^{215}Po isotope is determined as $(214.9993276 \pm 8.07 \cdot 10^{-05})$ u.

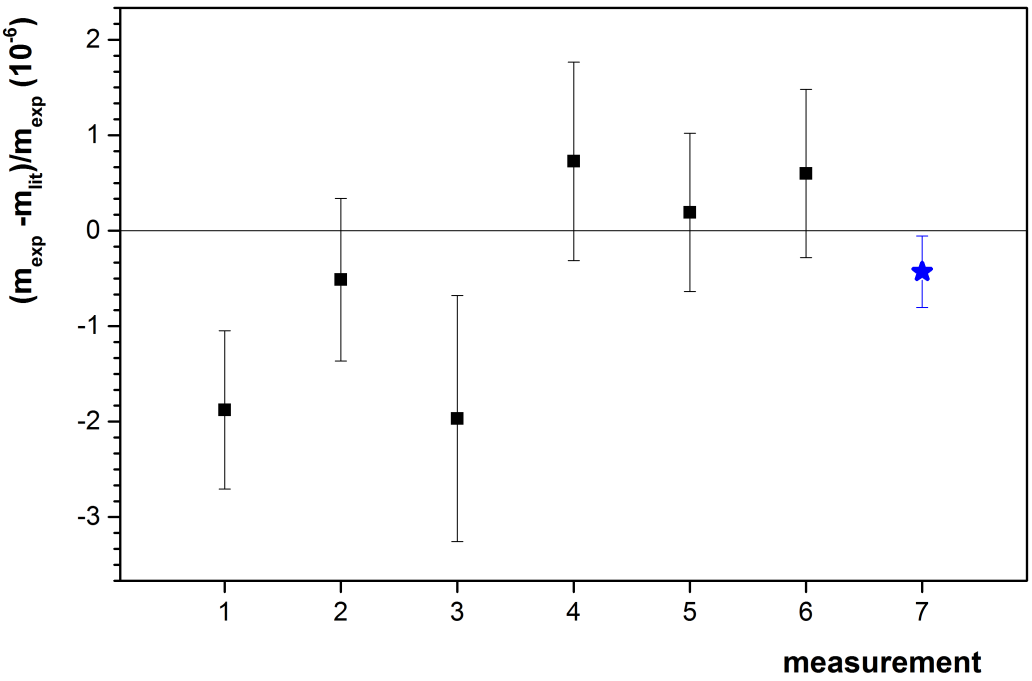

Figure 7.4: Accuracy of the ^{215}Po mass measurements given in parts per million (10^{-06}) for six different measurements. The measurements are calibrated with ^{219}Rn or ^{211}Pb ions (black squares). The average value of the six measurements is indicated by the blue star.

Table 7.1: The table lists boundary conditions for the mass measurements of the ^{215}Po isotope done with the MR-TOF MS. For each measurement a mass value including its error is listed and deviation from literature value [Wang et al., 2012] is listed. The weighted mean of the data

	Density	Pressure	Temp.	N(^{215}Po)	#of Turns	Calib. ion	Mass	Error			Dev. Lit.
								meas.	sys.	overall	
	($\frac{\mu g}{cm^3}$)	mbar	(K)				(u)	(u)	(u)	(u)	(10^{-6})
1	4.1	25.9	304	60044	8	^{211}Pb	214.9993098	$1.76 \cdot 10^{-04}$	$2.67 \cdot 10^{-05}$	$1.78 \cdot 10^{-04}$	−1.88
2	4.1	25.9	304	60044	8	^{219}Rn	214.9990164	$1.81 \cdot 10^{-04}$	$2.71 \cdot 10^{-05}$	$1.83 \cdot 10^{-04}$	−0.51
3	4.1	25.9	304	137	32	^{219}Rn	214.9989971	$2.28 \cdot 10^{-04}$	$1.57 \cdot 10^{-04}$	$2.77 \cdot 10^{-04}$	−1.97
4	4.7	25.8	265	687	32	^{211}Pb	214.9995765	$2.07 \cdot 10^{-04}$	$8.54 \cdot 10^{-05}$	$2.24 \cdot 10^{-04}$	0.73
5	5.9	24.7	203	1201	32	^{211}Pb	214.9994616	$1.36 \cdot 10^{-04}$	$1.15 \cdot 10^{-04}$	$1.78 \cdot 10^{-04}$	0.19
6	7.0	24.9	172	1214	32	^{211}Pb	214.9995490	$1.49 \cdot 10^{-04}$	$1.17 \cdot 10^{-04}$	$1.89 \cdot 10^{-04}$	0.60
	Weighted	mean					214.9993276	$3.25 \cdot 10^{-07}$	$8.73 \cdot 10^{-08}$	$8.07 \cdot 10^{-05}$	−0.430

7.2 Mass selective decay spectroscopy

The mass selective decay spectroscopy has been performed with short-lived ^{215}Po ions. Therefore, the isobar/isomer separation mode of the MR-TOF was chosen and the setup described in section 4.4. The system is operated in the high-resolution mode with 32 turns in the TOF analyser. The data acquisition was pulsed to reset the clock for each MR-TOF-MS cycle which is fixed to 2.5 ms (400 Hz). For each MR-TOF-MS cycle a decay spectrum is recorded and added to the previous ones, see chapter 4.5. To perform MR-TOF assisted decay spectroscopy, the ion of interest needs to be clearly identified to assign the correct TOF through the analyser and the detector. Therefore, an important intermediate step to perform isobar separation is a mass/ time-of-flight spectrum. If the time-of-flight is determined, the Silicon detector can be moved into the beam line to perform α-spectroscopy of the radioactive nuclei behind the time-of-flight analyser.

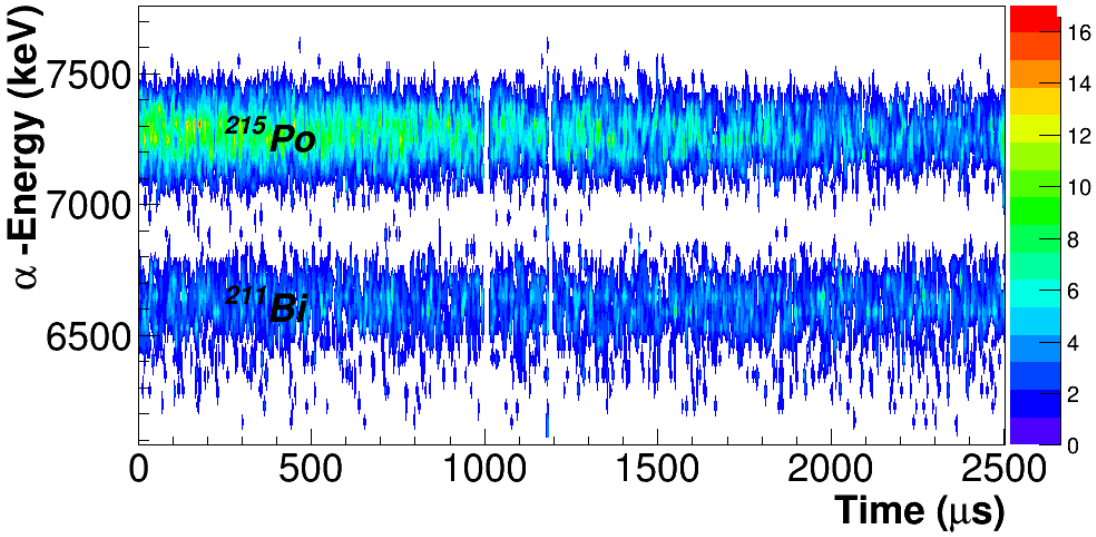

Figure 7.5: α-Decay lines of ^{215}Po and ^{211}Bi during a selected MR-TOF-MS measurement cycle of 2500 μs. The decrease of the ^{215}Po intensity is clearly visible. There are two gaps in the data aquisition appearing at 1000 μs and 1200 μs, that have been taken into account in the data analysis.

The measured α-spectrum is similar to the one shown in figure 6.6 of chapter 6. In this case, no mass selection has been done and all three α-decay daughters of the ^{223}Ra isotope can be directly detected with their energy related channel number and time stamp. The time counting starts by opening the injection trap and the ions entering the TOF analyser. Since we are interested in the time between implanting the ions on the detector and their decay, the spectrum must be time shifted by the time-of-flight through the analyser and to the detector for evaluation. This proced-

ure is necessary for both, the numerical calculation and the standard fit procedure to deliver a correct result.

The relevant decay time is determined by subtracting the time-of-flight and the storage time from the measured total time, i.e. $T_{\mathrm{MR-TOF}} = 1504.93\,\mu$s are subtracted.

In figure 7.5 a time revolution of the detected α-spectrum is shown. On the y-axis the decay channel of the implanted α-emitter is given versus the cycle time of the MR-TOF on the x-axis.

To determine the half-life of polonium the data have been correlated to the α-decay between 7000 keV and 7500 keV.

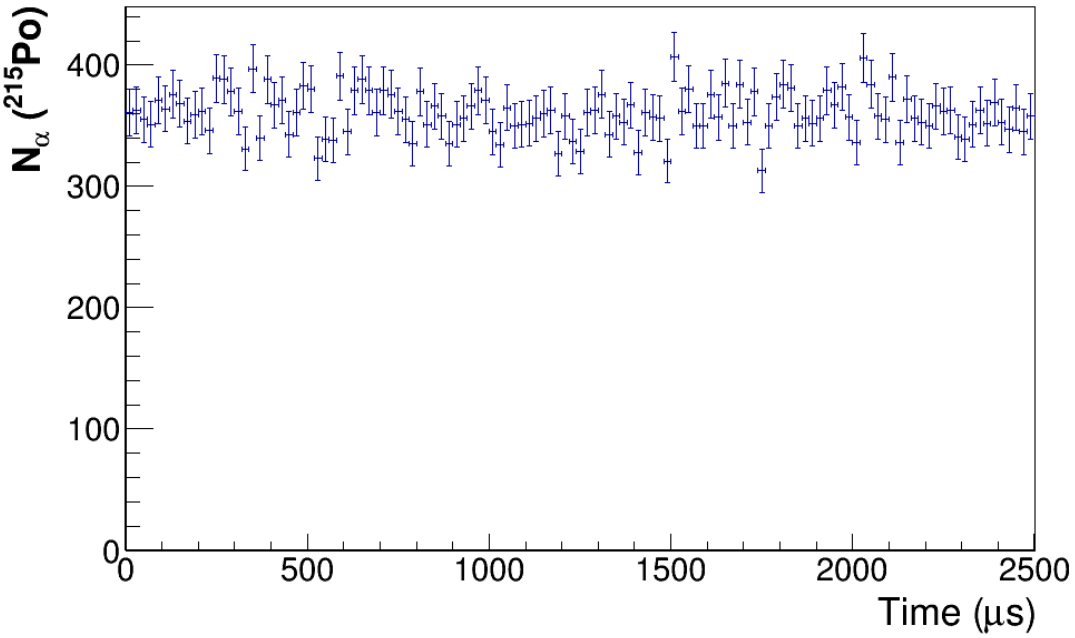

Figure 7.6: α-Decay measurement of ^{215}Po isotopes without gating on the ^{215}Po mass. The decay of ^{215}Po ions is masked by the population from ^{219}Rn ions.

In figure 7.6 the time evolution without the mass selection for ^{215}Po ions is displayed. Without mass tagging of the ^{215}Po isotope the arithmetic mean according to formula (3.56) would yield an unrealistic result. The reason for the incorrect half-life determination is the constant pollution of the polonium via α-decay of the mother nuclide ^{219}Rn with a half-life of 3.96 (1) s [Wang et al., 2012].

It is obvious that this population has to be separated from the Polonium decay channel.Therefore, the ion gate was switched on to deflect all ions except the ^{215}Po. Now the proper decay can be seen in figure 7.7.

Figure 7.5 shows additionally to the time resolved α-spectrum empty spots around $t \approx 1000\,\mu$s and $t \approx 1200\,\mu$s. A third disturbance cannot be seen in the time spectrum is an increase in the count rate. The last impurity may result from the original structure of the data and can be interpreted as rising slope of the decay events, since

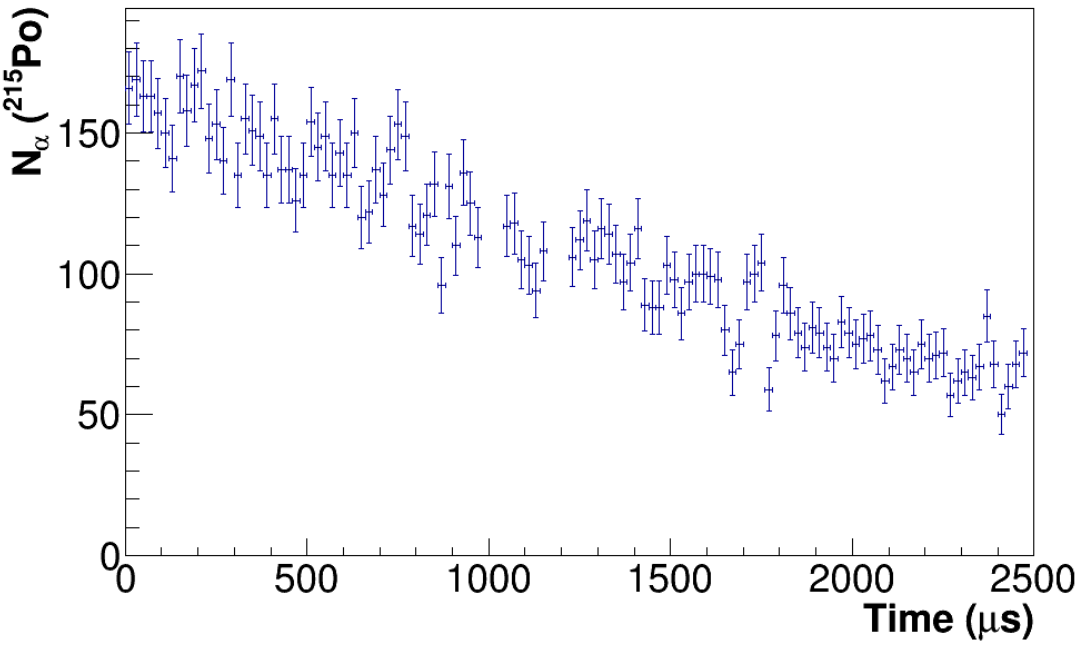

Figure 7.7: α-Decay measurement of ^{215}Po with the gate set on its time-of-flight mass spectrum. The artefacts seen in figure 7.5 have been corrected.

the ion bunch has an extension unequal zero, whereas the other two spots may result from pulsed voltages that hindered the data acquisition by producing dead time and/or overflow of the DAQ. The artefacts in the data evaluation are corrected with equation (3.68) resulting from [Peierls, 1934]. The corrected decay slope is plotted in figure 7.7. The final half-life is determined by the arithmetic mean calculations using equations (3.68) and the error with equation (3.66). Two series of data that have been recorded: A high statistics file containing $\sim 13,000$ decays and a low statistics file containing $\sim 1,000$ polonium decays. Both data sets have been evaluated and a weighted mean is calculated. The results are summarised in table 7.2.

Results of the half-life measurements

The error determination of the half-live measurement is done as described in section 3.4 using equation (3.65). The noise rate on the detector covering the channels of interest was assumed to be one count each ten minutes, which corresponds to a dark count rate $\alpha = 1,6 \cdot 10^{-9} \frac{1}{\mu s}$. With this noise rate the count rate correction done with equation (3.62) can be neglected.

$$s = \frac{m_\alpha s_\alpha - m_N s_N}{m_\alpha - m_N} = \frac{m_N s_N}{m_N} = s_N$$

The correction due to $T \cong \tau$ gives the number of ions implanted on the detector but not detected because they have not decayed during $1T$. Further the count rate was corrected for the time-of-flight through MR-TOF-MS. Regarding on each of the

error contributions equation (3.66) gives the variance of the calculated mean life τ. For the low statistics file (see table 7.2) the standard deviation is

$$\frac{d\tau}{\tau} = 1.34 \cdot 10^{-1}$$

the high statistic file has a standard deviation of

$$\frac{d\tau}{\tau} = 3.21 \cdot 10^{-2}.$$

Thus it follows for the error of single measurements:
high statistics 55.53 μs
low statistics 263.20 μs.

Table 7.2: Half-life measurement of ^{215}Po ions. Two independent measurements have been evaluated and a weighted mean has been calculated. The measurement time T, the number of decays m, mean life τ, half-life $t_{1/2}$

T (μs)	m	s (μs)	τ (μs)	dτ (μs)	$t_{1/2}$ (μs)	d$t_{1/2}$ (μs)
2490	12864	1038	2499.23	89.12	1732.33	55.53
2490	934	1066	2840.06	379.71	1968.58	263.20
Weighted mean			2558.61	78.39	1773.50	55.38

Comparison to the literature value:

$$\frac{1773.50\,\mu\text{s} - 1781\,\mu\text{s}}{1773.50\,\mu\text{s}} = -0.0042. \tag{7.6}$$

The deviation is 0.42% and thus it is in excellent agreement with the literature.

Summary

In modern nuclear- and nuclear astrophysics exotic nuclei are central research topics. Especially close to the driplines these nuclei show novel and unexpected properties compared to the well known stable isotopes. The obtained information from these nuclei can explore the knowledge of stellar nucleosynthesis.

The international Facility for Anti-proton and Ion Research (FAIR-GSI) has the probability to provide important contributions using the Super Fragment Separator (Super-FRS). Novel experimental concepts for measurements with short-lived nuclei are presented in this thesis together with pilot experiments performed at the current Fragment Separator FRS at GSI.

In the context of this doctoral thesis a method to measure very short-lived nuclei has been successfully developed. Therefore projectile fragments have been produced, separated in-flight and thermalised in a cryogenic gas-filled stopping cell. After a fast extraction the stopped projectile fragments are investigated with a high resolution mass spectrometer. The ion's kinetic energy is in the order of several eV for the transport through an RFQ beam line (10^{-2} mbar) and maximal 1.3 keV in the analyser of the mass spectrometer. To reduce the phase space of the ions, they are either He- or N_2-gas cooled.

The efficient stopping of a separated exotic ion beam, produced of a 1000 MeV/u ^{238}U projectiles, is challenging due to their large range distribution. Even though a mono-energetic degrader system reduces the range distributions, they are still bigger than the current areal gas density of the cryogenic stopping cell (CSC). An important goal for future experiments is a higher areal density to achieve the complete and thus efficient stopping of the interesting nuclei.

Effects like space charge or enlarged extraction and transport times have to be minimized because they are limiting the system's performance. If space charge is built up inside the buffer gas, the electrical transport field will be attenuated and a decrease in efficiency will be the result.

In this work, extraction times of 2 ms have been achieved using a different geometry of the CSC. Important parameter dependencies on gas pressure and electrical fields have been tested with success for the next generation CSC that will be built for the Super-FRS at FAIR.

The current CSC shows extraction with full efficiency up to 3×10^{11} He_3^+ ions produced by the incoming fragments, which corresponds an energy loss equivalent of 10^4 ^{221}Ac ions. Higher beam rates cause a drop in extraction efficiencies. The future CSC will provide more than three orders of magnitude higher rate capability as the current system, which enables experiments with even higher background

rates. The obtained results now pave the way for the technical realization of the next generation Ion Catcher for the Super-FRS.

Furthermore, a new concept has been developed to perform accurate mass and life-time measurements of the ^{215}Po isotope. The measurements have been performed under conditions which are foreseen for the Low-Energy Branch of the Super-FRS [Dickel et al., 2015b]. It has been the first direct mass measurement of the ^{215}Po isotope, even though the mass value is well known due to α-spectroscopy and systematics. The obtained mass value of the ^{215}Po isotope is $(214.9993276 \pm 8.07 \cdot 10^{-05})$ u, which is in agreement with the literature value given by $(214.9994201 \pm 2.7 \times 10^{-6})$ u.

The result of the MR-TOF-MS assisted decay spectroscopy of ^{215}Po performed in course of this work is (1.7735 ± 0.055) ms. MR-TOF assisting decay spectroscopy simplifies the spectroscopy measurement by mass identification and separation. It also denotes that there will be no other decay channels but ^{215}Po and its daughter decays to populate the ^{215}Po decay channel undesirably.

Concluding the experimental and simulated results evince that the new concepts for experiments at the Super-FRS are based on solid principles. A completely new generation of accurate measurements of rare isotopes are enabled.

8 Zusammenfassung

Exotische Kerne stehen weltweit im Zentrum der modernen Kern- und nuklearen Astrophysik. Diese Kerne zeigen in der Nähe der Driplinien neue, unerwartete Eigenschaften im Vergleich zu den gut bekannten stabilen Kernen und geben außerdem wichtige Informationen zum Verständnis der Synthese der Elemente in den Sternen. Das internationale Zentrum für Antiprotonen und Ionen Forschung (FAIR-GSI) kann mit dem Separator Super-FRS wichtige Beiträge in dieser Forschungsrichtung leisten. Neuartige experimentelle Entwicklungen für Messungen mit kurzlebigen Kernen am Super-FRS wurden in dieser Arbeit in Pilotexperimenten am bestehenden Fragmentseparator FRS erfolgreich erprobt.

Im Rahmen dieser Doktorarbeit wurde erfolgreich an einer neuen experimentellen Methode zur Untersuchung von sehr kurzlebigen Kernen gearbeitet. Dabei wird der im Flug separierte Strahl von Projektilfragmenten in einer mit gekühltem Heliumgas gefüllten Kammer (CSC) zunächst gestoppt und dann möglichst schnell wieder extrahiert, um die interessanten Kerne in Präzisionsmessungen mit einem hochauflösenden Flugzeitmassenspektrometer zu untersuchen. Die kinetische Energie der Fragmente ist bei diesem Transport und Messungen maximal 1300 keV, wobei der Phasenraum durch Stöße mit Helium- oder Stickstoff-Gas im RFQ-Fallensystem stark reduziert wird.

Die Erzeugung und Separation der exotischen Nuklide mit einem 1000 MeV/u ^{238}U-Projektilstrahl am Eingang des FRS stellt eine große Herausforderung für die effiziente Abbremsung in der kryogenen Stoppkammer dar, weil die Reichweiteverteilung der Fragmente, trotz Einsatz eines monoenergetischen Degradersystems am FRS, wegen der hohen kinetischen Energie noch breiter ist als die momentan erreichbare Flächendichte des Heliumgases in der CSC. Somit ist es ein Ziel, dass man eine möglichst große Flächendichte im Heliumgas anstreben muss, um die interessanten Kerne vollständig im Gasvolumen abzubremsen.

Dabei müssen störende Effekte, wie auftretende Raumladung oder längere Extraktionszeiten, vermieden werden, weil sie einen effizienten Transport der gestoppten Ionen verhindern. Ausgebildete Raumladungszonen schwächen die elektrischen Felder zum Extrahieren der Ionen ab, sodass nur noch ein Bruchteil der thermischen Ionen die Stoppzelle verlässt.

In dieser Arbeit konnten Extraktionszeiten von 2 ms mit einer neuen Geometrie in der Stoppzelle erreicht werden. Es wurden dabei Abhängigkeiten von wichtigen Parameter, wie Gasdruck und Feldstärken, für die geplante FAIR Stoppzelle erfolgreich getestet. Die gegenwärtige CSC hat noch die volle Extraktionseffizienz bei einem erzeugten Plasma von 3×10^{11} He_3^+ Ionen im Abbremsgas. Dieser Ionisationsdichte entsprechen etwa einem Energieverlust von 10^4 ^{221}Ac Ionen. Die zukün-

ftige Stoppzelle wird eine um mehr als 1000-fache Ratenfestigkeit haben als die gegenwärtige Anordnung und kann somit auch bei höheren Untergrundraten noch zuverlässig arbeiten. Mit diesen experimentellen Ergebnissen steht nun der technischen Realisierung des zukünftigen Ion-Catchers für die Super-FRS Anlage im Prinzip nichts mehr im Wege.

Zur weiteren Demonstration des neuen Konzeptes wurden die Masse und die Halbwertszeit ^{215}Po Ionen erfolgreich unter Bedingungen gemessen, die für die neue Stoppzelle [Dickel et al., 2015a] am Super-FRS vorgesehen sind. Die Masse von einfach geladenen $^{215}Po^{1+}$ Ionen wurde mit der neuen Testanordnung erstmals direkt gemessen, denn die vorhandenen Werte in der Literatur basieren auf Messungen, die mittels α-Spektroskopie gewonnen wurden. Massenbestimmungen, die aus der Zerfallsspektroskopie abgeleitet wurden, haben stets die schwierige Voraussetzung, dass Anfangs- und Endzustände genau bekannt sein müssen. Der gemessene Massenwert beträgt $(214.9993276 \pm 8.07 \cdot 10^{-05})$ u und ist somit innerhalb der Messfehler in sehr guter Übereinstimmung mit dem Literaturwert von $(214.9994201 \pm 2.7 \times 10^{-6})$ u.

Die in dieser Arbeit gemessene Lebensdauer von ^{215}Po Ionen beträgt (1.7735 ± 0.055) ms. Die Lebensdauermessung war erst durch die Bedingung der koinzidenten Massenidentifikation ermöglicht. Ohne diese experimentelle Bedingung würde die Bevölkerung von ^{215}Po Ionen als Tochterprodukt von ^{219}Rn Ionen den zeitlichen Verlauf dominieren.

Mit den experimentellen und simulierten Ergebnissen dieser Arbeit konnte überzeugend gezeigt werden, dass die geplanten Konzepte für die Experimente am Super-FRS auf soliden experimentellen Grundlagen basieren.

Danksagung

Geschafft. Ich glaube, das war mein erster Gedanke, nachdem ich den letzten Satz zu Papier brachte. Nach fast fünf Jahren mit vielen Höhen und Tiefen halte ich nun das Resultat in der Hand.
Ich möchte mich im Zuge dieser Arbeit bei den Menschen bedanken, die mir geholfen haben meine Promotion erfolgreich abzuschließen.

Zuerst möchte ich mich bei Prof. Hans Geissel bedanken, für eine sehr gute, produktive Betreuung während meiner Promotion. Dein Engagement und deine Motivation waren immer sehr ansteckend und inspirierend.

Ebenso bei Prof. Christoph Scheidenberger, der mir die Mglichkeit gab in der IONAS-Gruppe am Ion Catcher Experiment zu promovieren.

Bedanken möchte ich mich ebenfalls bei Dr. Wolfgang Plaß und Dr. Timo Dickel für die zahlreichen weiterführenden wissenschaftlichen Diskussionen, die Unterstützung und die freundliche Aufnahme in die Gruppe.

Ein großer Dank geht auch an die Mitglieder der IONAS-Gruppe. Insbesondere an Samuel Ayet und Christine Hornung sowie Ivan Miskun für zahllose und manchmal auch unendliche lange Tage im Labor am Ion Catcher experiment an der GSI. Dr. Pascal Reiter und Dr. Sivaji Purushothaman für eine exzellente Zusammenarbeit an der kryogenen Stoppzelle und produktiven Kaffee- bzw. Teepausen. Genauso möchte ich mich bedanken bei Dr. Jens Ebert, Florian Greiner, Julian Bergmann, Dr. Wayne Lippert und Dr. Christian Jesch für die großartige Zusammenarbeit überwiegend in Gießen in den letzten Jahren. Bei Dr. Stephane Pietri und Dr. Emma Haettner für anregende Diskussionen und eine helfende Hand wenn immer notwendig. Bei Evelin Prinz, die uns stets fern von den Mühlen der Bürokratie gehalten hat und viel Nervenstärke beweisen musste im ein oder anderen Fall...

Ein besonderer Dank gilt auch den Ingenieuren und Technikern sowohl an der GSI als auch in Gießen für die zuverlässige Unterstützung an den Experimenten und den vielen last-minuit Reparaturen bzw Änderungen.

Weiter möchte ich mich bei meinen Freunden bedanken, die mich vorallem aber von Zeit zu Zeit zurück ins Leben außerhalb der Physik geholt haben.

Zu Guter Letzt möchte ich mich bei meiner Familie bedanken, meiner Schwester Melanie und meinen Eltern Andrea und Roland, die mich während meines Studiums immer unterstützt haben. Vorallem möchte ich mich aber bei meinem Freund Jan bedanken, für die ungezählten Momente an denen du immer zur Stelle warst.

Erklärung

Ich habe die vorgelegte Dissertation selbstständig und ohne unerlaubte fremde Hilfe und nur mit den Hilfen angefertigt, die ich in der Dissertation angegeben habe. Alle Textstellen, die wörtlich oder sinngemäß aus veröffentlichten Schriften entnommen sind, und alle Angaben, die auf mündlichen Auskünften beruhen, sind als solche kenntlich gemacht. Ich stimme einer evtl. Überprüfung meiner Dissertation durch eine Antiplagiat-Software zu. Bei den von mir durchgeführten und in der Dissertation erwähnten Untersuchungen habe ich die Grundsätze guter wissenschaftlicher Praxis, wie sie in der Satzung der Justus-Liebig-Universität Gießen zur Sicherung guter wissenschaftlicher Praxis niedergelegt sind, eingehalten.

Gießen, den 24. September 2017

Ann-Kathrin Rink

Bibliography

[Äysto, 2001] Äysto, J. (2001). Development and applications of the IGISOL technique. *Nuclear Physics A*, 693:477–494.

[Batygin, 2011] Batygin, Y. K. (2011). Space charge effects in cyclotron gas stopper. *Nuclear Instruments and Methods in Physics Research Section A: Accelerators, Spectrometers, Detectors and Associated Equipment*, 629(1):37–42.

[Bergmann, 2015] Bergmann, J. (2015). Entwicklung und Anwendung einer integrierten Systemsteuerung und Datenaufnahme für Flugzeitmassenspektrometer. Master's thesis, Justus-Liebig-Universität Gießen.

[Bethe, 1932] Bethe, H. A. (1932).

[Bjørnstad et al., 1986] Bjørnstad, T., Hagebø, E., Hoff, P., O.C.Jonsson, Kugler, E., Ravn, H. L., Sundell, S., Vosicki, B., and Collaboration, I. (1986). Methods for Production of Intense Beams of Unstable Nuclei: New Developments at ISOLDE. *Physica Scripta*, 34:578–590.

[Blumenfeld et al., 2013] Blumenfeld, Y., Nilsson, T., and Duppen, P. V. (2013). Facilities and methods for radioactive ion beam production. *Physica Scripta*, T152(014023).

[Bohr, 1913] Bohr, N. (1913). On the Constitution of Atoms and Molecules. *Philosophilcal Magazine*, 26(6):1–25.

[Bortels and Collaers, 1987] Bortels, G. and Collaers, P. (1987). Analytical function for fitting peaks in alpha-particle spectra from Si detectors. *Appl. Radiat. Isot.*, 38:831–837.

[Bradbury and Nielsen, 1936] Bradbury, N. E. and Nielsen, R. A. (1936). Absolute values of the electron mobility in hydrogen. *Phys. Rev.*, 49:388–393.

[Dahl, 2000] Dahl, D. A. (2000). SIMION for the personal computer in reflection. *International Journal of Mass Spectrometry*, 200(1-3):3 – 25.

[Dawson, 1976] Dawson, P. H. (1976). *Quadrupole Mass Spectrometry and its applications*. Elsevier Scientific Publishing Company, Amsterdam-Oxford-New York. Chap. II, Editor: P. H. Dawson.

[de Jong et al., 1997] de Jong, M., Ignatyuk, A., and Schmidt, K.-H. (1997). Angular momentum in peripheral fragmentation reactions. *Nuclear Physics A*, 613(4):435–444.

[Dehmelt, 1967] Dehmelt, H. G. (1967). Radiofrequency spectroscopy of stored ions I: Storage. *Adv. At. Mol. Phys.*, 3:53–72.

[Demtröder, 2010] Demtröder, W. (2010). *Experimentalphysik 3: Atome, Moleküle und Festkörper*. Springer-Verlag.

[Dendooven, 1997] Dendooven, P. (1997). The development and status of the IGISOL technique. *Nuclear Instruments and Methods B*, 126:184–189.

[Dickel, 2010] Dickel, T. (2010). *Design and Commissioning of an Ultra-High-Resolution Time-of-Flight Based Isobar Separator and Mass Spectrometer*. PhD thesis, Justus-Liebig-Universität Gießen.

[Dickel et al., 2016] Dickel, T., Plaß, W., Geissel, H., Heiße, F., Miskun, I., Purushothaman, S., Reiter, M., Rink, A.-K., and Scheidenberger, C. (2016). Conceptual design of a novel next-generation cryogenic stopping cell for the Low-Energy Branch of the Super-FRS. *Nuclear Instruments and Methods in Physics Research B*, (376):216–220.

[Dickel et al., 2015a] Dickel, T., Plaß, W. R., Ayet San Andres, S., Ebert, J., Geissel, H., Haettner, E., Hornung, C., Miskun, I., Pietri, S., Purushothaman, S., Reiter, M. P., Rink, A. K., Scheidenberger, C., Weick, H., Dendooven, P., Diwisch, M., Greiner, F., Heiße, F., Knöbel, R., Lippert, W., Moore, I. D., Pohjalainen, I., Prochazka, A., Ranjan, M., Takechi, M., Winfield, J. S., and Xu, X. (2015a). First spatial separation of a heavy ion isomeric beam with a multiple-reflection time-of-flight mass spectrometer. *Phys. Lett. B*, 744:137–141.

[Dickel et al., 2015b] Dickel, T., Plaß, W. R., Becker, A., Czok, U., Geissel, H., Haettner, E., Jesch, C., Kinsel, W., Petrick, M., Scheidenberger, C., and Yavor, M. I. (2015b). A high-performance multiple-reflection time-of-flight mass spectrometer and isobar separator for the research with exotic nuclei. *Nucl. Instrum. Meth. A*, 777:172–188.

[Diwisch, 2015] Diwisch, M. (2015). *Present and Future Isochronous Mass Spectrometry at GSI-FAIR: 25 New Masses of Fission Fragments; Novel Analysis Method; Design of a New Time-of-Flight Detector System*. Phd thesis, Justus-Liebig-University Gießen.

[Ebert, 2016] Ebert, J. (2016). *Mass Measurements of ^{238}U-Projectile Fragments for the First time with a Multiple-Reflection Time-of-flight Mass Spectrometer*. Phd thesis, Justus-Liebig-University Gießen.

[FLNR, 2017] FLNR (May 2017). http://flerovlab.jinr.ru/flnr/GaLs/phys_bg.html.

[Franzke, 1987] Franzke, B. (1987). The heavy ion storage and cooler ring project ESR at GSI. *Nucl. Instrum. Meth. B*, 24/25:18–25.

[Franzke et al., 2008] Franzke, B., Geissel, H., and Münzenberg, G. (2008). Mass and lifetime measurements of exotic nuclei in storage rings. *Mass Spectrom. Rev.*, 27:428–469.

[Freedmann and Diaconis, 1981] Freedmann, D. and Diaconis, P. (1981). On the histogram as a density estimator: L 2 theory. *Zeitschrift für Wahrscheinlichkeitstheorie und verwandte Gebiete*, 57(4):453–476.

[Gaimard and Schmidt, 1991] Gaimard, J.-J. and Schmidt, K.-H. (1991). A reexamination of the abrasion-ablation model for the description of the nuclear fragmentation reaction. *Nuclear Physics A*, 531(3-4):709–745.

[Geissel et al., 1992] Geissel, H., Armbruster, P., Behr, K. H., Brünle, A., Burkard, K., Chen, M., Folger, H., Franczak, B., Keller, H., Klepper, O., Langenbeck, B., Nickel, F., Pfeng, E., Pfützner, M., Roeckl, E., Rykaczewski, K., Schall, I., Schardt, D., Scheidenberger, C., Schmidt, K. H., Schröter, A., Schwab, T., Sümmerer, K., Weber, M., Münzenberg, G., Brohm, T., Clerc, H. G., Fauerbach, M., Gaimard, J. J., Grewe, A., Hanelt, E., Knödler, B., Steiner, M., Voss, B., Weckenmann, J., Ziegler, C., Magel, A., Wollnik, H., Dufour, J. P., Fujita, Y., Vieira, D. J., and Sherrill, B. (1992). The GSI projectile fragment separator (FRS): a versatile magnetic system for relativistic heavy ions. *Nucl. Instrum. Meth. B*, 70(1-4):286 – 297.

[Geissel et al., 1995] Geissel, H., Münzenberg, G., and Riisager, K. (1995). Secondary Exotic Nuclear Beams. *Annu. Rev. Nucl. Part. Sci.*, 45:163–203.

[Geissel et al., 1989] Geissel, H., Schwab, T., Armbruster, P., Dufour, J., Hanelt, E., Schmidt, K.-H., Scherrill, B., and Münzenberg, G. (1989). Ions penetrating through ion-optical systems and matter - non-liouvillian phase-space modelling. *Nucl. Instrum. Meth. A*, 282:247–260.

[Geissel et al., 2002] Geissel, H., Weick, H., Scheidenberger, C., Bimbot, R., and Gardes, D. (2002). Experimental studies of heavy-ion slowing down in matter. *Nuclear Instruments and Methods in Physics Research Section B: Beam Interactions with Materials and Atoms*, 195(1):3–54.

[Geissel et al., 2003] Geissel, H., Weick, H., Winkler, M., Münzenberg, G., Chichkine, V., Yavor, M., Aumann, T., Behr, K. H., Böhmer, M., Brünle, A., Burkard, K., Benlliure, J., Cortina-Gil, D., Chulkov, L., Dael, A., Ducret, J.-E., Emling, H., Franczak, B., Friese, J., Gastineau, B., Gerl, J., Gernhäuser, R., Hellström, M., Jonson, B., Kojouharova, J., Kulessa, R., Kindler, B., Kurz, N., Lommel, B., Mittig, W., Moritz, G., Mühle, C., Nolen, J. A., Nyman, G., Roussell-Chomaz, P., Scheidenberger, C., Schmidt, K.-H., Schrieder, G., Sherrill, B., Simon, H.,

Sümmerer, K., Tahir, N. A., Vysotsky, V., Wollnik, H., and Zeller, A. F. (2003). The Super-FRS project at GSI. *Nucl. Instrum. Meth. B*, 204:71–85.

[Greiner, 2013] Greiner, F. (2013). *Construction and Commissioning of an RF Quadrupole Switchyard (in German)*. Bachelor thesis, Justus-Liebig-University Gießen.

[Haettner, 2011] Haettner, E. (2011). *A novel radio frequency quadrupole system for SHIPTRAP & New mass measurements of rp nuclides*. PhD thesis, Justus-Liebig-Universität Gießen.

[Haettner, 2012] Haettner, E. (2012). personal communication.

[Heiße, 2015] Heiße, F. (2015). *Investigation of the cryogenic gas-filled stopping cell for the FRS Ion Catcher*. MSc thesis, Technische Universität Dresden.

[Helm, 1976] Helm, H. (1976). The mobilities and equilibrium reactions of helium ions in helium at 77 K. *Journal of Physics: Atom. Molec. Phys.*, 9(7):1171–1189.

[Huyse et al., 2002] Huyse, M., Facina, M., Kudryavtsev, Y., and Duppen, P. V. (2002). Intensity limitations of a gas cell for stopping, storing and guiding of radioactive ions. *Nucl. Instrum. Methods B*, 187:535–547.

[ISOLDE,] ISOLDE. Yield Database 2015.

[Jesch, 2008] Jesch, C. (2008). *Injektions-Ionenfallensystem für ein Multireflektions-Flugzeitmassenspektrometer*. Diploma thesis, Justus-Liebig-University Gießen.

[Kratz et al., 1993] Kratz, K.-L., Bitouzet, J.-P., Thielemann, F.-K., Moeller, P., and Pfeiffer, B. (1993). Isotopic r-process abundances and nuclear structure far from stability-implications for the r-process mechanism. *The Astrophysical Journal*, 403:216–238.

[Kreim et al., 2013] Kreim, S., Atanasov, D., Beck, D., Blaum, K., Böhm, C., Borgmann, C., Breitenfeld, M., Cocolios, T. E., Fink, D., George, S., Herlert, A., Kellerbauer, A., Köster, U., Kowalska, M., Lunney, D., Manea, V., Ramirez, E. M., Naimi, S., Neidherr, D., Nicol, T., Rossel, R. E., Rosenbusch, M., Schweikhard, L., Stanja, J., Wienholtz, F., Wolf, R., and Zuber, K. (2013). Recent exploits of the ISOLTRAP mass spectrometer. *Nucl. Instrum. Methods B*, 317:492–500.

[Leo, 1994] Leo, W. R. (1994). *Techniques for Nuclear and Particle Physics Experiments*. Springer, Berlin, Heidelberg, New York.

[Lindhard and Sœrensen, 1996] Lindhard, J. and Sœrensen, A. H. (1996). Relativistic theory of stopping for heavy ions. *Physical Review A*, 53(4):2443.

[Lorentz, 1937] Lorentz, H. A. (1937). Electromagnetic phenomena in a system moving with any velocity smaller than that of light. In *Collected Papers*, pages 172–197. Springer.

[Lotze, 2014] Lotze, C. (2012-2014). personal communication.

[Manura and Dahl, 2006] Manura, D. J. and Dahl, D. A. (2006). *SIMION 8.0 User Manual*. Sci. Instrument Services, Inc., Idaho Nat. Lab.

[Miskun, 2014] Miskun, I. (2014). *Commissioning, performance and possible application of RFQ mass-filter in the diagnostic unit of the FRS Ion Catcher facility*. Master thesis, Justus-Liebig-University Gießen.

[Münzenberg, 1992] Münzenberg, G. (1992). Separation Techniqes for Secondary Beams. *Nucl. Inst. Meth B*.

[Neumayr et al., 2006] Neumayr, J., Beck, L., Habs, D., Heinz, S., Szerypo, J., Thirolf, P., Varentsov, V., Voit, F., Ackermann, D., Beck, D., Block, M., Di, Z., Eliseev, S., Geissel, H., Herfurth, F., Heßberger, F., Hofmann, S., Kluge, H.-J., Mukherjee, M., Münzenberg, G., Petrick, M., Quint, W., Rahaman, S., Rauth, C., Rodriguez, D., Scheidenberger, C., Sikler, G., Wang, Z., Weber, C., Plaß, W., Breitenfeldt, M., Chaudhuri, A., Marx, G., Schweikhard, L., Dodonov, A., Novikov, Y., and Suhonen, M. (2006). The ion-catcher device for SHIPTRAP. *Nucl. Instrum. Meth. B*, 244:489–500.

[Paul and Steinwedel, 1953] Paul, W. and Steinwedel, H. (1953). Ein neues massenspektrometer ohne magnetfeld. *Z. Naturforschung*, 8a:448–451.

[Peierls, 1934] Peierls, R. (1934). Statistical Error in Counting Experiments. *Royal Society Publishing*.

[Petrick et al., 2008] Petrick, M., Plaß, W., Behr, K.-H., Brünle, A., Caceres, L., Clark, J., Di, Z., Elisseev, S., Facina, M., Fettouhi, A., Geissel, H., Hüller, W., Huyse, M., Karagiannis, C., Kindler, B., Knöbel, R., Kudryavtsev, Y., Kurcewicz, J., Levant, T., Litvinov, Y. A., Lommel, B., Maier, M., Morrissey, D., Münzenberg, G., Portillo, M., Savard, G., Scheidenberger, C., Duppen, P. V., Weick, H., Winkler, M., and Zabransky, B. (2008). Online test of the FRS Ion Catcher at GSI. *Nucl. Instrum. Meth. B*, 266:4493–4497.

[Pikhtelev, 2014] Pikhtelev, A. (2014). personal communication. Original version of MAc software.

[Plaß et al., 2015] Plaß, W. R., Dickel, T., Ayet San Andres, S., Ebert, J., Greiner, F., Hornung, C., Jesch, C., Lang, J., Lippert, W., Majoros, T., Short, D., Geissel, H., Haettner, E., Reiter, M. P., Rink, A.-K., Scheidenberger, C., and Yavor, M. I. (2015). High-performance multiple-re ection time-of- ight mass spectrometers for research with exotic nuclei and for analytical mass spectrometry. *Physica Scripta*,

T166:134–144.

[Plaß et al., 2013a] Plaß, W. R., Dickel, T., Purushothaman, S., Dendooven, P., Geissel, H., Ebert, J., Haettner, E., Jesch, C., Ranjan, M., Reiter, M. P., Weick, H., Amjad, F., Ayet, S., Diwisch, M., Estrade, A., Farinon, F., Greiner, F., Kalantar-Nayestanaki, N., Knöbel, R., Kurcewicz, J., Lang, J., Moore, I., Mukha, I., Nociforo, C., Petrick, M., Pfuetzner, M., Pietri, S., Prochazka, A., Rink, A.-K., Rinta-Antila, S., Schäfer, D., Scheidenberger, C., Takechi, M., Tanaka, Y. K., Winfield, J. S., and Yavor, M. I. (2013a). The FRS Ion Catcher - a facility for high-precision experiments with stopped projectile and fission fragments. *Nucl. Instrum. Meth. B*, 317:457–462.

[Plaß et al., 2013b] Plaß, W. R., Dickel, T., and Scheidenberger, C. (2013b). Multiple-reflection time-of-flight mass spectrometry. *Int. J. Mass Spectrom.*, 349:134–144.

[Poschenrieder, 1972] Poschenrieder, W. P. (1972). Multiple-focusing time-of-flight mass spectrometers part II. TOFMS with equal energy acceleration. *Int. J. Mass Spectrom. Ion Phys.*, 9:357–373.

[Purushothaman et al., 2017] Purushothaman, S., Andres, S. A. S., J.Bergman, Dickel, T., Ebert, J., Geissel, H., Hornung, C., Plaß, W., Rappold, C., Scheidenberger, C., Tanaka, Y., and Yavor, M. (2017). Hyper-EMG: A new probability distribution function composed of Exponetially Modified Gaussian distributions to analyse asymmetric peak shapes in high-resolution time-of-flight mass spectrometry. *International Journal of mass spectrometry.*

[Purushothaman et al., 2013] Purushothaman, S., Reiter, M. P., Haettner, E., Dendooven, P., Dickel, T., Geissel, H., Ebert, J., Jesch, C., Plaß, W. R., Ranjan, M., Weick, H., Amjad, F., Ayet, S., Diwisch, M., Estrade, A., Farinon, F., Greiner, F., Kalantar-Nayestanaki, N., Knöbel, R., Kurcewicz, J., Lang, J., Moore, I., Mukha, I., Nociforo, C., Petrick, M., Pfuetzner, M., Pietri, S., Prochazka, A., Rink, A.-K., Rinta-Antila, S., Scheidenberger, C., Takechi, M., Tanaka, Y. K., Winfield, J. S., and Yavor, M. I. (2013). First online results of a cryogenic stopping cell with short-lived heavy uranium fragments produced at 1000 MeV/u. *Eur. Phys. Lett.*, 104:42001.

[Ranjan et al., 2015] Ranjan, M., Dendooven, P., Purushothama, S., Dickel, T., Reiter, M. P., Ayet, S., Haettner, E., Moore, I. D., Kalantar-Nayestanaki, N., Geissel, H., Plaß, W. R., Schäfer, D., Scheidenberger, C., Schreuder, F., Timersma, H., Van de Walle, J., and Weick, H. (2015). Design, construction and cooling system performance of a prototype cryogenic stopping cell for the Super-FRS at FAIR. *Nucl. Instrum. Methods A*, 770:87–97.

[Ranjan et al., 2011] Ranjan, M., Purushothaman, S., Dickel, T., Geissel, H., Plaß, W. R., Schäfer, D., Scheidenberger, C., Van de Walle, J., Weick, H., and

Dendooven, P. (2011). New stopping cell capabilities: RF carpet performance at high gas density and cryogenic operation. *Eur. Phys. Lett.*, 96:52001.

[Ravn et al., 1975] Ravn, H. L., Sundell, S., and Westgaard, L. (1975). Target Techniques for the ISOLDE ON-LINE Isotope Separator. *Nuclear Instrumets and Methods*, (123):131–144.

[Reiter et al., 2016] Reiter, M., Rink, A.-K., Dickel, T., Haettner, E., Heiße, F., Plaß, W., Purushothaman, S., Amjad, F., Andrés, S. A. S., Bergmann, J., Blum, D., Dendooven, P., Diwisch, M., Ebert, J., Geissel, H., Greiner, F., Hornung, C., Jesch, C., Kalantar-Nayestanaki, N., Knöbel, R., Lang, J., Lippert, W., Miskun, I., Moore, I., Nociforo, C., Petrick, M., Pietri, S., Pfützner, M., Pohjalainen, I., Prochazka, A., Scheidenberger, C., Takechi, M., Tanaka, Y., Weick, H., Winfield, J., and Xu, X. (2016). Rate Capability of a Cryogenic Stopping CEll for Uranium Projectile Fragments Produced at 100 MeV/u. *Nuclear Instruments and Methods in Physics Research B*, (713):19–26.

[Reiter, 2011] Reiter, M. P. (2011). *Simulation of the cryogenic stopping cell of the FRS Ion Catcher experiment and construction of a novel RFQ beam line system.* Master thesis, Justus-Liebig-University Gießen.

[Reiter, 2015] Reiter, M. P. (2015). *Pilot Experiments with Relativistic Uranium Projectile and Fission Fragments Thermalized in a Cryogenic Gas-Filled Stopping Cell.* Phd thesis, Justus-Liebig-University Gießen.

[Rink, 2012] Rink, A.-K. (2012). A Laser Ablation Ion Source For Characterisation of the Cryogenic Stopping Cell of the RFS Ion Catcher Experiment. Master's thesis, Justus-Liebig-Universität Gießen.

[Rodriguez et al., 2010] Rodriguez, D. et al. (2010). MATS and LaSpec: High-precision experiments using ion traps and lasers at FAIR. *Eur. Phys. J. Special Topics*, 183:1–123.

[Rolfs and Rodney, 1988] Rolfs, C. E. and Rodney, W. S. (1988). *Cauldrons in the cosmos: Nuclear astrophysics.* University of Chicago press.

[Rutherford, 1911] Rutherford, E. (1911). ... *Philosophilcal Magazine*, 669(21).

[Savard et al., 2003] Savard, G., Clark, J., Boudreau, C., Buchinger, F., Crawford, J., Geissel, H., Greene, J., Gulick, S., Heinz, A., Lee, J. K. P., Levand, A., Maier, M., Münzenberg, G., Scheidenberger, C., Seweryniak, D., Sharma, K. S., Sprouse, G., Vaz, J., Wang, J. C., Zabransky, B. J., and Zhou, Z. (2003). Development and operation of gas catchers to thermalize fusion-evaporation and fragmentation products. *Nucl. Instrum. Meth. B*, 204:582–586.

[Scheidenberger and Geissel, 1998] Scheidenberger, C. and Geissel, H. (1998). Penetration of relativistic heavy ions through matter. *Nuclear Instruments and Meth-*

ods in Physics Research Section B: Beam Interactions with Materials and Atoms, 135(1):25–34.

[Scheidenberger et al., 2003] Scheidenberger, C., Geissel, H., Maier, M., Münzenberg, G., Portillo, M., Savard, G., Duppen, P. V., Weick, H., Winkler, M., Yavor, M., Attallah, F., Behr, K.-H., Chichkine, V., Eliseev, S., Hausmann, M., Hellström, M., Kaza, E., Kindler, B., Litvinov, Y., Lommel, B., Marx, G., Matos, M., Nankov, N., Ohtsubo, T., Sümmerer, K., Sun, Z.-Y., and Zhou, Z. (2003). Energy and range focusing of in-flight separated exotic nuclei - a study for the energy-buncher stage of the low-energy branch of the Super-FRS. *Nucl. Instrum. Meth. B*, 204:119–123.

[Scheidenberger et al., 1994] Scheidenberger, C., Geissel, H., Mikkelsen, H., Nickel, F., Brohm, T., Folger, H., Irnich, H., Magel, A., Mohar, M., Münzenberg, G., et al. (1994). Direct observation of systematic deviations from the Bethe stopping theory for relativistic heavy ions. *Physical review letters*, 73(1):50.

[Simon, 2008] Simon, A. (2008). *Entwicklung und Test eines CFK-basierten RF-Quadrupols für ein Multireflektions-Flugzeitmassenspektrometer*. Bachelor thesis, Justus-Liebig-University Gießen.

[Takamine et al., 2005] Takamine, A., Wada, M., Ishida, Y., Nakamura, T., Okada, K., Yamazaki, Y., Kambara, T., Kanai, Y., Kojima, T. M., Nakai, Y., Oshima, N., Yoshida, A., Kubo, T., Ohtani, S., Noda, K., Katayama, I., Hostain, P., Varentsov, V., and Wollnik, H. (2005). Space-charge effects in the catcher gas cell of a rf ion guide. *Rev. Sci. Instrum.*, 76:103503.

[Tarasov and Bazin, 2003] Tarasov, O. and Bazin, D. (2003). Development of the program LISE: Application to fusion-evaporation. *Nucl. Instrum. Meth. B*, 204:174–178.

[Tolmachev et al., 1997] Tolmachev, A. V., Chernushevich, I. V., Dodonov, A. F., and Standing, K. G. (1997). A collisional focusing ion guide for coupling an atmospheric pressure ion source to a mass spectrometer. *Nucl. Instrum. Meth. B*, 124:112–119.

[Tretner, 1959] Tretner, W. (1959). Ein Massenspektroskop für die Hochvakuumtechnik. *Z. Angew. Physik*, 10:395–399.

[Uhlenbeck and Anrnstein, 1930] Uhlenbeck, G. and Anrnstein, L. (1930). On the theory of the bownian motion. *Physical Review*, 36.

[Wada et al., 2003] Wada, M., Ishida, Y., Nakamura, T., Yamazaki, Y., Kambara, T., Ohyama, H., Kanai, Y., Kojima, T. M., Nakai, Y., Ohshima, N., Yoshida, A., Kubo, T., Matsuo, Y., Fukuyama, Y., Okada, K., Sonoda, T., Ohtani, S., Noda, K., Kawakami, H., and Katayama, I. (2003). Slow RI-beams from projectile

fragment separators. *Nucl. Instrum. Meth. B*, 204:570–581.

[Walker et al., 2013] Walker, P., Litvinov, Y., and Geissel, H. (2013). The ILIMA project at FAIR. *International Journal of mass spectrometry*, 100 years of mass spectrometry(349-350):247–254.

[Wang et al., 2012] Wang, M., Audi, G., Wapstra, A. H., Kondev, F. G., McCormick, M., Sun, X., and Pfeiffer, B. (2012). The AME2012 atomic mass evaluation. (ii). Tables, graphs and references. *Chin. Phys. C*, 36:1603–2014.

[Weick et al., 2000] Weick, H., Geissel, H., Scheidenberger, C., Attallah, F., Baumann, T., Cortina, D., Hausmann, M., Lommel, B., Münzenberg, G., Nankov, N., Nickel, F., Radon, T., Schatz, H., Schmidt, K., Stadlmann, J., Sümmerer, K., Winkler, M., and Wollnik, H. (2000). Slowing down of relativistic few-electron heavy ions. *Nucl. Instrum. Meth. B*, 164-165:168–179.

[Wollnik and Przewloka, 1990] Wollnik, H. and Przewloka, M. (1990). Time-of-flight mass spectrometers with multiply reflected ion trajectories. *Int. J. Mass Spectrom. Ion Processes*, 96:267–274.

[Yavor et al., 2015] Yavor, M. I., Plaß, W. R., Dickel, T., Geissel, H., and Scheidenberger, C. (2015). Ion-optical design of a high-performance multiple-reflection time-of-flight mass spectrometer and isobar separator. *Int. J. Mass Spectrom.*, page http://dx.doi.org/10.1016/j.ijms.2015.01.002.

[Yoon et al., 2007] Yoon, O. K., Zuleta, I. A., Robbins, M. D., Barbula, G. K., and Zare, R. N. (2007). Simple template-based method to produce Bradbury-Nielsen Gates. *J. Am. Soc. Mass Spectrom.*, 18:1901–1908.